

# Tunable bandpass filters in chalcogenide fibers and their laser applications

*Kaixuan Zhang*



Department of Electrical & Computer Engineering  
McGill University  
Montréal, Canada

November 2020

---

A thesis submitted to McGill University in partial fulfillment of the requirements for the degree of Doctor of Philosophy.

© 2020 Kaixuan Zhang

## Abstract

The spectral region of 2  $\mu\text{m}$ -12  $\mu\text{m}$  in the mid-infrared accommodates plentiful capabilities with commercial and research value. As development of fiber technologies, all-fiber systems that operate in the mid-infrared spectral region have been subject to intensive interest due to their intrinsic qualities including robustness, flexibility, and ease of integration. Thus, basic building-block components such as filters, couplers, and light sources have become indispensable for mid-infrared fiber applications.

In this thesis, I have investigated tunable bandpass filters made of chalcogenide fibers which are notable as versatile platforms for mid-infrared applications. Theoretical analysis, design instruction, and experimental verification are provided for filters and their laser applications.

The first contribution of this thesis is the demonstration of a chalcogenide fiber Fabry-Perot tunable filter.  $\text{As}_2\text{S}_3$  glass known for its transparency window up to 10  $\mu\text{m}$  is used as fiber substrate. High reflective thin-film coatings composed of alternate layers of germanium and calcium fluoride are deposited on fiber facets in an electron-beam evaporation chamber. The filter shows an ultrabroad tunability  $>300$  nm by controlling the gap distance between two mirrors. Factors degrading the filter performance are analyzed such as surface roughness, thin-film reflectivity, and Gaussian beam divergence. Furthermore, a thulium-doped fiber laser presents a wavelength tunability from 1835 nm to 1920 nm operating in a continuous wave regime, with the Fabry-Perot filter serving as a wavelength-selective component.

The second contribution of this thesis is the demonstration of a tunable bandpass filter based on multimode interference effect in a chalcogenide fiber. The filter consists of a singlemode-multimode-singlemode fiber structure as an appealing solution with ease of fabrication, low cost, and stability. Renowned for its transparency window up to 17  $\mu\text{m}$ ,  $\text{As}_2\text{Se}_3$  glass ensures the mid-infrared compatibility. In comparison with multimode interference filters in silica glass fibers, this work introduces core to core lateral offsets at input and output interfaces between singlemode fiber and multimode fiber, leading to more design flexibility in determining the peak wavelength, free spectral range, and extinction ratio. Broad and continuous wavelength tunability  $>54$  nm is achieved by bending a few-mode  $\text{As}_2\text{Se}_3$  fiber. The mechanism responsible for multimode interference is also summarized, offering guidelines for fabricating a desirable filter.

The third contribution of this thesis is the demonstration of a saturable absorber made

of an  $\text{As}_2\text{Se}_3$  multimode fiber assembly. Instead of operating in a linear regime, saturable absorption is observed as increasing the input power, where detailed theoretical analysis is summarized based on nonlinear multimode interference. The chalcogenide fiber saturable absorber has a modulation depth of 10% and a peak saturation intensity  $<55 \text{ MW/cm}^2$ . The fiber architecture with core to core lateral offsets overcomes the precise length requirement of multimode fiber. Meanwhile, the saturable absorber acts as a bandpass filter simultaneously in the laser cavity, resulting in a pulsed fiber laser tunable from 1834 nm to 1895 nm. Additionally, resembling pulses arise from a secondary cavity, leading to diverse output pulse train patterns.

All chalcogenide fiber tunable filters proposed in the thesis fulfill a need in the field of mid-infrared fiber filters and establish a foundation for future research and applications.

## Résumé

La région spectrale de 2  $\mu\text{m}$  à 12  $\mu\text{m}$  dans l'infrarouge moyen accueille d'abondantes capacités ayant des valeurs commerciales et de recherche. En tant que développement des technologies de fibre, les systèmes tout en fibres qui fonctionnent dans la région spectrale de l'infrarouge moyen ont suscité un intérêt intense en raison de leurs qualités intrinsèques, notamment la robustesse, la flexibilité, et la facilité d'intégration. Ainsi, les composants de base tels que les filtres, les coupleurs, et les sources de lumière sont devenus indispensables pour les applications à fibres dans l'infrarouge moyen.

Dans cette thèse, j'ai étudié les filtres passe-bande accordables en fibres de chalcogénure qui sont remarquables en tant que plates-formes polyvalentes pour les applications dans l'infrarouge moyen. L'analyse théorique, l'instruction de conception, et la vérification expérimentale sont fournies pour les filtres et leurs applications laser.

La première contribution de cette thèse est la démonstration d'un filtre accordable Fabry-Perot en fibre de chalcogénure. Le verre  $\text{As}_2\text{S}_3$  connu pour sa fenêtre de transparence jusqu'à 10  $\mu\text{m}$  est utilisé comme substrat en fibre. Des revêtements en couches minces hautement réfléchissants composés de couches alternées de germanium et de fluorure de calcium sont déposés sur les facettes des fibres dans une chambre d'évaporation à faisceau d'électrons. Le filtre présente une accordabilité ultra large  $>300$  nm en contrôlant la distance entre deux miroirs. Les facteurs dégradant la performance du filtre sont analysés, tels que la rugosité de surface, la réflectivité des couches minces, et la divergence du faisceau gaussien. De plus, un laser à fibre dopée au thulium présente une accordabilité en longueur d'onde de 1835 nm à 1920 nm fonctionnant en régime d'ondes continues, avec le filtre Fabry-Perot servant de composant sélectif de longueur d'onde.

La deuxième contribution de cette thèse est la démonstration d'un filtre passe-bande accordable basé sur l'effet d'interférence multimode dans une fibre de chalcogénure. Le filtre se compose d'une structure de fibre monomode multimode monomode en tant que solution attrayante avec facilité de fabrication, faible coût, et stabilité. Réputé pour sa fenêtre de transparence jusqu'à 17  $\mu\text{m}$ , le verre  $\text{As}_2\text{Se}_3$  assure la compatibilité infrarouge moyen. En comparaison avec les filtres d'interférence multimode dans les fibres de verre de silice, ce travail introduit des décalages latéraux de cœur à cœur aux interfaces d'entrée et de sortie entre la fibre monomode et la fibre multimode, menant à plus de flexibilité de conception dans la détermination de la longueur d'onde de pointe, la gamme spectrale libre,

et le rapport d'extinction. Une accordabilité de longueur d'onde large et continue  $>54$  nm est obtenue en pliant une fibre  $\text{As}_2\text{Se}_3$  à quelques modes. Le mécanisme responsable des interférences multimodes est également résumé, offrant des directives pour la fabrication d'un filtre souhaitable.

La troisième contribution de cette thèse est la démonstration d'un absorbeur saturable constitué d'un assemblage de fibres multimodes  $\text{As}_2\text{Se}_3$ . Au lieu de fonctionner dans un régime linéaire, l'absorption saturable est observée comme augmentant la puissance d'entrée, où l'analyse théorique détaillée est résumée basée sur des interférences multimodes non linéaires. L'absorbeur saturable à fibres de chalcogénure a une profondeur de modulation de 10% et une intensité de saturation maximale  $<55$  MW/cm<sup>2</sup>. L'architecture de la fibre avec des décalages latéraux cœur à cœur surmonte l'exigence de longueur précise de la fibre multimode. Pendant ce temps, l'absorbeur saturable agit comme un filtre passe-bande simultanément dans la cavité laser, résultant en un laser à fibre pulsée accordable de 1834 nm à 1895 nm. En outre, des impulsions ressemblantes proviennent d'une cavité secondaire, conduisant à divers types de trains d'impulsions de sortie.

Tous les filtres accordables en fibre de chalcogénure proposés dans la thèse répondent à un besoin dans le domaine des filtres à fibre infrarouge moyen et établissent une base pour de futures recherches et applications.

## Acknowledgments

First and foremost, I would like to express my sincerest gratitude to my thesis advisor Prof. *Martin Rochette* for his thorough guidance and support that lead me to success in the Ph.D. research. I was impressed with his enthusiasm and cordiality at our first meeting and treasured the opportunity he provided me as a Ph.D. candidate in the fascinating field of nonlinear optics. His meticulous teaching both inside and outside class enhanced my knowledge and research skills toward fiber optics. His scrupulous revising of my manuscripts and presentations not only improved the quality of my works but also promoted my academic writing skill. When my project was stuck, I really appreciated his patience, encouragement, and inspiration while he also tirelessly coordinated me with other professors and students for potential collaboration. I valued the conference chances that he supported me for better personal career development. In addition to the amazing working environment, he shared a fruitful life with me, encouraging me to lead a healthy and joyful lifestyle. I am always grateful to have such a skilled, generous, and amiable mentor.

I would like to express my great esteem to professors in my thesis committee, Prof. *Lawrence R. Chen* and Prof. *Dennis Giannacopoulos* for their valuable time, effort, and comments throughout my research evaluation procedures. Their teaching courses also helped a lot in propelling my projects.

I am grateful to all the professors in the photonics group at McGill university for sharing the lab space, components, and equipment. In particular, I wish to thank Prof. *Yves-Alain Peter* and Prof. *Michel Meunier* at Polytechnique Montréal for the access to CO<sub>2</sub> laser and femtosecond laser fabrication setups as well as facilities in the clean room, which were invaluable experiences in my graduate life. At the same time, I especially thank *Christophe Clément* and *Marie-Hélène Bernier* for teaching me skills in the clean room, making the sample holder, and preparing materials. I would also like to express my gratitude to the examiners of this thesis for their precious time and insightful comments.

I also wish to thank all my colleagues from whom I learned a professional and positive attitude. In particular, my deep gratitude goes to *Lizhu Li* and *Nurmemet Abdukerim* not only for teaching me basic lab skills but also for their amicability of inviting me to various activities. I sincerely thank *Imtiaz Alamgir* and *Mohsen Rezaei* for their precious time of teaching me fiber tapering skills, sharing their equipment, and discussing about experiments. I am grateful to *Zhenping Xing* and *Arslan Anjum* for inspiring discussions. My sincere

gratitude also goes to *Sandrine Filion-Côté* for teaching me the atomic force microscopy and *Jennyfer Zapata* for showing me the femtosecond laser fabrication. I greatly value the friendships with the other members in the photonics group, with whom I thoroughly enjoyed my stay at Montréal.

My thanks also go to the Natural Sciences and Engineering Research Council of Canada (NSERC) for financial grants, and to *CorActive High-Tech Inc.* for providing chalcogenide glass fibers described in this thesis. I would like to express my gratitude to the administrative staff in the Department of Electrical Engineering at McGill University and the Department of Engineering Physics at Polytechnique Montréal, for their assistance during my graduate study.

Finally, my deepest gratitude goes to my whole family members for their continued understanding, unlimited support, meticulous care, and inspiring encouragement that made it possible for me to start and complete my Ph.D. journey. In particular, even deeper gratitude goes to my beloved wife for leading my way, helping me go through tough times, relaxing my mind, and bringing me happiness. I feel blessed to have her in my life.

# Contents

<b>1</b>	<b>Introduction</b>	<b>1</b>
1.1	Fiber optics . . . . .	1
1.2	Optical fiber filter . . . . .	2
1.3	Mid-infrared spectral range . . . . .	2
1.4	Chalcogenide glass fiber . . . . .	3
1.5	Motivation . . . . .	4
1.6	Main contributions . . . . .	5
1.7	Thesis organization . . . . .	5
<b>2</b>	<b>Light propagation in optical fibers and dielectric thin-films</b>	<b>9</b>
2.1	Step-index chalcogenide fiber . . . . .	9
2.2	Beam propagation in a fiber . . . . .	12
2.3	Fiber modes . . . . .	14
2.4	Multilayer thin-film coating . . . . .	20
<b>3</b>	<b>Chalcogenide fiber Fabry-Perot tunable filter</b>	<b>23</b>
3.1	Introduction . . . . .	23
3.2	Theoretical background . . . . .	24
3.2.1	Fabry-Perot filter with a plane wave . . . . .	24
3.2.2	Fabry-Perot filter with a Gaussian beam . . . . .	26
3.3	Design and fabrication . . . . .	28
3.4	Experimental characterization . . . . .	31
3.5	Summary . . . . .	38

---

<b>4</b>	<b>Tunable bandpass filter from multimode interference in chalcogenide fiber</b>	<b>39</b>
4.1	Introduction . . . . .	39
4.2	Theoretical background . . . . .	41
4.2.1	Multimode interference . . . . .	41
4.2.2	Spatial frequency spectrum . . . . .	43
4.2.3	Mechanical bending of multimode fiber . . . . .	44
4.3	Fabrication . . . . .	45
4.4	Experimental characterization . . . . .	47
4.5	Simulation . . . . .	58
4.6	Summary . . . . .	59
<b>5</b>	<b>All-fiber saturable absorber using nonlinear multimode interference in chalcogenide glass</b>	<b>60</b>
5.1	Introduction . . . . .	60
5.2	Theoretical analysis . . . . .	62
5.3	Fabrication . . . . .	64
5.4	Experimental characterization of saturable absorber . . . . .	65
5.5	Experimental characterization of pulsed fiber laser . . . . .	67
5.6	Summary . . . . .	78
<b>6</b>	<b>Conclusion and outlook</b>	<b>80</b>
6.1	Conclusion . . . . .	80
6.2	Outlook . . . . .	82
	<b>References</b>	<b>84</b>

# List of Figures

1.1	Spectral line intensities of molecules in the wavelength range of 2 $\mu\text{m}$ -16 $\mu\text{m}$ . Data from the HITRAN database. . . . .	3
2.1	Schematic of a step-index fiber. (a) Overview. (b) Transverse cross section. (c) Longitudinal cross section. (d) Refractive index distribution. . . . .	10
2.2	Refractive indices of chalcogenide glasses. . . . .	11
2.3	Schematic of a multilayer thin-film coating . . . . .	21
3.1	Schematic of a Fabry-Perot cavity with plane mirrors . . . . .	25
3.2	Transmission spectra of a Fabry-Perot filter without cavity loss. . . . .	26
3.3	Schematic of a fiber Fabry-Perot filter . . . . .	28
3.4	Electron-beam evaporation chamber for thin-film deposition. QCO: quartz crystal oscillator . . . . .	30
3.5	Reflection spectra of 5-layer thin-film coating designed at a central wavelength of (a) 1600 nm and (b) 5000 nm. Thickness of each layer is modified within a random deviation of 20 nm around the quarter wavelength thickness. . . . .	31
3.6	(a) Schematic of the setup to measure the reflection spectra of thin-film coat- ings. (b) Measured and simulated reflection spectra of thin-film coatings with 5-layers (HLHLH) and 3-layers (HLH) structures. H: high refractive index. L: low refractive index. SC: supercontinuum source. OSA: optical spectrum analyzer. . . . .	32
3.7	Fiber facet after polish observed by (a) camera and (b) atomic force mi- croscopy. (c) Extracted roughness. . . . .	33

3.8	(a) Schematic of the setup to measure the transmission spectrum of fiber Fabry-Perot filter. (b) Measured transmission spectra of fiber Fabry-Perot filter at different cavity length. SC: supercontinuum source. OSA: optical spectrum analyzer. FFP-TF: fiber Fabry-Perot tunable filter. . . . .	34
3.9	(a) Schematics of Fabry-Perot filters with the cavity gap constructed by air, index-matching liquid, and micro-lens. (b) Relationship between finesse and free spectral range using different coupling methods. . . . .	35
3.10	Measured and simulated transmission spectra of the fiber Fabry-Perot filter at a cavity length of 4.67 $\mu\text{m}$ , 4.74 $\mu\text{m}$ , and 4.80 $\mu\text{m}$ . HR: high reflective. Noise level is due to the sensitivity limit of optical spectrum analyzer. . . . .	36
3.11	Schematic of a Tm-doped fiber tunable laser. EDFA: erbium-doped fiber amplifier. WDM: wavelength division multiplexer. FFT-FT: fiber Fabry-Perot tunable filter. OSA: optical spectrum analyzer. . . . .	37
3.12	Spectra of the Tm-doped fiber tunable laser with a tunability from 1835 nm to 1920 nm. . . . .	37
4.1	Schematic of a multimode interference filter consisting of singlemode-multimode-singlemode fiber structure with lateral core to core offsets at both input and output interfaces between singlemode fiber and multimode fiber. . . . .	41
4.2	Theoretical and measured relationship between curvature and displacement .	45
4.3	Schematic of setup for tapering the chalcogenide fiber with a COP cladding and a PMMA protective coating. One end of the fiber is fixed, and the other end is pulled at a controlled speed, while a heater is scanning along the fiber.	46
4.4	Schematic of the setup to characterize and bend the MMI filter. SC: supercontinuum source. OSA: optical spectrum analyzer. MMI: multimode interference.	47
4.5	Transmission spectra of MMI filters with various MMF lengths. The $\text{As}_2\text{Se}_3$ core/cladding diameters are 22 $\mu\text{m}$ /170 $\mu\text{m}$ . The lengths are 23 mm, 69 mm, and 104 mm, respectively. . . . .	48
4.6	Transmission spectra and spatial frequency spectra of MMI filters in (a) aligned condition, (b) offset condition 1, (c) offset condition 2, and (d) offset condition 3. The MMF used in these samples has a length of 67 mm and a core diameter of 40 $\mu\text{m}$ . . . . .	49

---

4.7	Transmission spectra of the MMI filter with different transverse offsets at the input SMF-MMF interface. The MMF used in this sample has a length of 74 mm and a core diameter of 34 $\mu\text{m}$ . . . . .	50
4.8	(a) Transmission spectra of the MMI filter under various bending condition. (b) The intensities of transmission spectra are color-coded on a linear scale. The MMF used in this sample has a length of 60 mm and a core diameter of 34 $\mu\text{m}$ . . . . .	52
4.9	(a) Transmission spectra of the MMI filter under various bending condition. (b) The intensities of transmission spectra are color-coded on a linear scale. The MMF used in this sample has a length of 37 mm and a core diameter of 34 $\mu\text{m}$ . . . . .	53
4.10	(a) Transmission spectra of the MMI filter under various bending condition. (b) The intensities of transmission spectra are color-coded on a linear scale. The MMF used in this sample has a length of 67 mm and a core diameter of 40 $\mu\text{m}$ . Offsets could affect the FSR. . . . .	54
4.11	(a) Transmission spectra of the MMI filter under various bending condition. (b) The intensities of transmission spectra are color-coded on a linear scale. The MMF used in this sample has a length of 78 mm and a core diameter of 30 $\mu\text{m}$ . Offsets could affect the FSR. . . . .	55
4.12	Relationship between the transmission spectrum and translation displacement using (a) MMF with a length of 78 mm and a core diameter of 58 $\mu\text{m}$ and (b) MMF with a length of 104 mm and a core diameter of 22 $\mu\text{m}$ . Offsets could affect the FSR. . . . .	57
4.13	(a)-(c) A MMF with a length of 100 mm and a core diameter of 20 $\mu\text{m}$ . Input offset is (a) 0 $\mu\text{m}$ , (b) +2 $\mu\text{m}$ , and (c) +10 $\mu\text{m}$ . (d)-(f) A MMF with a length of 50 mm and a core diameter of 20 $\mu\text{m}$ . Input offset is (a) 0 $\mu\text{m}$ , (b) +2 $\mu\text{m}$ , and (c) +6 $\mu\text{m}$ . . . . .	58
5.1	Schematic of a multimode interference saturable absorber. . . . .	64
5.2	Linear transmission spectra of saturable absorbers. These samples are fabricated with different offset conditions and MMF lengths. . . . .	65

5.3	Schematic of the characterization setup for nonlinear transmission of saturable absorbers as a function of peak power intensity. VOA: variable optical attenuator. MMI-SA: multimode interference saturable absorber. . . . .	66
5.4	Nonlinear transmission of saturable absorbers as a function of peak power intensity. . . . .	67
5.5	Schematic of a fiber pulsed laser. EDFA: erbium-doped fiber amplifier. WDM: wavelength division multiplexer. TDF: thulium-doped fiber. UHNA: ultra-high numerical aperture fiber. OSA: optical spectrum analyzer. PD: photodetector. MMI-SA: multimode interference saturable absorber. Arrows point to SMF-TDF interface and SMF-As <sub>2</sub> Se <sub>3</sub> interface, which forming a secondary Fabry-Perot cavity. . . . .	68
5.6	Impulse response of the photodetector and oscilloscope observed from the detection of 800 fs optical pulses. It has a rise time of 0.1 ns, a fall time of 2.0 ns, a deviation of 0.1 ns. . . . .	69
5.7	Experimental results of the fiber pulsed laser when using SA <sub>2</sub> . (a) Pulse train. (b) Detail of a single pulse. (c) Optical spectrum with a resolution of 0.1 nm. (d) Radio frequency spectrum with a resolution of 1 kHz . . . . .	70
5.8	Experimental results of the fiber pulsed laser when using SA <sub>2</sub> and removing isolator 2. (a) Pulse train. (b) Detail of a single pulse. (c) Radio frequency spectrum in a narrow span with a resolution of 1 kHz and (d) wide span with a resolution of 100 kHz . . . . .	72
5.9	Relationship between output power and pump power of the fiber pulsed laser.	73
5.10	Output pulse trains of the fiber pulsed laser with (a) a total cavity length of 42.4 m and a Fabry-Perot cavity length of 3.59 m, (b) a total cavity length of 43.2 m and a Fabry-Perot cavity length of 4.40 m, and (c) a total cavity length of 47.3 m and a Fabry-Perot cavity length of 8.53 m. . . . .	74
5.11	Spectra of a fiber pulsed laser with a tunability from 1834 nm to 1895 nm. .	75
5.12	(a) Setup of a fiber laser with a total cavity length of 15.2 m and a net cavity dispersion of -0.58 ps <sup>2</sup> . (b) Spectra of Tm-doped fiber spontaneous emission, SA, and dual lasing wavelengths. (c) and (d) Output resembling pulse patterns under different polarization states. . . . .	76

- 
- 5.13 (a) Pulse propagation along the fiber cavity. (b) Pulse in time domain. (c) Spectrum of the pulse. SMF: single mode fiber. DCF: dispersion compensating fiber. SA: saturable absorber. OC: output coupler. There a 3 dB loss at the chalcogenide fiber and 3 dB loss at the DCF. Gain saturation energy is 3 nJ. . . . . 77
- 5.14 (a) Pulse propagation along the fiber cavity. (b) Pulse in time domain. (c) Spectrum of the pulse. SMF: single mode fiber. DCF: dispersion compensating fiber. SA: saturable absorber. OC: output coupler. There a 3 dB loss at the DCF. Gain saturation energy is 10 nJ. . . . . 78

# List of Tables

2.1	Relationship between LP modes, EH modes, and HE modes . . . . .	20
3.1	Properties of common mid-infrared materials . . . . .	29
4.1	Parameters of MMI filters . . . . .	57

# List of Acronyms

COP	cyclo olefin polymer
EDFA	erbium-doped fiber amplifier
FSR	free spectral range
GIMF	graded-index multimode fiber
LP	linearly polarized
MMF	multimode fiber
MMI	multimode interference
NA	numerical aperture
NCF	no core fiber
OSA	optical spectral analyzer
PMMA	polymethyl methacrylate
RF	radio frequency
SA	saturable absorber
SC	supercontinuum
SIMF	step-index multimode fiber
SMF	singlemode fiber
SMS	singlemode-multimode-singlemode
TDF	thulium-doped fiber
UHNA	ultra-high numerical aperture
WDM	wavelength division multiplexer

# Chapter 1

## Introduction

### 1.1 Fiber optics

Since the early years of fiber optics, the first demonstration of low loss silica fiber in the 1970s has not only created a new way of handling optical signals and opened the door to telecommunications [1], but also led to the emergence of versatile fiber components, including attenuator, coupler, filter, polarizer, and amplifier [2]. These inventions immediately became ubiquitous in a vast range of applications thanks to outstanding intrinsic merits of fiber devices such as compactness, low cost, ease of fabrication, simplicity, and excellent beam quality. The compatibility between fiber components eliminates the stringent requirement of optical alignment, offering convenient integration and design flexibility. Therefore, numerous configurations are feasible and less cumbersome compared to bulk optics [3]. An extremely long cavity length is accessible for a pulsed fiber laser with a low repetition rate and high peak power [4]. Heat removal in a fiber laser is also much easier than semiconductor and bulk lasers. Furthermore, fiber components preserve physical durability and operational stability in hostile environments, immune to electromagnetic radiation. Regarding all these unique features, optical fiber has been deemed as an ideal platform for the development toward a new generation of photonic devices. The innovation of fiber technology has also witnessed remarkable achievements in both research and industry applications [5].

## 1.2 Optical fiber filter

Since optical signals are handled either in the time, space, or frequency domain, the demand for frequency-dependent or wavelength-dependent devices is increasing every year. Enormous efforts have been devoured into the development of optical fiber filters, which transmit light in a desirable wavelength range and reject unwanted parts. Taking advantage of the fiber platform, fiber filters have been one of the pillars in modern fiber optics and are nowadays being used in a plethora of applications such as wavelength division multiplexer (WDM), spectroscopy, wavelength-selective switch, noise suppression, environmental sensing, photography, fluorescence microscopy, and laser system [6]. The highlighted parameters of a fiber filter include central wavelength, 3-dB bandwidth, insertion loss, extinction ratio, free spectral range, and wavelength tunability [7]. Over past decades, diverse types of fiber filters have been proposed, commercialized, and employed in different scenarios according to their unique properties. For example, fiber Fabry-Perot filter is well-known for its broad wavelength tunability [8], fiber Bragg grating could reflect light in a narrow bandwidth or serve as a dispersion compensator [9], fiber acousto-optic filter is capable of rapidly tuning the central wavelength [10], and fiber micro-ring resonance filter has a remarkable quality factor [11]. Other kinds of fiber filters also play an important role in wavelength selection such as fiber Faraday filter, Sagnac filter, and thin-film filter.

Despite the tremendous success achieved by all types of fiber filters, the composition of silica glass severely limits their usefulness beyond the spectral range of 2.4  $\mu\text{m}$  due to increasing material absorption coefficient. As a result, current applications only exploit advantages of the telecommunication band while the rest of abundant resources in the mid-infrared spectral range are still waiting to be explored.

## 1.3 Mid-infrared spectral range

The importance of mid-infrared spectral range, spanning 2  $\mu\text{m}$ -12  $\mu\text{m}$ , cannot be overstressed where a vast range of molecules have shown strong vibrational characteristics and fingerprints such as  $\text{H}_2\text{O}$ ,  $\text{CO}_2$ ,  $\text{N}_2\text{O}$ ,  $\text{SO}_2$ , and  $\text{CH}_4$ , leading to spectroscopy for structure identification, chemical sensing, food quality, and environmental monitoring [12, 13]. Figure 1.1 shows the spectral line intensities of some molecules [14]. The mid-infrared region has a low Rayleigh scattering loss and contains two transparency windows of Earth's atmosphere at 3  $\mu\text{m}$ -5  $\mu\text{m}$

and 8  $\mu\text{m}$ -13  $\mu\text{m}$  [15], raising a lot of interest for free-space communication, remote sensing, and LiDAR [16]. Meanwhile, radiation of objects with temperature ranging from  $-31\text{ }^\circ\text{C}$  to  $1180\text{ }^\circ\text{C}$ , such as human bodies and planets, overlaps with the mid-infrared spectral range, playing a pivotal role in thermal imaging, explosive detection, and astronomy [17]. Moreover, mid-infrared light sources provide rising opportunities for material cutting, welding, ablation, and modification [18]. In medical surgery, minimal collateral damage is reported while treating with some soft tissues [19]. Biomedical diagnostics through laser ultrasound imaging and fluorescence-based microscopy are also promising solutions propelled by researchers [20].

It is believed that just as the advent of silica glass fiber helped launch the information age, so will the exploration and exploitation of the mid-infrared spectral range speed up the current technology and science.

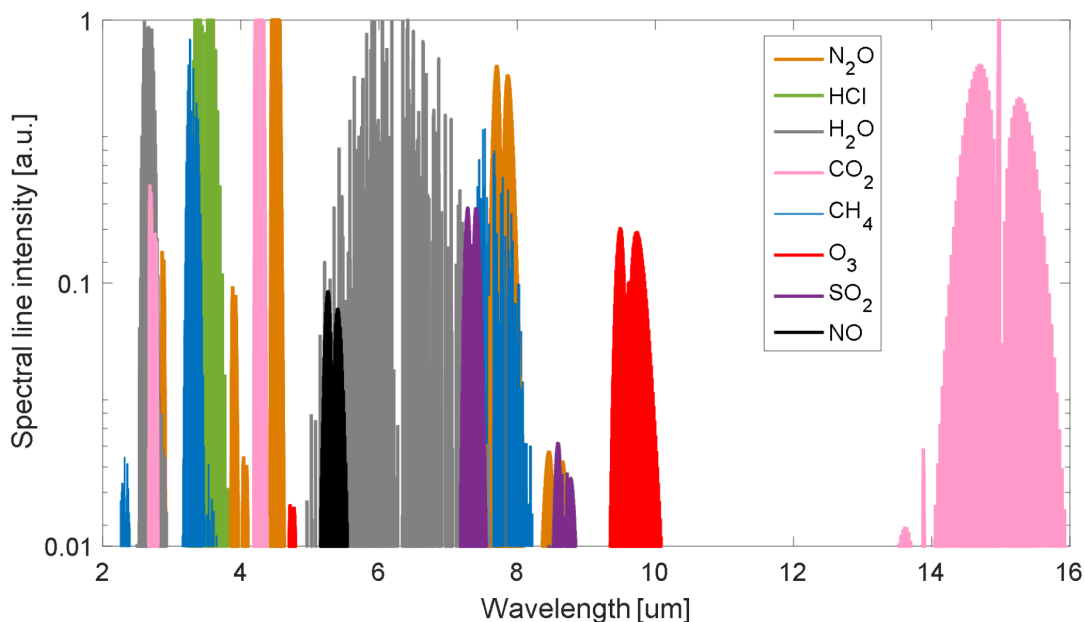


**Fig. 1.1** Spectral line intensities of molecules in the wavelength range of 2  $\mu\text{m}$ -16  $\mu\text{m}$ . Data from the HITRAN database.

## 1.4 Chalcogenide glass fiber

In this regard, various mid-infrared transparent glasses have been investigated over the years. Chalcogenide glasses distinguish themselves with ultra-broad transparency windows, surpass-

ing that of silica glass, sapphire, and fluoride glass which merely extend to 2.4  $\mu\text{m}$ , 6.0  $\mu\text{m}$ , and 7.0  $\mu\text{m}$ , respectively [21]. Chalcogenide glasses are named after the chalcogen compositions such as sulfur (S), selenium (Se), and tellurium (Te) [22]. Since the first report of chalcogenide glasses in the 1950s [23], followed by the first introduction of chalcogenide optical fiber in the 1980s [24], a large variety of glass forming systems have been demonstrated with good resistance to crystallization through covalent bonds to constitues such as arsenic (As), gallium (Ga), germanium (Ge), antimony (Sb), and tin (Sn) [25]. Heavy element with large atomic mass results in low phonon energy, low vibrational frequency, and a long wavelength cut-off edge extending to the mid-infrared spectral range. For instance, chalcogenide glasses of  $\text{As}_2\text{S}_3$ ,  $\text{As}_2\text{Se}_3$ , and  $\text{As}_2\text{Te}_3$  enable mid-infrared transmission up to a wavelength of 11  $\mu\text{m}$ , 17  $\mu\text{m}$ , and 25  $\mu\text{m}$ , respectively [26]. The low phonon energy is also appealing for rare-earth-dopants and responsible for enhanced quantum efficiency in radiation [27, 28]. There are many reports of chalcogenide fibers doped with erbium, thulium, praseodymium, or dysprosium, giving rise to light emissions in the mid-infrared spectral range [29]. Generally, the refractive indices of chalcogenide glasses lie in a range of 2.4-3.0. Widespread  $\text{As}_2\text{Se}_3$  and  $\text{As}_2\text{S}_3$  glasses have a notable nonlinearity up to  $\sim 1000$  times higher than that of silica glass [30], especially attractive for nonlinear applications, including pulse characterization by cross-phase modulation and four-wave mixing [31, 32], Raman gain and Raman based laser oscillation [33–39], parametric gain and optical parametric oscillation [40–43], supercontinuum (SC) [44–48], and wavelength conversion [49–54]. Two-photon absorption coefficients of chalcogenide glasses become negligible in the mid-infrared spectral range, in favor of high-power delivery while I. D. Aggarwal *et al.* reported a fiber damage threshold of 3.0 GW/cm<sup>2</sup> due to dielectric breakdown at the surface [55]. Besides, chalcogenide glasses have low glass transition temperatures about 200 °C, easing the way for fiber fabrication [56], optical fiber coupler fabrication [57, 58], as well as optical fiber taper fabrication [59–62]. Another noteworthy property is the high photosensitivity, benefiting for writing the fiber Bragg grating filter [25, 63].

## 1.5 Motivation

Along with the advance of science and technology, chalcogenide glass fibers have manifested as a novel platform to achieve mid-infrared applications. However, for mid-infrared tunable filters, only a few published works of chalcogenide fiber tunable filters have been reported

before this thesis. To date, Littler *et al.* demonstrated an acousto-optic tunable filter based on chalcogenide fiber around a central wavelength of 1.45  $\mu\text{m}$  [64]. Ahmad *et al.* reported a fiber Bragg-grating tunable filter inscribed into chalcogenide wire at a central wavelength of 1.55  $\mu\text{m}$  [65]. Other mid-infrared filters are in bulk [66] or micro-electromechanical platforms [67] that could not integrate as easily as fiber components. To enrich the category of chalcogenide fiber tunable filters, this thesis focused on a Fabry-Perot tunable filter and a multimode interference (MMI) tunable filter in chalcogenide fibers, paving the way for further applications.

## 1.6 Main contributions

The main contributions of the thesis are summarized as follows. These contributions have been disseminated in the form of journal papers and have been presented at international conferences. First, I demonstrate a Fabry-Perot tunable filter based on  $\text{As}_2\text{S}_3$  fibers with a broad wavelength tunability  $>300$  nm. Mid-infrared transparent materials are selected and deposited on fiber facets using an electron-beam evaporation system, leading to high reflective thin-films. A thulium-doped fiber laser operating in a continuous wave regime is built with a wavelength tunability from 1835 nm to 1920 nm by employing this Fabry-Perot tunable filter. Second, I demonstrate a multimode interference tunable filter based on  $\text{As}_2\text{Se}_3$  fibers. A continuous wavelength tunability  $>54$  nm and a hop tunability of 84 nm are presented, surpassing the tunability of 14 nm in the previous report. The mechanism responsible for multimode interference and design guidelines are summarized. Third, I demonstrate a saturable absorber made of an  $\text{As}_2\text{Se}_3$  multimode fiber for the first time. It has a modulation depth of 10% and a peak saturation intensity  $<55$  MW/cm<sup>2</sup>. An offset coupling structure is proposed to overcome the precise length requirement of multimode fiber. By inserting this saturable absorber in a fiber ring cavity, a pulsed fiber laser is presented with a continuous tunability from 1834 nm to 1895 nm.

## 1.7 Thesis organization

The organization of the thesis is as follows:

Chapter 2 introduces basic concepts of a step-index fiber. Equations for beam propagation are developed from Maxwell's equations. General eigenvalue equations for actual

fiber modes and degenerated fiber modes are summarized. A theoretical model of multilayer thin-films is also described for the design and simulation of a high reflective coating.

Chapter 3 demonstrates the structure and optical properties of a chalcogenide fiber Fabry-Perot tunable filter. Design, fabrication, and characterization process of the high reflective thin-film coating on chalcogenide fiber facet are presented. The transmission spectrum of Fabry-Perot filter is fitted using a Gaussian beam propagation model. Then, as a proof of concept to illustrate the potential application, this Fabry-Perot tunable filter is inserted into a thulium-doped fiber laser cavity, leading to a continuous wave output with a wavelength tunability of 85 nm.

Chapter 4 presents the development of a multimode interference tunable filter consisting of a step-index chalcogenide multimode fiber. Following the analysis of mode propagation theory, filter properties are compared regarding multimode fibers with different core diameters. The schematic with core to core lateral offsets of both input and output fiber is proposed, leading to a new degree of freedom in determining the transmission spectrum. Both continuous and hop wavelength tunability are presented by bending the multimode fiber. Finally, design guidelines for a broadly tunable bandpass filter are summarized.

Chapter 5 presents a chalcogenide fiber saturable absorber based on the nonlinear multimode interference effect. A brief introduction of multimode nonlinear Schrödinger equation is given, followed by the mechanism responsible for the saturable absorption. Then, samples with different saturable absorption properties are compared. Meanwhile, this saturable absorber acts as a bandpass filter simultaneously. Passive mode-locking is triggered by inserting this saturable absorber into a fiber laser cavity, leading to a tunable oscillation wavelength from 1834 nm to 1895 nm. In addition to the conventional single pulse train pattern, resembling pulse pattern is demonstrated and analyzed.

Chapter 6 concludes the thesis and suggests several promising research projects that have been inspired by the results of this thesis.

# List of publications

## Relevant journal publications

- **K. Zhang**, Y. Peter, and M. Rochette, “Chalcogenide Fabry–Perot fiber tunable filter,” *IEEE Photonics Technology Letters*, vol. 30, no. 23, pp. 2013-2016, 2018.

Contributions:

K. Zhang: Performed experiments and prepared manuscript.

Y. Peter: Revised manuscript and co-supervised the project.

M. Rochette: Prepared manuscript and supervised the project.

- **K. Zhang**, I. Alamgir, and M. Rochette, “Mid-infrared compatible tunable bandpass filter based on multimode interference in chalcogenide fiber,” *Journal of Lightwave Technology*, vol. 38, no. 4, pp. 857-863, 2019.

Contributions:

K. Zhang: Performed experiments and prepared manuscript.

I. Alamgir: Multimode fiber preparation.

M. Rochette: Prepared manuscript and supervised the project.

- **K. Zhang** and M. Rochette, “All-fiber saturable absorber using nonlinear multimode interference in a chalcogenide fiber,” *Journal of Lightwave Technology*, vol. 38, no. 22, pp. 6321-6326, 2020.

Contributions:

K. Zhang: Performed experiments and prepared manuscript.

M. Rochette: Prepared manuscript and supervised the project

### Relevant conference publications

- **K. Zhang**, Y. Peter, and M. Rochette, “Chalcogenide Fabry-Perot fiber tunable filter,” at the *IEEE Photonics Conference*, TuD3.3, Reston, Virginia, Oct. 2018.
- **K. Zhang**, I. Alamgir, Y. Peter, and M. Rochette, “Multimode interference tunable filter in chalcogenide fiber,” at the *IEEE Photonics Conference*, MF4.2, San Antonio, Texas, Sept. 2019.
- **K. Zhang** and M. Rochette, “Thulium-doped fiber laser mode-locked from nonlinear multimode interference in chalcogenide fiber,” at the *Conference on Lasers and Electro-Optics (CLEO)*, STh4F.6, virtual conference, May 2020.
- **K. Zhang** and M. Rochette, “Saturable absorption using nonlinear multimode interference in chalcogenide fiber,” at the *Advanced Photonics Congress*, NpM3E.3, virtual conference, July 2020.

### Other conference publications

- A. Anjum, **K. Zhang**, M. El Amraoui, Y. Messaddeq, and M. Rochette, “Chalcogenide fiber based saturable absorber using multimode interference,” at the *Photonics North Conference*, NL-3-26-2, virtual conference, May 2020.

## Chapter 2

# Light propagation in optical fibers and dielectric thin-films

In this chapter, fundamental theories of optical fiber, fiber modes, beam propagation, and multilayer thin-film structure are introduced. Section 2.1 introduces the structure of a step-index chalcogenide fiber. Section 2.2 introduces the beam propagation equation. Section 2.3 describes high-order fiber modes, followed by the eigenvalue equation determining propagation constants of all modes. Finally, section 2.4 gives a brief description of the modeling of multilayer thin-films.

### 2.1 Step-index chalcogenide fiber

Since numerous glass forming systems have been demonstrated in chalcogenide glasses, a step-index chalcogenide fiber could be fabricated with a central core encompassed by a cladding. Either the material constitution is slightly modified, or a different material is used, resulting in a core refractive index  $n_1$  higher than the cladding refractive index  $n_2$ . The numerical aperture (NA) of the fiber is defined as [2]:

$$\text{NA} = n_0 \cdot \sin \theta_0 = \sqrt{n_1^2 - n_2^2} \quad (2.1)$$

where  $n_0$  is the refractive index and  $\theta_0$  is the maximum incident angle at the input medium. Figure 2.1 shows the cylindrical schematic and refractive index distribution of a step-index chalcogenide fiber, where  $a$  is the core radius and  $b$  is the cladding radius. A polymer

coating is usually applied to enclose the cladding, leading to mechanical durability. The NA describes the acceptance angle of the step-index fiber. Generally, the linear refractive index of chalcogenide glass at an operational wavelength far from the resonance is calculated by the Sellmeier equation [2]:

$$n^2(\lambda) = 1 + \sum_{j=1}^m \frac{A_j^2 \lambda^2}{\lambda^2 - \lambda_j^2} \quad (2.2)$$

where  $\lambda_j$  is the resonance wavelength,  $A_j$  is the strength of  $j$ th resonance, and  $\lambda$  is the target operational wavelength. Figure 2.2 shows the calculated refractive indices of  $\text{As}_2\text{S}_3$  glass and  $\text{As}_2\text{Se}_3$  glass as a function of wavelength, using the Sellmeier coefficients from *Amorphous Materials Inc.* [68]

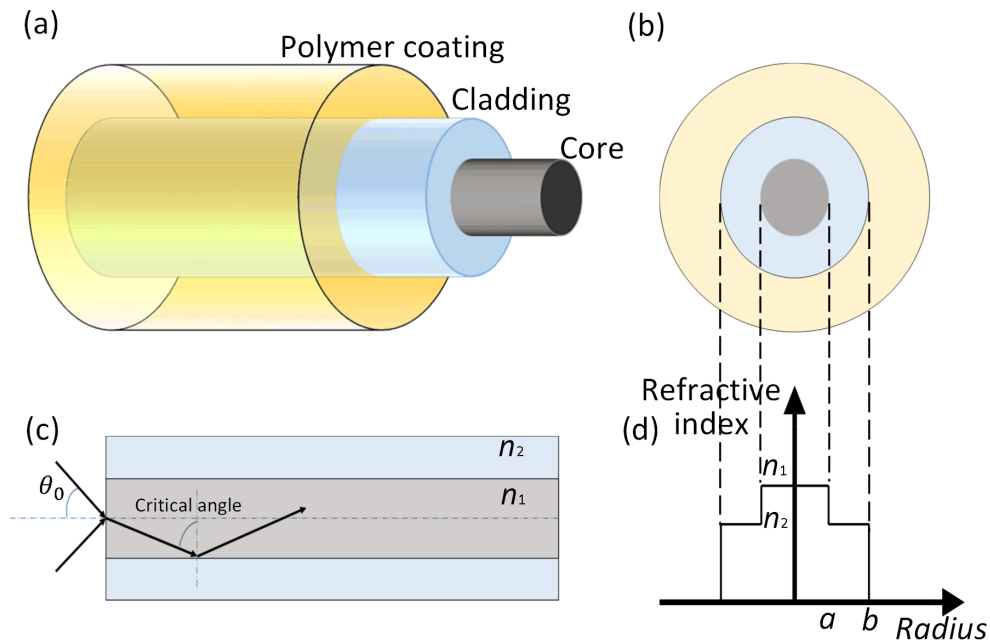


**Fig. 2.1** Schematic of a step-index fiber. (a) Overview. (b) Transverse cross section. (c) Longitudinal cross section. (d) Refractive index distribution.

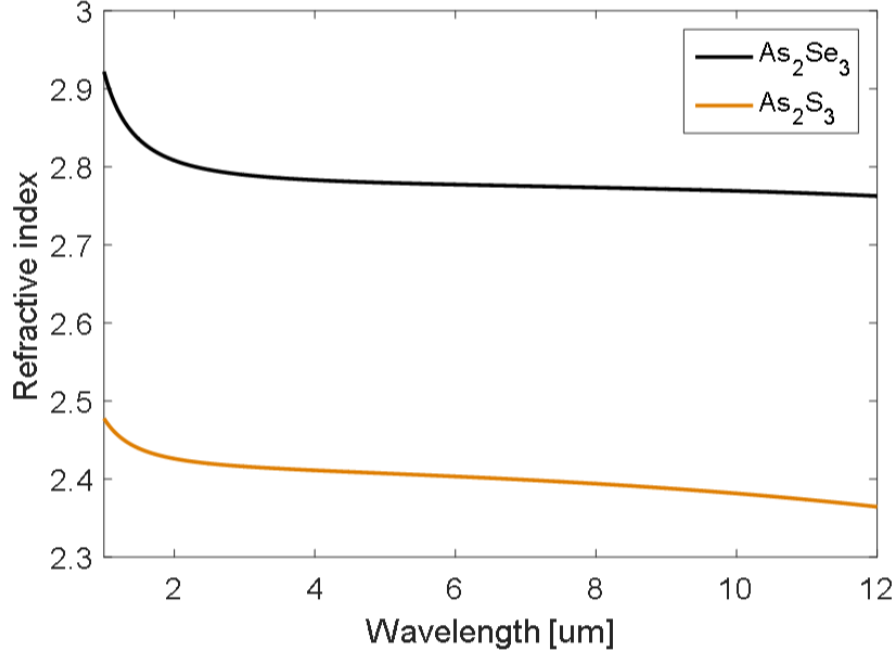


**Fig. 2.2** Refractive indices of chalcogenide glasses.

The phenomenon that material has wavelength or frequency dependent properties is known as material chromatic dispersion, resulting in a varied phase propagation constant that is defined and expanded in a Taylor series as [69]:

$$\beta(\omega) = n_{\text{eff}}(\omega) \cdot \frac{\omega}{c_0} = \beta_0 + \beta_1 \cdot (\omega - \omega_0) + \frac{1}{2} \beta_2 \cdot (\omega - \omega_0)^2 + \dots \quad (2.3)$$

$$\beta_m = \left( \frac{d^m \beta}{d\omega} \right)_{\omega=\omega_0} \quad m = 0, 1, 2, \dots$$

where  $n_{\text{eff}}(\omega)$  is termed as the effective refractive index, determined by the fiber structure, refractive indices, and operational wavelength.  $c_0$  is the light speed in vacuum.  $\beta_0$  is the propagation constant at a frequency of  $\omega_0$ ,  $\beta_1$  accounts for the group velocity, and  $\beta_2$  describes the group velocity dispersion that responsible for pulse broadening.

## 2.2 Beam propagation in a fiber

The behavior of electromagnetic wave in a step-index fiber is dominated by Maxwell's equations and constitutive relations in the material, which are summarized as the following set [70]:

$$\nabla \times E = -\frac{\partial B}{\partial t} \quad (2.4)$$

$$\nabla \times H = J + \frac{\partial D}{\partial t} \quad (2.5)$$

$$\nabla \cdot D = \rho_v \quad (2.6)$$

$$\nabla \cdot B = 0 \quad (2.7)$$

$$D = \epsilon_0 E + P \quad (2.8)$$

$$B = \mu_0 H + M \quad (2.9)$$

where  $E$  and  $H$  are the electric and magnetic field vectors.  $D$  and  $B$  are the corresponding electric and magnetic flux densities.  $J$  and  $\rho_v$  are current and charge densities, which equate to zero in the absence of free charges in an optical fiber. And  $t$  corresponds to the time domain. According to the constitutive relations in the material, the electric and magnetic flux densities  $D$  and  $B$  arise in response to the electric and magnetic fields  $E$  and  $H$ , where  $\epsilon_0$  and  $\mu_0$  are the values of permittivity and permeability in vacuum.  $P$  and  $M$  denote the induced electric and magnetic polarizations in the material. Chalcogenide glasses are nonmagnetic materials, leading to  $M = 0$ .

For simplification, magnetic related parameters are eliminated and only the electric field is preserved to better investigate the propagation behavior. At first, applying curl operator to Eq. 2.4 leads to

$$\nabla \times \nabla \times E = \nabla \times \left( -\frac{\partial B}{\partial t} \right) \quad (2.10)$$

Then use Eq. 2.5, Eq. 2.8, and Eq. 2.9 to eliminate  $B$ ,  $H$ , and  $D$ , resulting in

$$\nabla \times \nabla \times E = -\epsilon_0 \mu_0 \frac{\partial^2 E}{\partial t^2} - \mu_0 \frac{\partial^2 P}{\partial t^2} \quad (2.11)$$

According to the vector identity relation where  $\nabla \times (\nabla \times A) = \nabla(\nabla \cdot A) - \nabla^2 A$ , Eq. 2.11 is

expressed as

$$\nabla(\nabla \cdot E) - \nabla^2 E = -\epsilon_0 \mu_0 \frac{\partial^2 E}{\partial t^2} - \mu_0 \frac{\partial^2 P}{\partial t^2} \quad (2.12)$$

In a homogeneous medium such as a step-index fiber, the polarization induced by electric field is represented in linear and nonlinear parts

$$P_L(t) = \epsilon_0 \int_{-\infty}^t \chi^{(1)}(t - \tau) \cdot E(\tau) d\tau \quad (2.13)$$

$$P_{NL}(t) = \epsilon_0 \int_{-\infty}^t d\tau_1 \int_{-\infty}^{\tau_1} d\tau_2 \int_{-\infty}^{\tau_2} d\tau_3 \times \chi^{(3)}(t - \tau_1, t - \tau_2, t - \tau_3) : E(\tau_1) E(\tau_2) E(\tau_3) \quad (2.14)$$

where  $\chi^{(1)}$  and  $\chi^{(3)}$  are the first and third order of electric susceptibilities of the medium.

To further simplify the equation, only linear instantaneous polarization is considered, assuming  $P = \epsilon_0 \chi^{(1)} E$ . Then, Eq. 2.8 is written as

$$D = \epsilon_0 (1 + \chi^{(1)}) E = \epsilon_0 \epsilon_r E = \epsilon E \quad (2.15)$$

where  $\epsilon$  is the permittivity in medium and  $\epsilon_r$  is a dielectric constant.

Generally, permittivity  $\epsilon$  in the fiber is independent of spatial coordinates, leading to  $\nabla \cdot D = \epsilon \nabla \cdot E = 0$ . Then Eq. 2.12 takes the form of the wave equation

$$\nabla^2 E = \epsilon \mu_0 \frac{\partial^2 E}{\partial t^2} \quad (2.16)$$

Applying definitions  $c_0^2 = 1/\epsilon_0 \mu_0$  and  $\epsilon_r = 1 + \chi^{(1)} = n^2$ , where  $n$  is the refractive index of the medium. Eq. 2.16 is rewritten as

$$\nabla^2 E = \frac{n^2}{c_0^2} \frac{\partial^2 E}{\partial t^2} \quad (2.17)$$

To convert the wave equation into the frequency domain by applying the Fourier transformation function  $\tilde{E}(\omega) = \int_{-\infty}^{\infty} E(t) \cdot e^{-i\omega t} dt$ , one can get the well-known Helmholtz equation [69]

$$\nabla^2 \tilde{E}(\omega) + n^2 k_0^2 \tilde{E}(\omega) = 0 \quad (2.18)$$

where  $k_0 = \omega/c_0$  is termed as the wavenumber.

### 2.3 Fiber modes

Incorporated with the boundary condition determined by the fiber structure, a finite number of solutions of the Helmholtz equation are calculated. These solutions are known as guided fiber modes describing the behaviors of electromagnetic waves propagating along a step-index optical fiber while maintaining their propagation constants and transverse field distributions. To solve the Helmholtz equation in a fiber, Eq. 2.18 is expressed in cylindrical coordinates  $r$ ,  $\phi$ , and  $z$ :

$$\frac{\partial^2 \tilde{E}}{\partial r^2} + \frac{1}{r} \frac{\partial \tilde{E}}{\partial r} + \frac{1}{r^2} \frac{\partial^2 \tilde{E}}{\partial \phi^2} + \frac{\partial^2 \tilde{E}}{\partial z^2} + n^2 k_0^2 \tilde{E} = 0 \quad (2.19)$$

The electric field  $\tilde{E}$  is decomposed into three polarization directions, which all satisfy Eq. 2.19. The magnetic field  $\tilde{H}$  is also decomposed into  $\tilde{H}_r$ ,  $\tilde{H}_\phi$ , and  $\tilde{H}_z$  in a similar way.

$$\begin{aligned} \tilde{E}(r, \phi, z) &= \tilde{E}_r(r, \phi, z) \hat{r} + \tilde{E}_\phi(r, \phi, z) \hat{\phi} + \tilde{E}_z(r, \phi, z) \hat{z} \\ \tilde{H}(r, \phi, z) &= \tilde{H}_r(r, \phi, z) \hat{r} + \tilde{H}_\phi(r, \phi, z) \hat{\phi} + \tilde{H}_z(r, \phi, z) \hat{z} \end{aligned} \quad (2.20)$$

For electromagnetic waves, only two components out of six are independent. Thus,  $\tilde{E}_z$  and  $\tilde{H}_z$  are customarily chosen while others are expressed in terms of  $\tilde{E}_z$  and  $\tilde{H}_z$ . The following equations are derived from Eq. 2.4 to Eq. 2.9 [71]:

$$\tilde{E}_r = \frac{-i\beta}{\omega^2 \mu \epsilon - \beta^2} \left[ \frac{\partial \tilde{E}_z}{\partial r} + \frac{\omega \mu}{\beta r} \frac{\partial \tilde{H}_z}{\partial \phi} \right] \quad (2.21)$$

$$\tilde{E}_\phi = \frac{-i\beta}{\omega^2 \mu \epsilon - \beta^2} \left[ \frac{1}{r} \frac{\partial \tilde{E}_z}{\partial \phi} - \frac{\omega \mu}{\beta} \frac{\partial \tilde{H}_z}{\partial r} \right] \quad (2.22)$$

$$\tilde{H}_r = \frac{-i\beta}{\omega^2 \mu \epsilon - \beta^2} \left[ \frac{\partial \tilde{H}_z}{\partial r} - \frac{\omega \epsilon}{\beta r} \frac{\partial \tilde{E}_z}{\partial \phi} \right] \quad (2.23)$$

$$\tilde{H}_\phi = \frac{-i\beta}{\omega^2 \mu \epsilon - \beta^2} \left[ \frac{1}{r} \frac{\partial \tilde{H}_z}{\partial \phi} + \frac{\omega \epsilon}{\beta} \frac{\partial \tilde{E}_z}{\partial r} \right] \quad (2.24)$$

The method of separation of variables is used to solve  $\tilde{E}_z$  by assuming

$$\tilde{E}_z(r, \phi, z) = F(r) \cdot \Phi(\phi) \cdot Z(z) \cdot e^{i\omega t} \quad (2.25)$$

Substituting Eq. 2.25 into Eq. 2.19 leads to

$$\frac{1}{F \cdot r} \frac{\partial F}{\partial r} + \frac{1}{F} \frac{\partial^2 F}{\partial r^2} + \frac{1}{\Phi \cdot r^2} \frac{\partial^2 \Phi}{\partial \phi^2} + \frac{1}{Z} \frac{\partial^2 Z}{\partial z^2} + k_0^2 n^2 = 0 \quad (2.26)$$

Eq. 2.26 is rearranged to obtain

$$\begin{cases} -\frac{1}{Z} \frac{\partial^2 Z}{\partial z^2} = \beta^2 \\ \frac{1}{F \cdot r} \frac{\partial F}{\partial r} + \frac{1}{F} \frac{\partial^2 F}{\partial r^2} + \frac{1}{\Phi \cdot r^2} \frac{\partial^2 \Phi}{\partial \phi^2} + k_0^2 n^2 = \beta^2 \end{cases} \quad (2.27)$$

Then equation of  $Z(z)$  is solved as

$$Z(z) = e^{-i\beta z} \quad (2.28)$$

Substituting Eq. 2.28 into Eq. 2.27 and mutiplied by  $r^2$  at both sides of the equation, lead to

$$\frac{r}{F} \frac{\partial F}{\partial r} + \frac{r^2}{F} \frac{\partial^2 F}{\partial r^2} + k_0^2 n^2 r^2 - \beta^2 r^2 = -\frac{1}{\Phi} \frac{\partial^2 \Phi}{\partial \phi^2} \quad (2.29)$$

Similarly, Eq. 2.29 is rearranged to obtain

$$\begin{cases} -\frac{1}{\Phi} \frac{\partial^2 \Phi}{\partial \phi^2} = m^2 \\ \frac{r}{F} \frac{\partial F}{\partial r} + \frac{r^2}{F} \frac{\partial^2 F}{\partial r^2} + k_0^2 n^2 r^2 - \beta^2 r^2 = m^2 \end{cases} \quad (2.30)$$

The equation of  $\Phi(\phi)$  is solved as

$$\Phi(\phi) = e^{im\phi} \quad (2.31)$$

where  $m$  must be an integer to satisfy the azimuthal condition that  $\Phi(\phi) = \Phi(\phi + 2\pi)$ .

Substituting Eq. 2.28 and Eq. 2.31 into Eq. 2.25,  $\tilde{E}_z$  is rewritten following the form of

$$\tilde{E}_z(r, \phi, z) = F(r) \cdot e^{i(\omega t - \beta z + m\phi)} \quad (2.32)$$

Then, Eq. 2.30 is rearranged as

$$\frac{\partial^2 F}{\partial r^2} + \frac{1}{r} \frac{\partial F}{\partial r} + \left( n^2 k_0^2 - \beta^2 - \frac{m^2}{r^2} \right) F = 0 \quad (2.33)$$

Eq. 2.33 is well-known as the Bessel differential equation solved using the series method to

obtain solutions known as Bessel functions. Recall the refractive index distribution.

$$n = \begin{cases} n_1 & \text{for } r \leq a \\ n_2 & \text{for } r > a \end{cases}$$

In view of the physical consideration that power cannot be infinite, solutions of Eq. 2.33 are expressed as

$$F(r) = \begin{cases} AJ_m(\kappa r) & \text{for } r \leq a \\ CK_m(\gamma r) & \text{for } r > a \end{cases} \quad (2.34)$$

where  $A$  and  $C$  are constants,  $\kappa$  and  $\gamma$  are defined as

$$\begin{cases} \kappa = \sqrt{n_1^2 k_0^2 - \beta^2} \\ \gamma = \sqrt{\beta^2 - n_2^2 k_0^2} \end{cases} \quad (2.35)$$

In summary,  $\tilde{E}_z$  has the form of

$$\tilde{E}_z(r, \phi, z) = \begin{cases} AJ_m(\kappa r) \cdot e^{i(\omega t - \beta z + m\phi)} & \text{for } r \leq a \\ CK_m(\gamma r) \cdot e^{i(\omega t - \beta z + m\phi)} & \text{for } r \geq a \end{cases} \quad (2.36)$$

The same procedure is followed to obtain the magnetic field component and  $\tilde{H}_z$  has the form of

$$\tilde{H}_z(r, \phi, z) = \begin{cases} BJ_m(\kappa r) \cdot e^{i(\omega t - \beta z + m\phi)} & \text{for } r \leq a \\ DK_m(\gamma r) \cdot e^{i(\omega t - \beta z + m\phi)} & \text{for } r \geq a \end{cases} \quad (2.37)$$

Replacing  $\tilde{E}_z$  and  $\tilde{H}_z$  of Eq. 2.21 to Eq. 2.24, one can get expressions of the rest four

components for an electromagnetic wave. In the core region,

$$\begin{aligned}
 \tilde{E}_r &= \frac{-i\beta}{\kappa^2} \left[ A\kappa J'_m(\kappa r) + \frac{i\omega\mu m}{\beta r} B J_m(\kappa r) \right] \cdot e^{i(\omega t - \beta z + m\phi)} \\
 \tilde{E}_\phi &= \frac{-i\beta}{\kappa^2} \left[ \frac{im}{r} A J_m(\kappa r) - \frac{\omega\mu}{\beta} B \kappa J'_m(\kappa r) \right] \cdot e^{i(\omega t - \beta z + m\phi)} \\
 \tilde{H}_r &= \frac{-i\beta}{\kappa^2} \left[ B \kappa J'_m(\kappa r) - \frac{i\omega\epsilon_0 n_1^2 m}{\beta r} A J_m(\kappa r) \right] \cdot e^{i(\omega t - \beta z + m\phi)} \\
 \tilde{H}_\phi &= \frac{-i\beta}{\kappa^2} \left[ \frac{im}{r} B J_m(\kappa r) + \frac{\omega\epsilon_0 n_1^2}{\beta} A \kappa J'_m(\kappa r) \right] \cdot e^{i(\omega t - \beta z + m\phi)}
 \end{aligned} \tag{2.38}$$

And in the cladding region,

$$\begin{aligned}
 \tilde{E}_r &= \frac{i\beta}{\gamma^2} \left[ C\gamma K'_m(\gamma r) + \frac{i\omega\mu m}{\beta r} D K_m(\gamma r) \right] \cdot e^{i(\omega t - \beta z + m\phi)} \\
 \tilde{E}_\phi &= \frac{i\beta}{\gamma^2} \left[ \frac{im}{r} C K_m(\gamma r) - \frac{\omega\mu}{\beta} D \gamma K'_m(\gamma r) \right] \cdot e^{i(\omega t - \beta z + m\phi)} \\
 \tilde{H}_r &= \frac{i\beta}{\gamma^2} \left[ D \gamma K'_m(\gamma r) - \frac{i\omega\epsilon_0 n_2^2 m}{\beta r} C K_m(\gamma r) \right] \cdot e^{i(\omega t - \beta z + m\phi)} \\
 \tilde{H}_\phi &= \frac{i\beta}{\gamma^2} \left[ \frac{im}{r} D K_m(\gamma r) + \frac{\omega\epsilon_0 n_2^2}{\beta} C \gamma K'_m(\gamma r) \right] \cdot e^{i(\omega t - \beta z + m\phi)}
 \end{aligned} \tag{2.39}$$

Meanwhile, the tangential components of  $\tilde{E}$  and  $\tilde{H}$  are continuous across the core-cladding interface, imposing that  $\tilde{E}_z$ ,  $\tilde{H}_z$ ,  $\tilde{E}_\phi$ , and  $\tilde{H}_\phi$  are continuous when  $r = a$ . To determine the coefficients of  $A$ ,  $B$ ,  $C$ , and  $D$ , following equations are constructed:

$$\begin{cases}
 A J_m(\kappa a) = C K_m(\gamma a) \\
 B J_m(\kappa a) = D K_m(\gamma a) \\
 \frac{-i\beta}{\kappa^2} \left[ \frac{im}{r} A J_m(\kappa a) - \frac{\omega\mu}{\beta} B \kappa J'_m(\kappa a) \right] = \frac{i\beta}{\gamma^2} \left[ \frac{im}{r} C K_m(\gamma a) - \frac{\omega\mu}{\beta} D \gamma K'_m(\gamma a) \right] \\
 \frac{-i\beta}{\kappa^2} \left[ \frac{im}{r} B J_m(\kappa a) + \frac{\omega\epsilon_0 n_1^2}{\beta} A \kappa J'_m(\kappa a) \right] = \frac{i\beta}{\gamma^2} \left[ \frac{im}{r} D K_m(\gamma a) + \frac{\omega\epsilon_0 n_2^2}{\beta} C \gamma K'_m(\gamma a) \right]
 \end{cases} \tag{2.40}$$

which could be reconstructed into the matrix form

$$[\mathbf{M}](A \ B \ C \ D)^T = 0$$

where

$$[\mathbf{M}] = \begin{bmatrix} J_m(\kappa a) & 0 & -K_m(\gamma a) & 0 \\ 0 & J_m(\kappa a) & 0 & -K_m(\gamma a) \\ \frac{\beta m}{\kappa^2 a} J_m(\kappa a) & \frac{i\omega\mu}{\kappa} J'_m(\kappa a) & \frac{\beta m}{\gamma^2 a} K_m(\kappa a) & \frac{i\omega\mu}{\gamma} K'_m(\gamma a) \\ \frac{-i\omega\epsilon_0 n_1^2}{\kappa} J'_m(\kappa a) & \frac{\beta m}{\kappa^2 a} J_m(\kappa a) & \frac{-i\omega\epsilon_0 n_2^2}{\gamma} K'_m(\gamma a) & \frac{\beta m}{\gamma^2 a} K_m(\gamma a) \end{bmatrix}$$

In order to get a nonzero solution for  $(A \ B \ C \ D)$ , the matrix  $\mathbf{M}$  is required to be non-full rank, while the determinant of matrix  $\mathbf{M}$  should be zero. Thus, the eigenvalue equation is obtained, where  $\beta$  is the only unknown variable. For each integer value of  $m$ , there are a various number of solutions for  $\beta$ , labeled as  $\beta_{m,n}$ , corresponding to the propagation constant of each fiber mode [71].

$$\begin{aligned} & \left[ \frac{J'_m(\kappa a)}{\kappa a J_m(\kappa a)} + \frac{K'_m(\gamma a)}{\gamma a K_m(\gamma a)} \right] \left[ \frac{n_1^2 J'_m(\kappa a)}{\kappa a J_m(\kappa a)} + \frac{n_2^2 K'_m(\gamma a)}{\gamma a K_m(\gamma a)} \right] \\ & = \left[ \left( \frac{1}{\kappa a} \right)^2 + \left( \frac{1}{\gamma a} \right)^2 \right]^2 \left( \frac{m\beta}{k_0} \right)^2 \end{aligned} \quad (2.41)$$

According to Eq. 2.40, coefficients  $B$ ,  $C$ , and  $D$  can be represented in the form of coefficient  $A$ . However, because the matrix  $\mathbf{M}$  is non-full rank, the coefficient  $B$  has two solutions, one of them expressed as

$$B = \frac{i\beta m}{\omega\mu a} \frac{\frac{1}{\kappa^2} + \frac{1}{\gamma^2}}{\frac{J'_m(\kappa a)}{\kappa J_m(\kappa a)} + \frac{K'_m(\gamma a)}{\gamma K_m(\gamma a)}} A \quad (2.42)$$

which corresponds to  $\tilde{E}_\phi$  continuity, leading to EH modes that with  $B > A$ . The eigenvalue equation for EH modes is derived as

$$\begin{aligned} \frac{J_{m+1}(\kappa a)}{\kappa a J_m(\kappa a)} &= \frac{n_1^2 + n_2^2}{2n_1^2} \frac{K'_m(\gamma a)}{\gamma a K_m(\gamma a)} + \\ & \left[ \frac{m}{(\kappa a)^2} - \sqrt{\left( \frac{n_1^2 - n_2^2}{2n_1^2} \right)^2 \left( \frac{K'_m(\gamma a)}{\gamma a K_m(\gamma a)} \right)^2 + \left( \frac{m\beta}{n_1 k_0} \right)^2 \left[ \left( \frac{1}{\kappa a} \right)^2 + \left( \frac{1}{\gamma a} \right)^2 \right]^2} \right] \end{aligned} \quad (2.43)$$

Another solution of  $B$  is expressed as

$$B = \frac{i\omega\epsilon_0 a}{\beta m} \frac{\frac{n_1^2 J'_m(\kappa a)}{\kappa J_m(\kappa a)} + \frac{n_2^2 K'_m(\gamma a)}{\gamma K_m(\gamma a)}}{\frac{1}{\kappa^2} + \frac{1}{\gamma^2}} A \quad (2.44)$$

which corresponds to  $\tilde{H}_\phi$  continuity, leading to HE modes with  $A > B$ . The eigenvalue equation for HE modes is derived as

$$\frac{J_{m-1}(\kappa a)}{\kappa a J_m(\kappa a)} = -\frac{n_1^2 + n_2^2}{2n_1^2} \frac{K'_m(\gamma a)}{\gamma a K_m(\gamma a)} + \left[ \frac{m}{(\kappa a)^2} - \sqrt{\left(\frac{n_1^2 - n_2^2}{2n_1^2}\right)^2 \left(\frac{K'_m(\gamma a)}{\gamma a K_m(\gamma a)}\right)^2 + \left(\frac{m\beta}{n_1 k_0}\right)^2 \left[\left(\frac{1}{\kappa a}\right)^2 + \left(\frac{1}{\gamma a}\right)^2\right]^2} \right] \quad (2.45)$$

Especially when  $m = 0$ , then either  $B = 0$  or  $A = 0$ . There are only fields of  $\tilde{E}_r$ ,  $\tilde{E}_z$ , and  $\tilde{H}_\phi$ , referred as TM mode for  $B = 0$ . There are only fields of  $\tilde{H}_r$ ,  $\tilde{H}_z$ , and  $\tilde{E}_\phi$  referred as TE mode for  $A = 0$ .

For further simplification, it is customary to make a weakly guiding approximation in optical fibers where the difference of refractive indices between core and cladding is small such that  $n_1 \approx n_2$ . Then Eq. 2.43 and Eq. 2.45 are reduced to

$$\frac{J_{m+1}(\kappa a)}{\kappa a J_m(\kappa a)} + \frac{K_{m+1}(\gamma a)}{\gamma a K_m(\gamma a)} = 0 \quad \text{for EH modes} \quad (2.46)$$

$$\frac{J_{m-1}(\kappa a)}{\kappa a J_m(\kappa a)} - \frac{K_{m-1}(\gamma a)}{\gamma a K_m(\gamma a)} = 0 \quad \text{for HE modes} \quad (2.47)$$

On the other hand, linearly polarized (LP) light are assumed regarding the weakly guiding assumption where  $\tilde{E}_y = 0$  and  $\tilde{E}_x(r, \phi, z) = F(r)e^{i(\omega t - \beta z + m\phi)}$ . Following the same analysis procedure, the eigenvalue equation for LP modes is obtained as

$$\frac{J_m(\kappa a)}{\kappa a J_{m-1}(\kappa a)} + \frac{K_m(\gamma a)}{\gamma a K_{m-1}(\gamma a)} = 0 \quad \text{for LP modes} \quad (2.48)$$

It is found that Eq. 2.48 has same solutions that also satisfy Eq. 2.46 or Eq. 2.47, which means LP modes are constructed by superposition of the degenerated EH modes and HE modes that have the same propagation constant. Thus, it is reasonable to make the assumption of LP modes. The detailed relationship between LP modes and the corresponding EH modes or HE modes is listed in the following table [71]:

**Table 2.1** Relationship between LP modes, EH modes, and HE modes

LP modes ( $n \geq 1$ )	Conventional modes ( $n \geq 1$ )
LP <sub>0n</sub>	HE <sub>1n</sub>
LP <sub>1n</sub>	TE <sub>0n</sub> , TM <sub>0n</sub> , HE <sub>2n</sub>
LP <sub>mn</sub> ( $m \geq 2$ )	EH <sub>m-1,n</sub> , HE <sub>m+1,n</sub>

## 2.4 Multilayer thin-film coating

There have been extensive studies toward dielectric thin-film coatings that act as antireflective coating, high reflective coating, beam splitter, and bandpass filter based on the interference of light. It is addressed that a multilayer thin-film structure is adopted in an ultra-high reflective coating with less absorption loss than metallic mirrors. Theoretical analysis regarding reflectance and transmittance of the multilayer thin-film coating has been developed in many textbooks [70, 72, 73].

Figure. 2.3 shows the schematic of multilayer thin-film structure consisting of  $L$  layers in total between an incident medium and a substrate. Refractive indices of the incident medium, the  $k$ th layer, and substrate are labeled as  $n_0$ ,  $n_k$ , and  $n_s$ , respectively. The thickness of each layer is referred as  $d_k$ .

The matrix method is a powerful way to calculate the properties of multilayer thin-film coating where each matrix represents a single thin-film layer, written in a notation [73]

$$\mathbf{M}_k = \begin{bmatrix} \cos \delta_k & \frac{i}{\eta_k} \sin \delta_k \\ i\eta_k \sin \delta_k & \cos \delta_k \end{bmatrix} \quad (2.49)$$

where  $\delta_k$  is the phase shift

$$\delta_k = \frac{2\pi n_k d_k \cos \theta_k}{\lambda} \quad (2.50)$$

with  $\lambda$  the wavelength of incident light. And  $\eta_k$  is the effective refractive index in each layer

$$\eta_k = \begin{cases} \frac{n_k}{\cos \theta_k} & \text{for p-polarization} \\ n_k \cos \theta_k & \text{for s-polarization} \end{cases} \quad (2.51)$$

where  $\theta_k$  is the propagation angle in each layer. Snell's law provides correlations for  $\theta_k$  in

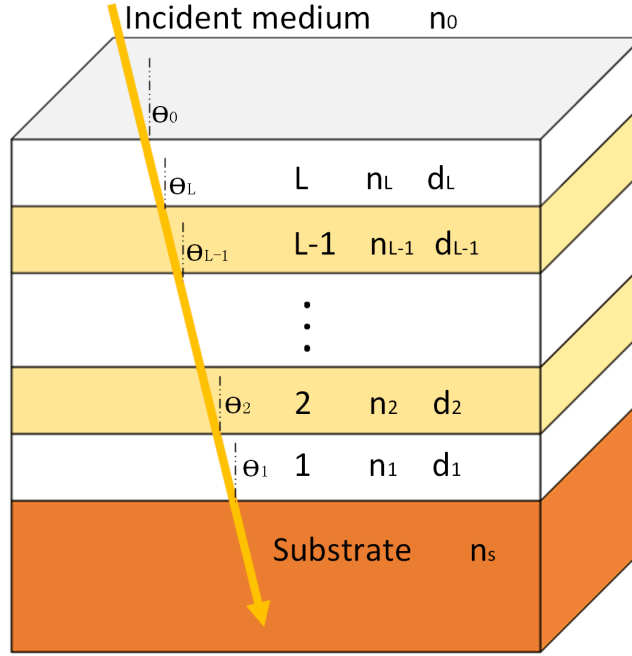


**Fig. 2.3** Schematic of a multilayer thin-film coating

each layer.

$$n_0 \sin \theta_0 = n_k \sin \theta_k$$

The characteristic matrix of the whole multilayer thin-film coating is written as the product of each matrix

$$\mathbf{M} = \mathbf{M}_L \mathbf{M}_{L-1} \cdots \mathbf{M}_2 \mathbf{M}_1 = \begin{bmatrix} m_{11} & m_{12} \\ m_{21} & m_{22} \end{bmatrix} \quad (2.52)$$

Then the amplitudes of reflectivity and transmissivity are calculated through [73]

$$r = \frac{n_0 m_{11} - n_s m_{22} + n_0 n_s m_{12} - m_{21}}{n_0 m_{11} + n_s m_{22} + n_0 n_s m_{12} + m_{21}} \quad (2.53)$$

$$t = \frac{2n_0}{n_0 m_{11} + n_s m_{22} + n_0 n_s m_{12} + m_{21}} \quad (2.54)$$

followed with the intensity of reflectance and transmittance expressed by

$$R = rr^* \quad (2.55)$$

$$T = \frac{\text{Re}[n_s]}{\text{Re}[n_0]} tt^* \quad (2.56)$$

where Re extracts the real part of the element.

Considering the surface roughness at certain interface, a single absorbing layer is added at each interface to model the scattering loss [74]. The thickness  $d_R$ , the real part  $n_R$ , and the imaginary part  $k_R$  of refractive index of this additional layer are expressed as

$$d_R = 2\sigma \quad (2.57)$$

$$n = n_R - ik_R = \sqrt{\frac{n_a^2 + n_b^2}{2}} - i \frac{\pi}{2\sqrt{2}} \frac{d_R}{\lambda_0} \frac{(n_a - n_b)^2 (n_a + n_b)}{\sqrt{n_a^2 + n_b^2}} \quad (2.58)$$

where  $\sigma$  is the root-mean-square roughness of the surface,  $n_a$  and  $n_b$  are the refractive indices of adjacent materials.

Generally, a broadband high reflective thin-film coating is obtained from a multilayer structure with alternate layers of high and low refractive index dielectric materials when the thickness is determined through [75]

$$n_H d_H = n_L d_L = \frac{\lambda_0}{4} \quad (2.59)$$

where  $n_H$  denotes the high refractive index and  $n_L$  represents the low refractive index.  $\lambda_0$  is the central wavelength of this reflector. The relative bandwidth coefficient  $\frac{\Delta\lambda}{\lambda}$  is expressed as

$$\frac{\Delta\lambda}{\lambda} = \frac{4}{\pi} \arcsin \left( \frac{n_H - n_L}{n_H + n_L} \right) \quad (2.60)$$

## Chapter 3

# Chalcogenide fiber Fabry-Perot tunable filter

In this chapter, the first mid-infrared compatible Fabry-Perot tunable filter based on  $\text{As}_2\text{S}_3$  fibers is demonstrated. Dielectric multilayer thin-films are designed and deposited on the chalcogenide fiber facets, acting as high reflective mirrors. The first part of this chapter summarizes theory of the Fabry-Perot interferometer. The second part presents the fabrication process and experimental results. In the third part, a tunable fiber laser is assembled as an example of potential applications.

### 3.1 Introduction

The Fabry-Perot interferometer is an optical resonant cavity named after Charles Fabry and Alfred Perot since its first introduction in 1899. It primarily consists of two parallel reflectors where light is reflected back and forth successively in the cavity, leading to constructive interference at some wavelengths [7]. The implementation of Fabry-Perot interferometer to the present has not only contributed to wavelength-selective systems but also inspired a large variety of applications where refractive index, temperature, pressure, displacement, strain force, and humidity are measured [76–79]. The integration of a high finesse Fabry-Perot cavity also helps enhance the interaction between light and matter in a quantum system [80]. When incorporated with fiber technology, the reflector of a fiber Fabry-Perot interferometer is usually realized by Fresnel reflection, metallic mirror, dielectric multilayer thin-film coating, Sagnac loop mirror, or chirped Bragg grating. In addition to

the conventional Fabry-Perot cavity with parallel plane reflectors [81], diverse cavity structures have been proposed to reduce the insertion loss and enhance the cavity finesse. D. Hunger *et al.* demonstrated a concave cavity [80]. Y. Liu *et al.* presented elliptic, D-shaped, and crescent-shaped cavities [78]. Y. Jiang *et al.* adopted micro-lens to focus light in the cavity [82]. Other methods to match cavity mode and fiber mode include inserting a section of singlemode fiber, hollow-core fiber, or multimode fiber in the resonant cavity [79, 83].

Though fiber Fabry-Perot interferometer has been successfully demonstrated and commercialized over the past years, the operational wavelengths of these devices merely extend to 2.4  $\mu\text{m}$  because of the transparency window of silica glass. In comparison, chalcogenide glasses have transparency windows extending to 11  $\mu\text{m}$  ( $\text{As}_2\text{S}_3$ ) and 17  $\mu\text{m}$  ( $\text{As}_2\text{Se}_3$ ) as mentioned in chapter 1, which are good candidates for the mid-infrared spectral range that is utmost interest for a large variety of applications including chemical sensing, free-space communication, and surgical ablation. However, none of the published work before this thesis demonstrated a chalcogenide fiber Fabry-Perot tunable filter. It is the lack of such broadly tunable fiber filters compatible with the mid-infrared range that motivates the work carried out in this chapter.

In this chapter, I demonstrate the first Fabry-Perot tunable filter made of chalcogenide fibers terminated with high reflective multilayer thin-film coatings. Germanium (Ge) and calcium fluoride ( $\text{CaF}_2$ ) are selected for mid-infrared thin-film layers which are deposited alternately using the electron-beam evaporation method. The filter has a broad tunability  $>300$  nm by controlling the gap distance between two fiber facets. A thulium-doped fiber laser is demonstrated with a continuous wave output and a wavelength tunability from 1835 nm to 1920 nm.

## 3.2 Theoretical background

### 3.2.1 Fabry-Perot filter with a plane wave

Figure 3.1 shows the schematic of a traditional Fabry-Perot cavity, constructed by two parallel plane mirrors with their reflectance denoted by  $R_1$  and  $R_2$ . Considering a plane wave is successively reflected between two mirrors without excess loss of absorption and scattering,

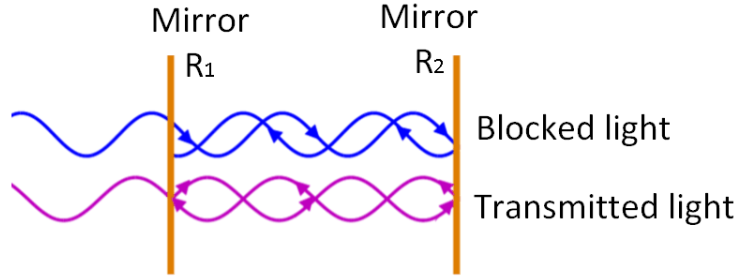


**Fig. 3.1** Schematic of a Fabry-Perot cavity with plane mirrors

the reflectance  $R$  and transmittance  $T$  of the Fabry-Perot cavity are expressed as [7]

$$R = \frac{R_1 + R_2 + 2\sqrt{R_1 R_2} \cos \varphi}{1 + R_1 R_2 - 2\sqrt{R_1 R_2} \cos \varphi} \quad (3.1)$$

$$T = \frac{(1 - R_1)(1 - R_2)}{1 + R_1 R_2 - 2\sqrt{R_1 R_2} \cos \varphi} \quad (3.2)$$

where  $\varphi$  is the roundtrip propagation phase shift in the cavity

$$\varphi = \frac{4\pi n d f \cos \theta}{c_0} \quad (3.3)$$

where  $n$  is the refractive index in the cavity,  $d$  is the distance between two mirrors,  $\theta$  is the incident angle,  $c_0$  is the light speed in vacuum, and  $f$  is the frequency of light. The transmittance reaches a maximum when  $\varphi = 2q\pi$ , where  $q$  is an integer, leading to the expression of resonant frequencies

$$f = \frac{q \cdot c_0}{2nd \cos \theta} \quad (3.4)$$

The free spectral range (FSR)  $f_{FSR}$  is then defined as the interval between two successive transmission peaks, leading to

$$f_{FSR} = \frac{c_0}{2nd \cos \theta} \quad (3.5)$$

Figure 3.2 shows the transmittance as a function of frequency. The quality of Fabry-Perot cavity is described by a parameter called finesse, which is the FSR divided by the

3-dB bandwidth of the transmission peak, corresponding to the reflectance of mirrors.

$$\mathcal{F} = \frac{f_{FSR}}{\Delta f_{FWHM}} = \frac{\pi}{2} \left[ \arcsin \left( \frac{1 - (R_1 R_2)^{1/2}}{2(R_1 R_2)^{1/4}} \right) \right]^{-1} \quad (3.6)$$

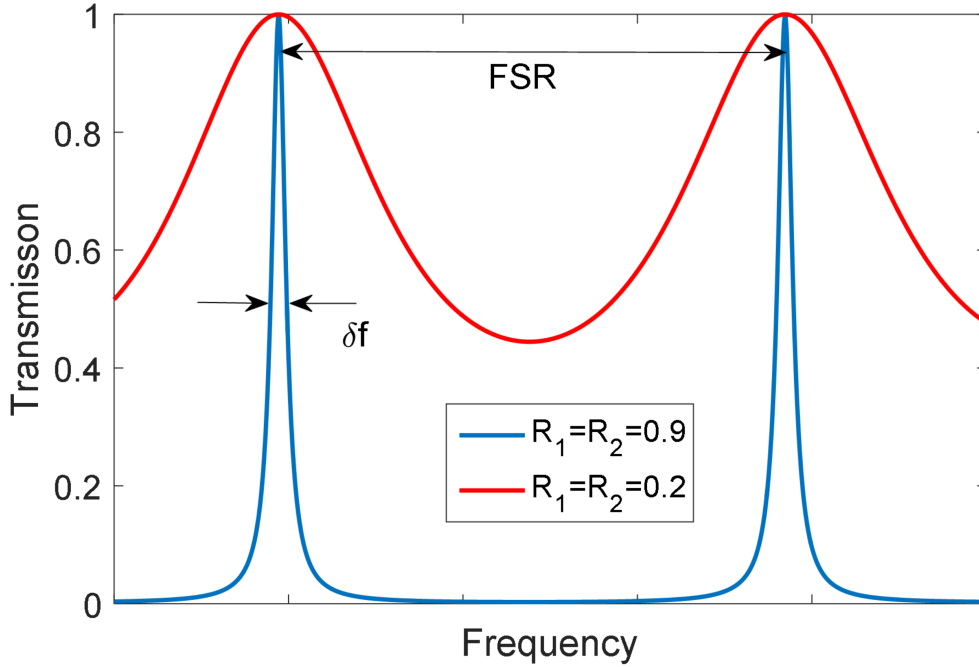


**Fig. 3.2** Transmission spectra of a Fabry-Perot filter without cavity loss.

### 3.2.2 Fabry-Perot filter with a Gaussian beam

However, the free space propagation in the Fabry-Perot cavity suffers from beam divergence, resulting in energy loss and mode mismatch to the fiber mode. The behavior of a diverging beam is usually approximated by a Gaussian beam expression. The polarization component along the propagation direction is negligible, which is the case of linearly polarized modes under the weakly guiding condition in an optical fiber. The fundamental Gaussian mode is used to represent the beam from a single mode fiber, expressed as

$$E(k, x, y, z) = \frac{q_0}{w_0 q(z)} \exp \left( -ik \frac{x^2 + y^2}{2q(z)} - ikz \right) \quad (3.7)$$

where  $k = \frac{2\pi n}{\lambda}$  is the wavenumber,  $x$  and  $y$  are transverse axes,  $z$  is the propagation axis,  $w_0$  is the waist radius that equates to the radius of fundamental fiber mode,  $q(z)$  and  $q_0$  are given by

$$q(z) = z + q_0 = z + i\frac{\pi w_0^2}{\lambda} \quad (3.8)$$

To incorporate with the multilayer system, Eq. 3.7 is decomposed into a two-dimensional angular distribution of plane waves by applying Fourier transform function [84]

$$\begin{aligned} \tilde{E}(k, k_x, k_y, z) &= \iint E(k, x, y, z) e^{-i(k_x x + k_y y)} dx dy \\ &= -i\frac{2\pi q_0}{w_0 k} \exp\left(-i\frac{q(z)(k_x^2 + k_y^2)}{k} - ikz\right) \end{aligned} \quad (3.9)$$

where  $k_x$  and  $k_y$  are transverse wavenumbers. Because of the circular symmetry, Eq. 3.9 is reduced to

$$\tilde{E}(k, k_t, z) = -i\frac{2\pi q_0}{w_0 k} \exp\left(-i\frac{q(z)k_t^2}{k} - ikz\right) \quad (3.10)$$

with  $k_t^2 = k_x^2 + k_y^2$ . Then  $\theta$  in Eq. 2.50 is linked to  $k_t$  with the relation

$$\sin \theta = \frac{k_t}{k} \quad (3.11)$$

The transmission through the whole multilayer thin-film structure, including the cavity gap, is calculated following the matrix method in chapter 2.

Then the light is coupled to another single mode fiber with mode mismatch, where the coupling coefficient or transmittance is calculated by the overlap integral equation

$$T(\lambda) = \frac{|\int_0^k \tilde{E}_{out} \tilde{E}_{fiber}^* k_t dk_t|^2}{|\int_0^k \tilde{E}_{fiber} \tilde{E}_{fiber}^* k_t dk_t|^2} \quad (3.12)$$

where  $\tilde{E}_{fiber}$  denotes the fundamental fiber mode and  $\tilde{E}_{out}$  is the electric field after the whole multilayer structure.

### 3.3 Design and fabrication

Figure 3.3 shows the schematic of a fiber Fabry-Perot tunable filter made of  $\text{As}_2\text{S}_3$  fibers with core/cladding diameters of 6/170  $\mu\text{m}$ . High reflective thin-film coatings are designed to cover the spectral range of 1.1  $\mu\text{m}$ -2.8  $\mu\text{m}$  with quarter-wavelength thicknesses  $d_k = \frac{\lambda_0}{4n_k}$ . Fibers are attached to V-grooves and aligned face to face by fine-tuning the 5-axes translation/rotation stage.

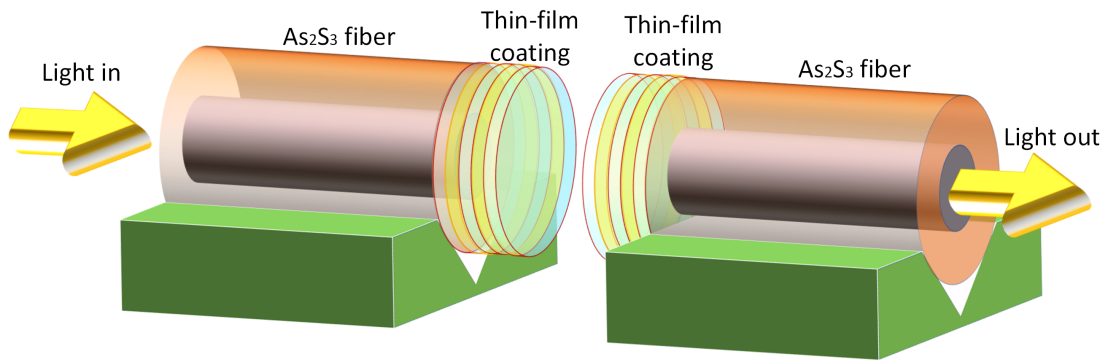


**Fig. 3.3** Schematic of a fiber Fabry-Perot filter

Regarding a suitable thin-film coating with mid-infrared compatibility, the dielectric materials are principally selected by factors such as transparency window, refractive index, mechanical stress, adhesion, toxicity, and cost. The most common materials in the mid-infrared range are summarized in Table 3.1, including  $\text{MgF}_2$ ,  $\text{CaF}_2$ ,  $\text{BaF}_2$ ,  $\text{SiO}_2$ ,  $\text{TiO}_2$ ,  $\text{Al}_2\text{O}_3$ ,  $\text{ZnS}$ ,  $\text{ZnSe}$ ,  $\text{CdTe}$ ,  $\text{Si}$ , and  $\text{Ge}$  [85]. The durability, stress, and optical property of a thin-film also vary with deposition technologies, where the microstructural growth process plays a key role [86]. Many excellent reviews have been published discussing the parameters such as substrate, temperature, pressure, deposition rate, surface roughness, contamination, energetic particle bombardment, and annealing condition that affect the process of nucleation, island growth, coalescence, and film growth [87–89]. In this work, I choose the electron-beam evaporation method because a large chamber volume is suitable for the fiber holder, the high deposition rate leads to a reasonable processing time of multilayer thin-films, and it is a relatively cheap method compatible to a considerable amount of materials. According to the electron-beam evaporation system in the laboratory,  $\text{ZnS}$ ,  $\text{ZnSe}$ , and  $\text{CdTe}$  are avoided because they all decompose during evaporation, leading to high vapor pressure,

while the condensed residuals on the chamber wall will be reintroduced to contaminate other thin-films [73]. Special precautions should be taken when exposing these materials to the atmosphere, preventing toxic compositions. Otherwise, strict disposal regulation should be followed in a shared environment. Multilayer high reflective coating consisting of  $\text{MgF}_2$  and  $\text{TiO}_2$  is found with severe delamination due to high tensile stress in the  $\text{MgF}_2$  layer, in line with the report of Muallem *et al.* [90]. Multilayer coating composed of  $\text{CaF}_2$  and  $\text{TiO}_2$  leads to a rough surface and much lower reflectance than the theoretical value. Finally, it is the combination of  $\text{CaF}_2$  as low refractive index material and Ge as high refractive index material that results in a stable and high reflective thin-film coating, where the large refractive index contrast is favored for less total thickness and broader reflection spectral bandwidth compared to other common materials. According to literature,  $\text{CaF}_2$  has a transparency window up to 12  $\mu\text{m}$  and a refractive index of 1.42 at a wavelength of 2  $\mu\text{m}$ , while Ge has a transparency window up to 23  $\mu\text{m}$  and a refractive index of 4.10 at a wavelength of 2  $\mu\text{m}$  [85].

**Table 3.1** Properties of common mid-infrared materials

Material	Refractive index at 2 $\mu\text{m}$	Transmission wavelength range
ZnS	2.28	0.4 $\mu\text{m}$ -15.0 $\mu\text{m}$
ZnSe	2.44	0.6 $\mu\text{m}$ -21.0 $\mu\text{m}$
CdTe	2.70	0.9 $\mu\text{m}$ -15.0 $\mu\text{m}$
$\text{Al}_2\text{O}_3$	1.73	0.2 $\mu\text{m}$ - 6.5 $\mu\text{m}$
SiO	1.85	0.7 $\mu\text{m}$ - 9.0 $\mu\text{m}$
$\text{TiO}_2$	2.40	0.4 $\mu\text{m}$ - 6.2 $\mu\text{m}$
$\text{CaF}_2$	1.42	0.1 $\mu\text{m}$ -12.0 $\mu\text{m}$
$\text{BaF}_2$	1.46	0.2 $\mu\text{m}$ -15.0 $\mu\text{m}$
$\text{MgF}_2$	1.37	0.1 $\mu\text{m}$ - 7.5 $\mu\text{m}$
Si	3.44	1.0 $\mu\text{m}$ - 9.0 $\mu\text{m}$
Ge	4.10	1.8 $\mu\text{m}$ -23.0 $\mu\text{m}$
GaAs	3.33	1.0 $\mu\text{m}$ -16.0 $\mu\text{m}$
NaCl	1.53	0.2 $\mu\text{m}$ -18.0 $\mu\text{m}$

Figure 3.4 depicts the schematic of an electron-beam evaporation chamber.  $\text{As}_2\text{S}_3$  fibers are polished and attached to a holder where one end of the fiber is oriented vertically. The temperature of fiber facet is not additionally controlled, while it increases under the heat

flux radiated by evaporants. The holder is rotating to promote uniformity of the thin-film. Dielectric materials are vaporized by an electron-beam and subsequently condensed on fiber facets. A quartz crystal oscillator is used to monitor the layer thickness. The chamber pressure is kept under  $5 \times 10^{-6}$  Torr, where a low pressure is usually recommended for the high quality of a thin-film. The deposition rate is set at 0.2 nm/s. After deposition, no annealing process is applied. The above condition and procedure are not optimal, but feasible for  $\text{CaF}_2$  and Ge layers.

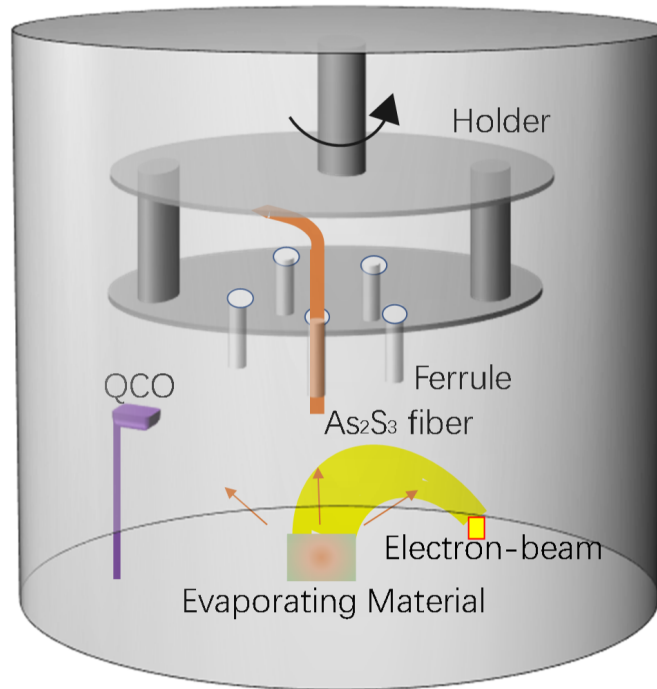


**Fig. 3.4** Electron-beam evaporation chamber for thin-film deposition. QCO: quartz crystal oscillator

In the first place, it is essential to calibrate the quartz crystal oscillator for thickness monitoring. Therefore, single layer of  $\text{CaF}_2$  is deposited on a silicon chip. Then, thickness and refractive index are determined by an ellipsometer, while the thickness is double-checked by a surface profiler (Dektak 150). The same verification is followed for Ge single layer. The average measured refractive index of  $\text{CaF}_2$  thin-film is 1.25 at a wavelength of  $2 \mu\text{m}$ , while the top part of the thin-film has a smaller refractive index than the bottom part. An identical phenomenon is reported by O. S. Heavens *et al.* [91] due to the porous structure of  $\text{CaF}_2$  layer. Dense films could be achieved by an ion-assisted deposition method. The

measured refractive index of Ge thin-film agrees with the theoretical value. After calibration of the quartz crystal oscillator, the accuracy of each layer is controlled within an error of 15 nm due to fluctuation of the deposition condition, leading to a shift of the reflection spectrum. Figure 3.5 shows reflection spectra of 5-layer thin-film coatings designed at a central wavelength of 1600 nm and 5000 nm respectively. The thickness of each layer is modified randomly within a deviation of 20 nm around the quarter wavelength thickness. Broad high reflective wavelength region is obtained, especially at the longer wavelength. So, the accuracy of layer thickness still meets the design requirement.

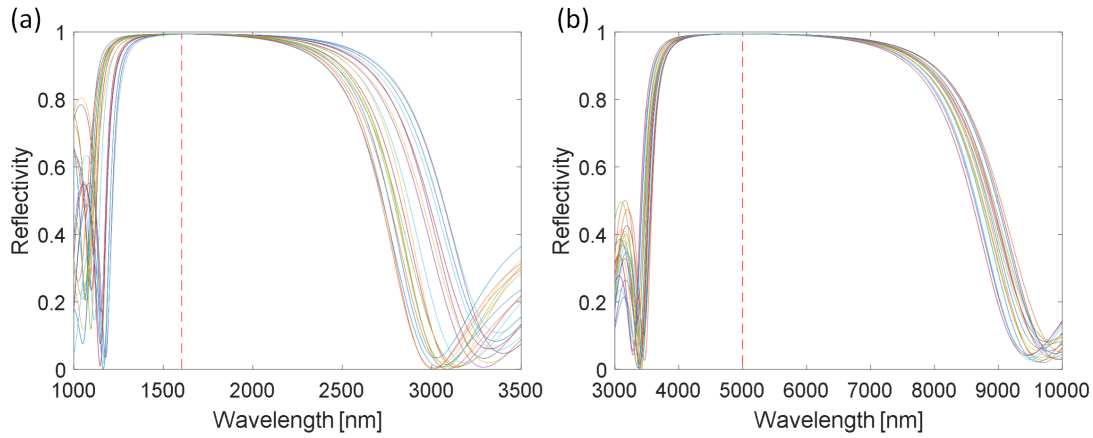


**Fig. 3.5** Reflection spectra of 5-layer thin-film coating designed at a central wavelength of (a) 1600 nm and (b) 5000 nm. Thickness of each layer is modified within a random deviation of 20 nm around the quarter wavelength thickness.

The central wavelength of the reflection coating is arbitrary set to 1.5  $\mu\text{m}$  for ease of measurement, expecting a layer thickness of 288 nm for  $\text{CaF}_2$  and 91 nm for Ge. High reflective coatings are deposited on  $\text{As}_2\text{S}_3$  fiber facets with three alternate thin-film layers of “high-low-high” (HLH) refractive indices and five alternate layers of “HLHLH”.

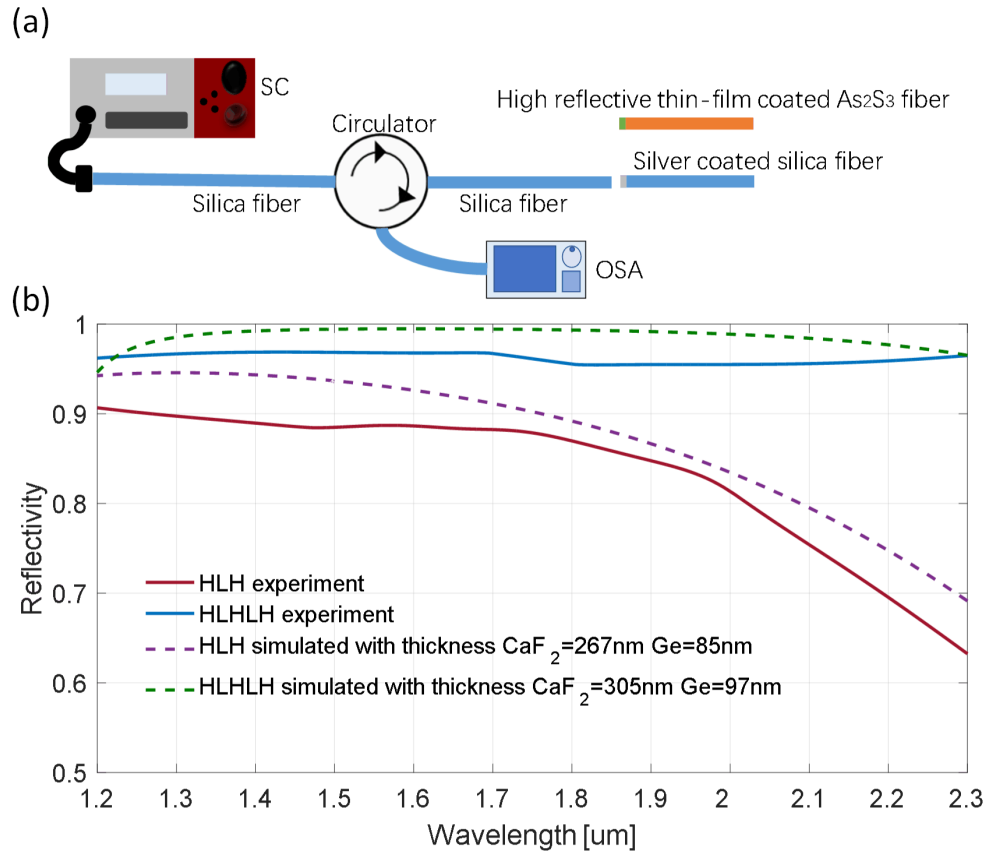
### 3.4 Experimental characterization

Figure 3.6a illustrates the schematic of a setup to characterize high reflective coatings. Broad-band light from a supercontinuum source is first coupled through a circulator and reflected by a silver layer with a thickness of 30 nm coated on a silica fiber facet, as a reference that provides 95% reflectivity across the spectral range. An optical spectral analyzer (OSA) is used to record the optical spectrum in the range of 1.2  $\mu\text{m}$ -2.3  $\mu\text{m}$ . Reflection spectrum of

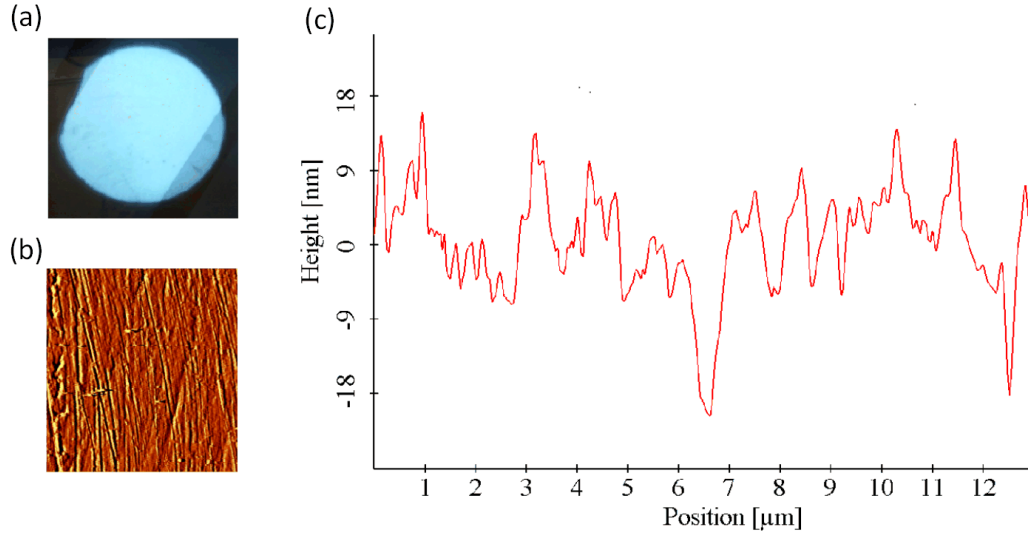
the high reflective thin-film coating on the  $\text{As}_2\text{S}_3$  fiber facet is then measured and calculated according to the reference. Due to the air gap, the measured reflectivity is expressed as

$$R_{\text{measure}} = R_{\text{silica}} + \frac{T_{\text{silica}}^2 R_{\text{coating}}}{1 - R_{\text{silica}} R_{\text{coating}}} \quad (3.13)$$

where  $R_{\text{silica}}$  and  $T_{\text{silica}}$  are reflectivity and transmissivity of the silica fiber facet in air.  $R_{\text{coating}}$  is the actual reflectivity of coating. When  $R_{\text{coating}} > 83\%$ , the difference between  $R_{\text{measure}}$  and  $R_{\text{coating}}$  is  $< 0.1\%$ . Thus, an approximation is made that  $R_{\text{coating}} \approx R_{\text{measure}}$ . Figure 3.6b shows reflection spectra of three-layer and five-layer coatings. The reflectivity is 90%



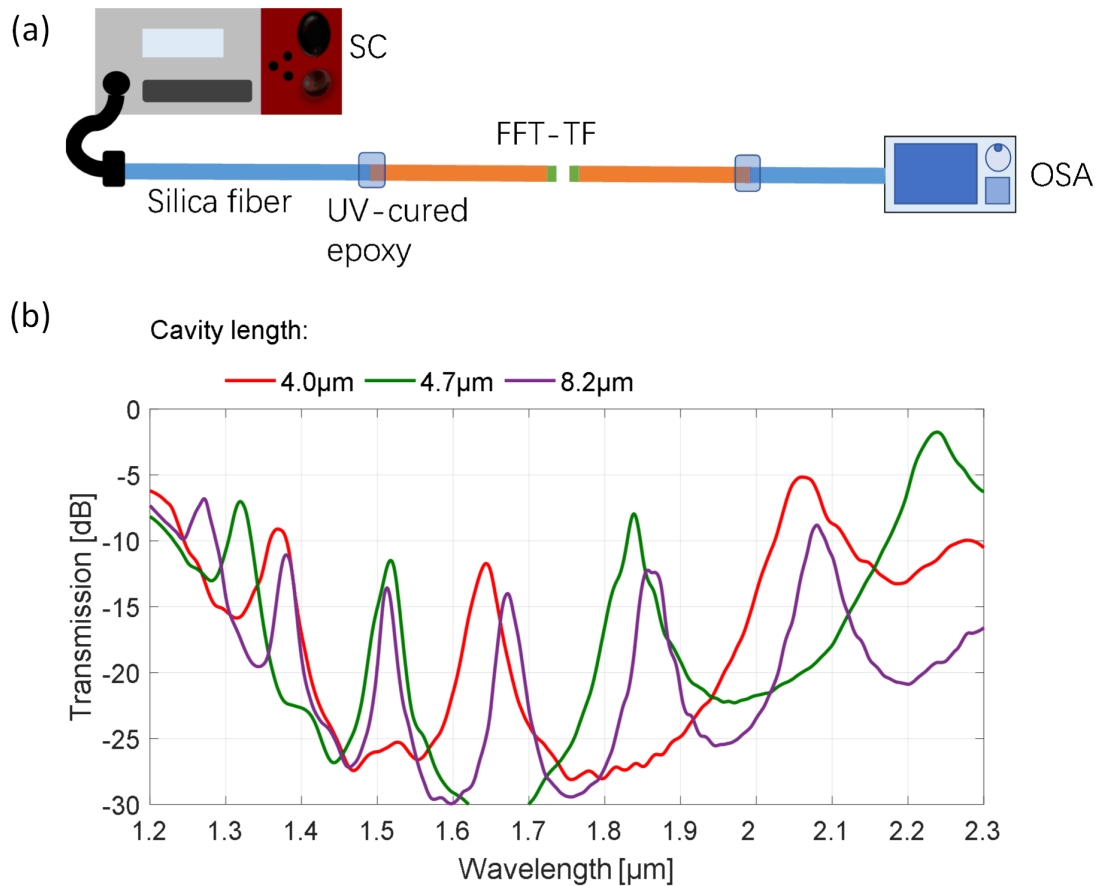
**Fig. 3.6** (a) Schematic of the setup to measure the reflection spectra of thin-film coatings. (b) Measured and simulated reflection spectra of thin-film coatings with 5-layers (HLHLH) and 3-layers (HLH) structures. H: high refractive index. L: low refractive index. SC: supercontinuum source. OSA: optical spectrum analyzer.



**Fig. 3.7** Fiber facet after polish observed by (a) camera and (b) atomic force microscopy. (c) Extracted roughness.

of the three-layer coating and 96% of the five-layer coating, which is about 4% lower than the theoretical value. Figure 3.7a shows the fiber facet after polish. Figure 3.7b and 3.7c show the surface roughness measured by an atomic force microscopy, which is about 10 nm and explains the reduction of reflectivity according to Eq. 2.57 and Eq. 2.58. The spectrum shift of the 3-layer high reflective coating is caused by the reduced thin-film thickness due to variation of depositing condition.

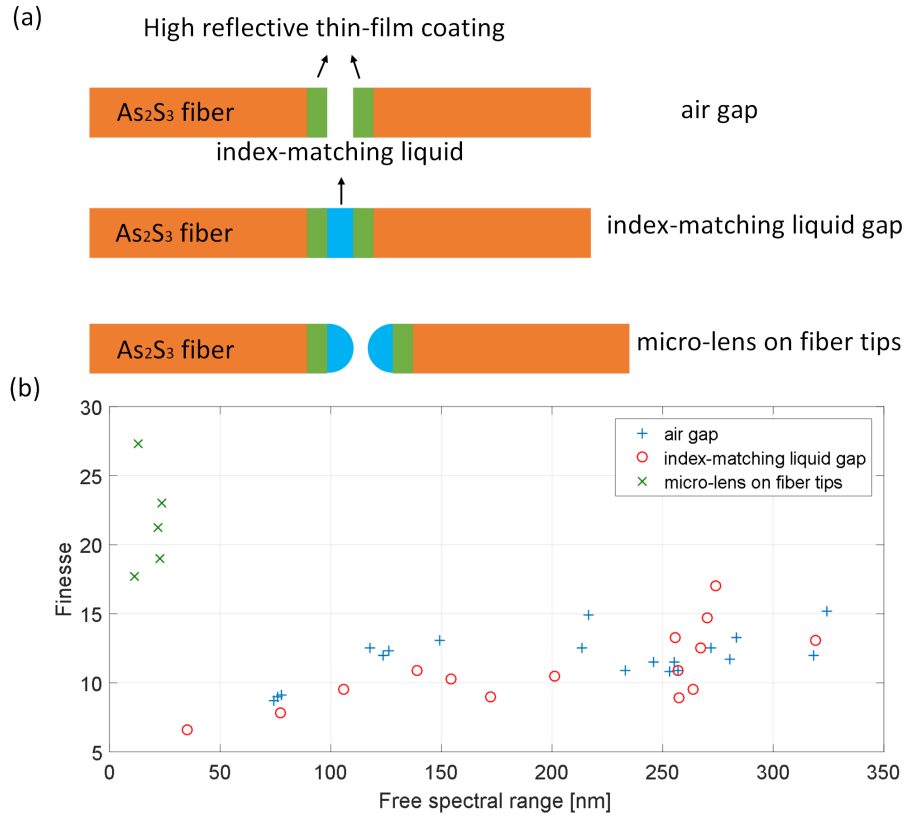
Figure 3.8a shows the schematic of a Fabry-Perot cavity consisting of two  $\text{As}_2\text{S}_3$  fibers coated with 5-layer high reflective thin-films. Fiber to fiber coupling is adjusted by 5-axes translation/rotation stages while the air gap between two fibers constitutes a Fabry-Perot cavity. A supercontinuum source and an OSA are used to measure the transmission spectrum of Fabry-Perot filter through the connecting silica fibers. Mechanical stability is ensured by ultraviolet (UV) ray cured epoxy at the joint between silica fiber and chalcogenide fiber, with a coupling loss of 2.5 dB where 0.3 dB loss comes from the Fresnel reflection at the interface, 0.7 dB loss is due to mode mismatch, and 1.5 dB loss attributes to the angular misalignment. Figure 3.8b plots the transmission spectra of a Fabry-Perot filter corresponding to an air gap distance of 4.0  $\mu\text{m}$ , 4.7  $\mu\text{m}$ , and 8.2  $\mu\text{m}$ . There is no noticeable multimode interference effect at the wavelength range of 1.2  $\mu\text{m}$ -2.3  $\mu\text{m}$ , despite that the single mode condition of  $\text{As}_2\text{S}_3$  fiber is satisfied at wavelength beyond 2  $\mu\text{m}$ . The Fabry-Perot has a free spectral



**Fig. 3.8** (a) Schematic of the setup to measure the transmission spectrum of fiber Fabry-Perot filter. (b) Measured transmission spectra of fiber Fabry-Perot filter at different cavity length. SC: supercontinuum source. OSA: optical spectrum analyzer. FFP-TF: fiber Fabry-Perot tunable filter.

range  $>350$  nm at a cavity length of 4  $\mu\text{m}$ , leading to a broad wavelength tunability. A finesse of 17 is also obtained at a cavity length of 4  $\mu\text{m}$ , limited by insufficient coupling of the diverging Gaussian beam propagation.

In addition to the air gap in Fabry-Perot cavity, figure 3.9a shows various coupling methods that are applied to enhance the coupling efficiency, including index-matching liquid and micro-lens. Figure 3.9b shows the corresponding finesse as a function of the free spectral range of each method. The smaller the free spectral range, the longer the cavity length. It is reasonable that finesse decreases when cavity length is longer due to the increasing coupling loss. The index-matching liquid has a refractive index of 1.47. However, it does



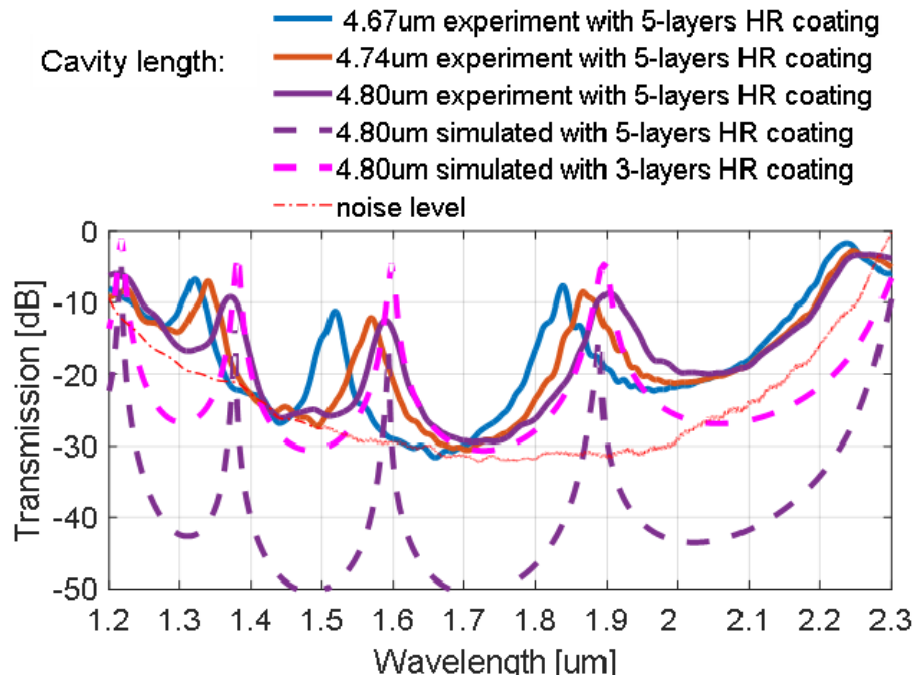


**Fig. 3.10** Measured and simulated transmission spectra of the fiber Fabry-Perot filter at a cavity length of 4.67  $\mu\text{m}$ , 4.74  $\mu\text{m}$ , and 4.80  $\mu\text{m}$ . HR: high reflective. Noise level is due to the sensitivity limit of optical spectrum analyzer.

the noise level of instrument. The insertion loss varies with the peak wavelength, attributed to the free space propagation of Gaussian beam between two flat reflectors. Figure 3.10 also shows the simulation results based on the Gaussian beam propagation. On the condition of 5-layer high reflective coatings, whose reflectivity is  $>99\%$ , the insertion loss is 16 dB at the central wavelength. On the condition of 3-layer high reflective coatings with a reflectivity of 95%, the insertion loss at the central wavelength is 5 dB. It is found that higher reflectivity leads to larger insertion loss and extinction ratio. The concave fiber facet could be used to reduce such insertion loss caused by the Gaussian beam propagation. The mismatch between transmission spectra of the experiment and simulation arises from the degradation of high reflective coatings as well as the proximity to the OSA instrumental noise floor.

Figure 3.11 shows the schematic of a thulium-doped fiber tunable laser operating in the continuous wave regime, where a chalcogenide fiber Fabry-Perot filter is inserted in the cavity to tune the lasing wavelength. A truly mid-infrared tunable laser could be constructed if all other components are mid-infrared compatible. A thulium-doped fiber with a length of

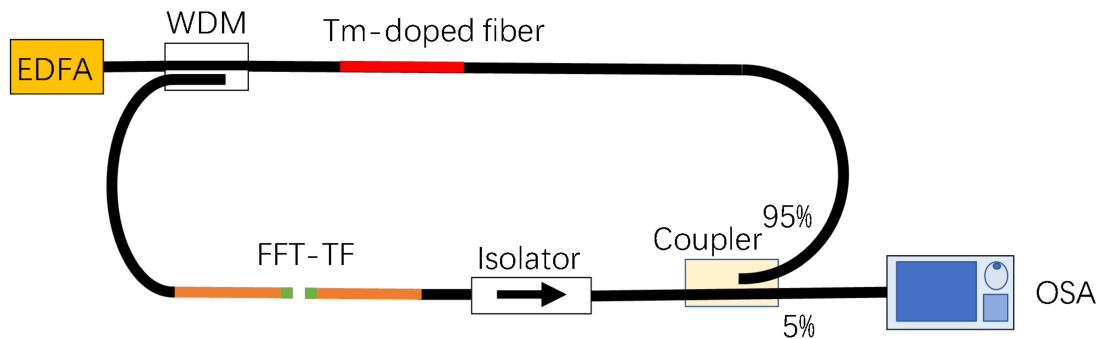


**Fig. 3.11** Schematic of a Tm-doped fiber tunable laser. EDFA: erbium-doped fiber amplifier. WDM: wavelength division multiplexer. FFT-TF: fiber Fabry-Perot tunable filter. OSA: optical spectrum analyzer.

30 cm is pumped by the spontaneous emission from an erbium-doped fiber amplifier via a 1550/1850 nm wavelength division multiplexer. An isolator with 38 dB isolation keeps unidirectional propagation in the ring cavity. Otherwise, a linear cavity constructed by two high reflective coatings is dominant. A 95/5 coupler is used to extract light from the cavity. The silica fibers are butt-coupled to chalcogenide fibers using UV-cured epoxy, leading to mechanical stability.

Figure 3.12 shows the spectra of the fiber laser at a pump power of 1.5 W while the lasing

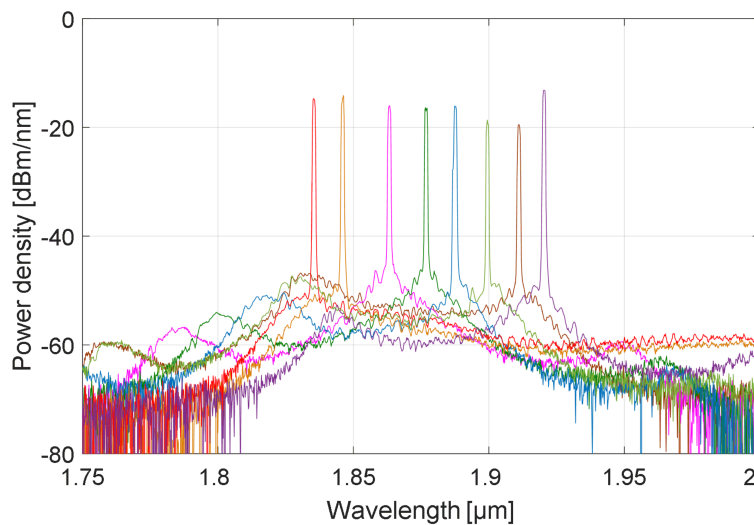


**Fig. 3.12** Spectra of the Tm-doped fiber tunable laser with a tunability from 1835 nm to 1920 nm.

wavelength is continuously tunable from 1835 nm to 1920 nm. The tunability is limited by the gain bandwidth of thulium.

### **3.5 Summary**

In conclusion, the first mid-infrared compatible Fabry-Perot tunable filter based on chalcogenide fibers is demonstrated with a continuous tunability  $>300$  nm. High reflective thin-film coating in the mid-infrared spectral range is designed and deposited on fiber facets using the electron-beam evaporation method. The selection of five alternate layers of Ge and  $\text{CaF}_2$  leads to mechanical stability and a high reflectivity of 96%, which could be further improved by reducing the fiber surface roughness and applying the ion-assisted evaporation method. Theoretical analysis and simulation of Gaussian beam propagation in the Fabry-Perot cavity show great accordance with the experimental results. Finally, a fiber tunable laser is assembled in tandem with this Fabry-Perot tunable filter. In the same way, a truly mid-infrared fiber laser could benefit from this Fabry-Perot filter as a building-block component.

## Chapter 4

# Tunable bandpass filter from multimode interference in chalcogenide fiber

In this chapter, a tunable bandpass filter is demonstrated based on a singlemode-multimode-singlemode fiber structure made of chalcogenide fibers. A continuous wavelength tunability  $>54$  nm and a hop wavelength tunability of 84 nm are obtained by mechanical bending. The first part of chapter covers the theoretical basics of a multimode interference filter. Second, the fabrication process of chalcogenide multimode fibers with different core diameters is presented. In the third part, various tuning properties of multimode interference filters are discussed, as well as design guidelines for a broadly tunable filter suitable for mid-infrared applications.

### 4.1 Introduction

As mentioned in chapter 1, the further exploitation in the spectral range of 2  $\mu\text{m}$ -12  $\mu\text{m}$  has led to increasing demand for mid-infrared compatible filters in applications of laser system, biomedical sensing, and spectroscopy. However, current mid-infrared tunable filters are mostly based on bulk or micro-electromechanical platforms [66, 67]. Though R. Ahmad *et al.* demonstrated a chalcogenide fiber Bragg grating filter [65] and I. C. M. Litter *et al.* demonstrated a chalcogenide acousto-optic filter [64], they are band-reject filters working

in reflection configurations, otherwise a circulator is needed for transmission applications. The chalcogenide Fabry-Perot bandpass filter presented in chapter 3 undergoes an expensive and complicated fabrication procedure for dielectric multilayer thin-film coatings. However, multimode interference (MMI) fiber filter is a type of bandpass filter features with ease of fabrication and low cost as well as other intrinsic advantages of a fiber platform including robustness, compactness, good beam quality, and ease of integration with fiber components.

MMI fiber filter is not only used in wavelength-selective systems [92], but also applied to measure displacement, temperature, and refractive index [93–95]. A conventional MMI fiber filter consists of a multimode fiber sandwiched between two singlemode fibers while wavelength tunability is achieved via diverse methods. A. Khattak *et al.* reported a MMI filter with a tunability of 9 nm via varying birefringence in the multimode fiber [96]. T. Walbaum *et al.* reported a tunability of 14 nm via mechanical bending of the multimode fiber [97]. J. E. Antonoi-Lopez *et al.* presented a tunability of 30 nm by adjusting the gap distance between multimode fiber and singlemode fiber [98]. X. Ma *et al.* presented a tuning range of 45 nm by shifting the liquid cladding of a no core fiber [99]. M. A. Fuentes-Fuentes *et al.* demonstrated a MMI fiber filter with a liquid core multimode fiber, where a tunability of 75 nm is obtained by controlling the temperature [100].

However, all previous MMI filters are made of silica fibers, limiting their transparency in the mid-infrared spectral range. Taking advantage of the transparency windows of chalcogenide glasses such as  $\text{As}_2\text{Se}_3$  up to a wavelength of 17  $\mu\text{m}$ , mid-infrared compatible MMI filter could be engineered. For this purpose, P. Wang *et al.* reported the first chalcogenide MMI device whose performance was limited by an insertion loss of 20 dB and an extinction  $<10$  dB [101]. Later, they demonstrated a chalcogenide MMI temperature sensor by measuring the dip deviation of transmission spectrum [102].

In this chapter, I demonstrate a MMI fiber bandpass filter assembled from  $\text{As}_2\text{Se}_3$  fibers. A continuous wavelength tunability  $>54$  nm and a hop wavelength tunability of 84 nm are obtained via mechanical bending of the multimode fiber. Transverse offsets of the input and output singlemode fibers, as a new degree of freedom to determine the filter property, are optimized to maximize the extinction ratio and set a desirable peak wavelength in the transmission spectrum. The mechanism responsible for MMI is summarized. Furthermore, MMI filters fabricated by multimode fibers with different core diameters are compared and discussed, leading to design guidance toward a broad tunability.

## 4.2 Theoretical background

### 4.2.1 Multimode interference

Figure 4.1 shows schematic of a MMI filter assembled with a singlemode-multimode-singlemode (SMS) fiber structure where core to core lateral offsets are applied at the input and output interfaces between singlemode fiber (SMF) and multimode fiber (MMF). Light propagating from input SMF is coupled to the MMF, exciting a set of eigenmodes at the interface, with their excitation coefficients determined by the input SMF diameter, MMF parameters (diameter and refractive index distribution), and the core to core offset position. Then, propagation of all guided modes along MMF gives rise to constructive interference and reproduction of the input light field, known as self-imaging [103], at the position  $z$  following

$$(\beta_{0,1} - \beta_{n,m}) \cdot z = 2\pi \cdot p \quad (4.1)$$

where  $\beta_{n,m}$  is the propagation constant of  $LP_{n,m}$  mode in the MMF,  $z$  is the propagation axis, and  $p$  is an integer indicating periodical self-imaging phenomena along MMF.

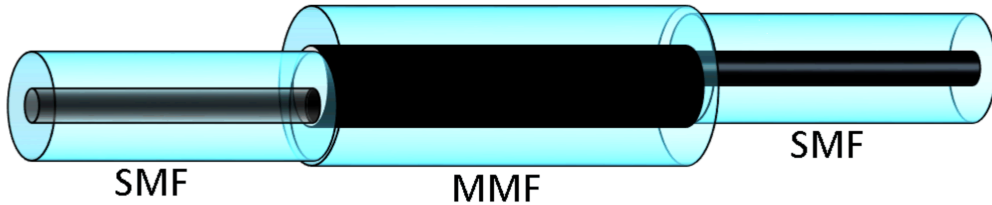


**Fig. 4.1** Schematic of a multimode interference filter consisting of singlemode-multimode-singlemode fiber structure with lateral core to core offsets at both input and output interfaces between singlemode fiber and multimode fiber.

As mentioned in chapter 1,  $LP_{n,m}$  modes are good approximations in a weakly guiding multimode fiber, where  $n$  and  $m$  are indices of the azimuthal and radial components, respectively. The field profile inside the MMF is expressed by the superposition of all excited guided modes [104]

$$E_{\text{MMF}}(r, \theta, z) = e^{-i\beta_{0,1}z} \sum_{n=-N}^N \sum_{m=1}^M C_{n,m}^{(\text{in})} F_{n,m}(r, \theta) e^{-i(\beta_{n,m} - \beta_{0,1})z} \quad (4.2)$$

## 4 Tunable bandpass filter from multimode interference in chalcogenide fiber 42

where  $C_{n,m}^{(\text{in})}$  and  $F_{n,m}(r, \theta)$  are excitation coefficient and field distribution of the LP $_{n,m}$  mode, respectively. The total number of azimuthal and radial modes are termed as  $2N + 1$  and  $M$ . The excitation coefficient  $C_{n,m}^{(\text{in})}$  is calculated through the field overlap integrals

$$C_{n,m}^{(\text{in})} = \frac{|\int_0^{2\pi} \int_0^\infty E_{\text{SMF}}(r - d_1, \theta) \cdot F_{n,m}^*(r, \theta) \cdot r dr d\theta|}{\int_0^{2\pi} \int_0^\infty |F_{n,m}(r, \theta)|^2 \cdot r dr d\theta} \quad (4.3)$$

where  $E_{\text{SMF}}$  is the field profile of fundamental mode in SMF and  $d_1$  is the lateral offset between input SMF and MMF. The transmission  $T_z^{(\text{out})}$  is expressed as

$$T_z = \frac{|\int_0^{2\pi} \int_0^\infty E_{\text{MMF}}(r, \theta, z) E_{\text{SMF}}^*(r - d_2) \cdot r dr d\theta|^2}{\int_0^{2\pi} \int_0^\infty |E_{\text{SMF}}(r, \theta)|^2 \cdot r dr d\theta \cdot \int_0^{2\pi} \int_0^\infty |E_{\text{MMF}}(r, \theta, z)|^2 \cdot r dr d\theta} \quad (4.4)$$

with  $d_2$  the lateral offset between output SMF and MMF.

According to Eq. 4.1, if all guided modes in the MMF are in phase, a perfect reproduction of the input field is obtained, leading to 100% of power transmittance neglecting the material loss. However, the propagation constants have no multiple relationships between each other, resulting in phase differences slightly deviating from multiples of  $2\pi$ . Then, a quasi-reproduction with a transmittance  $< 1$  is achieved as long as the dominant modes are in phase. As the MMF core diameter increases, the quasi-reproduction quality decreases because more modes are excited.

It is straightforward that  $(\beta_{0,1} - \beta_{n,m})$  varies at different wavelengths, leading to a wavelength-dependent power transmission function. Therefore, a spectral filter is constructed based on MMI effect where the peak transmission wavelengths are determined by the relative power and phase relationship among guided modes as well as the MMF length. Transverse offsets of the input and output SMFs provide a new degree of freedom to tune the excitation and coupling coefficients of the MMI filter.

At first, only LP $_{0,m}$  modes are excited without offset between input SMF and MMF. The propagation constant  $\beta_{0,m}$  is approximated by [105]

$$\beta_{0,m} \approx k_0 n_{\text{co}} - \left(2m - \frac{1}{2}\right)^2 \frac{\pi^2}{8k_0 n_{\text{co}} a^2} \quad (4.5)$$

leading to

$$(\beta_{0,1} - \beta_{0,m}) \cdot z = \frac{(2m - 2)(2m + 1)\pi}{16n_{\text{co}} a^2} \cdot \lambda_s \cdot z \quad (4.6)$$

## 4 Tunable bandpass filter from multimode interference in chalcogenide fiber 43

where  $n_{\text{co}}$  is the refractive index in fiber core,  $a$  is the radius of fiber core, and  $\lambda_s$  is the peak transmission wavelength. Substituting Eq. 4.6 into Eq. 4.1, the self-imaging length is obtained as [106]

$$L_s = \frac{16n_{\text{co}}a^2}{\lambda_s} \cdot p \quad (4.7)$$

A precise length of MMF within an accuracy of 100  $\mu\text{m}$  is required for a given peak transmission wavelength [104]. With a slightly increased  $\Delta L$ , the peak wavelength is shifted toward shorter wavelength, expressed as

$$\frac{\Delta\lambda}{\lambda_s} = -\frac{\Delta L}{L_s} \quad (4.8)$$

When offsets are introduced at both input and output interfaces between SMFs and MMF, additional insertion loss might be induced. However, the transmission spectrum, including peak wavelength, extinction ratio, and free spectral range, can also be adjusted. The tolerance of MMF length is no longer as strict as before, leading to flexibility in the design of a MMI filter.

### 4.2.2 Spatial frequency spectrum

At the end of MMF, where  $z = L$ , the phase term in Eq. 4.2 is expressed as

$$e^{-i(\beta_{n,m} - \beta_{0,1})L} = e^{-i\Delta\beta \cdot L} \quad (4.9)$$

where  $\Delta\beta$  is the difference between propagation constants. Applying a first-order Taylor series expansion leads to [107]

$$\Delta\beta = \frac{2\pi L \Delta n_{\text{eff}}}{\lambda} \approx \frac{2\pi L \Delta n_{\text{eff}}}{\lambda_x} - \frac{2\pi L \Delta n_{\text{eff}}}{\lambda_x^2} (\lambda - \lambda_x) \quad (4.10)$$

with  $\Delta n_{\text{eff}}$  the difference of effective refractive index at the reference wavelength  $\lambda_x$  of the Taylor series. The first term in Eq. 4.10 is a constant for a specific pair of modes. The second term of Eq. 4.10 leads to the definition of spatial frequency  $\xi = \frac{L \Delta n_{\text{eff}}}{\lambda_x^2}$ , while  $\xi = 0$  refers to the fundamental mode. Thus, application of a Fourier transformation on the transmission spectrum of MMI filter leads to a spatial frequency spectrum, which is widely used to pick out the mode components in the multimode interference spectrum.

### 4.2.3 Mechanical bending of multimode fiber

As reported, wavelength tuning of the MMI filter is attained by mechanically bending the MMF. The refractive index distribution in a MMF then becomes asymmetric due to the induced curvature and stress-optic effect. The modified refractive index distribution is governed by [108, 109]

$$n' = n \cdot \left(1 + \frac{x}{R_{\text{eff}}}\right) \quad (4.11)$$

where  $n$  is the material refractive index,  $x$  is the transverse location with positive value at the outer side of bend, and  $R_{\text{eff}}$  is the equivalent bend radius induced by the stress, expressed as [108, 109]

$$R_{\text{eff}} = \frac{R}{1 - \frac{n^2}{2}[P_{12} - \nu(P_{11} + P_{12})]} \quad (4.12)$$

with  $R$  the real bend radius.  $\nu$  is the Poisson's ratio and  $P_{11}$ ,  $P_{12}$  are the material photoelastic tensor. The modified refractive index leads to varied propagation constants of guided modes in the MMF, as well as varied power transmission at each wavelength. Therefore, the transmission spectrum of MMI filter undergoes a shift, acting as a tunable filter.

Assuming the MMF bends circularly, the displacement is related to the curvature through a triangle relationship

$$\sin\left(\frac{L_0}{2R}\right) = \frac{L_0 - \Delta s}{2R} \quad (4.13)$$

where  $L_0$  is the length of a straight support beam with MMF attached to it,  $\Delta s$  is the translation displacement, and  $R$  is the curvature radius. Application of a polynomial approximation for small values of the sine function leads to

$$\Delta s \approx \frac{L_0^3}{24R^2} - \frac{L_0^5}{1920R^4} \quad (4.14)$$

Figure 4.2 shows the relationship between curvature and displacement, where the measured result accords with the theoretical analysis of Eq. 4.14. MMF with a large core diameter is more sensitive to the bending as a result of more perturbed modes and more intermodal conversion among the guided modes of MMF.

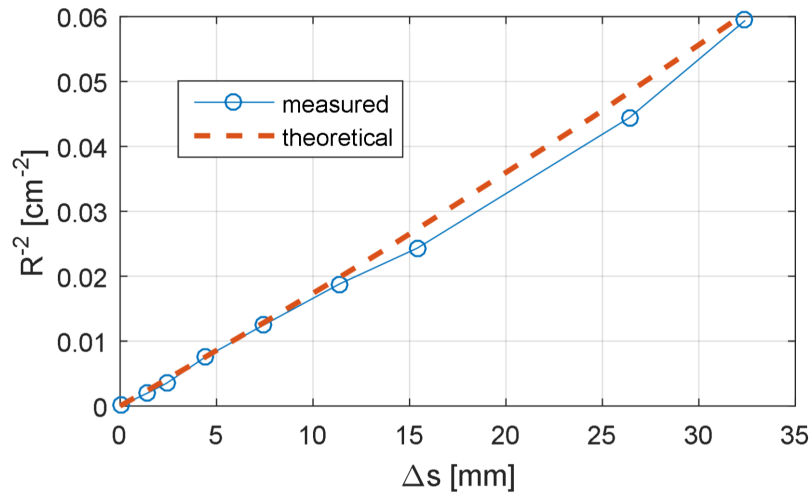


**Fig. 4.2** Theoretical and measured relationship between curvature and displacement

According to the complexity of analysis regarding a bent MMI filter with lateral offsets of both input and output SMFs, simulation methods are often used to calculate the transmission spectrum as an assistant in designing of a MMI filter. Typical simulation methods include guided mode propagation analysis and wide-angle beam propagation method.

### 4.3 Fabrication

In this work, a number of MMI filters have been fabricated for comparison following the structure in figure 4.1. The input and output fiber segments adopt identical chalcogenide ( $\text{As}_2\text{Se}_3$ ) singlemode fibers with a  $\text{NA} = 0.12$ . Mid-infrared compatible MMI filter is assembled by a chalcogenide ( $\text{As}_2\text{Se}_3$ ) step-index MMF with a  $\text{NA} = 0.2$ , a core diameter of  $22 \mu\text{m}$ , and a cladding diameter of  $170 \mu\text{m}$ . To vary the core diameter of MMF, the rest of MMI filters are assembled by three-layer step-index MMFs consisting of an  $\text{As}_2\text{Se}_3$  core, a cyclo olefin polymer (COP) cladding, and a polymethyl methacrylate (PMMA) protective coating. Figure 4.3 shows the schematic of setup for tapering chalcogenide fibers. One end of the fiber is fixed, and the other end is pulled at a controlled speed, while a heater is scanning along the fiber. The detailed fabrication procedure described by L. Li *et al.* is followed to taper the three-layer MMF [110], resulting in  $\text{As}_2\text{Se}_3$  core diameters of  $30 \mu\text{m}$ ,  $34 \mu\text{m}$ ,  $40 \mu\text{m}$ , and  $58 \mu\text{m}$ , where the diameter of COP cladding is four times of the corresponding core diame-

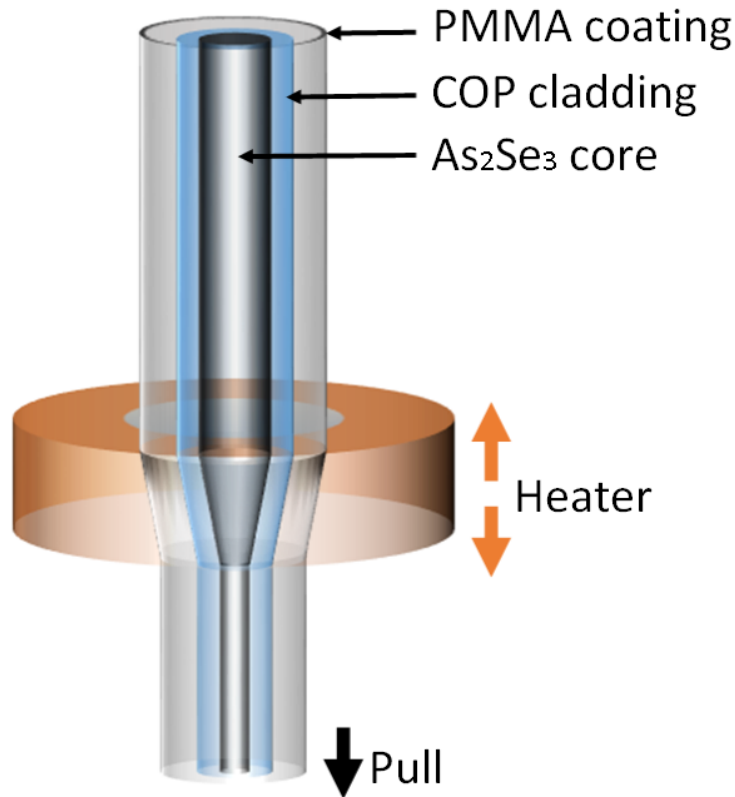


**Fig. 4.3** Schematic of setup for tapering the chalcogenide fiber with a COP cladding and a PMMA protective coating. One end of the fiber is fixed, and the other end is pulled at a controlled speed, while a heater is scanning along the fiber.

ter. The COP has a transparency window up to  $2.2 \mu\text{m}$ , resulting in MMFs not compatible to the mid-infrared spectral range. However, COP-cladded MMFs are conveniently tapered down to desirable core diameters that could be measured through a microscope, making it suitable for comparison among MMI filters with different core diameters.

SMFs are aligned to MMF with core to core lateral offsets at both input and output interfaces, where the offset positions are optimized by simultaneously monitoring the transmission spectrum during the alignment. To make the alignment and optimization easier, the input SMF is first aligned to the MMF via a 5-axes translation/rotation stage. The output beam from MMF is checked using a camera, where a clear core region at the MMF facet can be seen if the light is injected into the MMF fiber core. Then the output SMF is aligned

to the MMF using another 5-axes translation/rotation stage. A power meter connected to the output SMF indicates the output coupling efficiency. After the rough alignment of SMS fiber structure, the output SMF is connected to an OSA, where the transmission spectrum is obtained. Then, the offsets at both input and output SMF-MMF interfaces are finely optimized by observing the real-time transmission spectrum, until reaching a desirable target. Finally, the mechanical stability at fiber to fiber connections are ensured by UV epoxies. Because of the thermal expansion of UV epoxy, the transmission spectrum will shift during the UV light curing process. The following procedure should be applied to overcome this problem. First, applying a small amount of epoxies at both joint points between SMFs and MMF. After the first UV light curing period, applying more epoxies to both joint points, following a second UV light curing period. Then, the SMS fiber structure is connected while maintaining the transmission spectrum.

### 4.4 Experimental characterization

Figure 4.4 shows the schematic of setup to measure the transmission spectrum and tunability of a MMI filter. A supercontinuum source emits light with a broadband spectrum that is coupled to a MMI filter. An optical spectrum analyzer detects the transmission spectrum at the output. The MMI filter is attached on a flexible support beam which is bent under compression via the translation stages. The bending curvature in response to the displacement is calculated by Eq. 4.14. As a result, the spectral characterization in a range of 1600 nm-2100 nm is demonstrated.

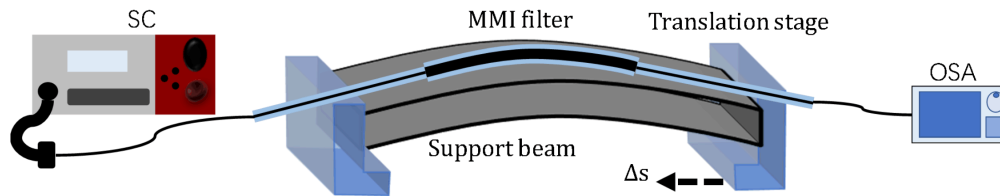


**Fig. 4.4** Schematic of the setup to characterize and bend the MMI filter. SC: supercontinuum source. OSA: optical spectrum analyzer. MMI: multimode interference.

Figure 4.5 shows the transmission spectra of MMI filters with various MMF lengths. These samples are assembled by an  $\text{As}_2\text{Se}_3$  MMF with a core diameter of 22  $\mu\text{m}$ , while the

length is arbitrarily cut to 104 mm, 69 mm, and 23 mm for comparison. The offset at the input SMF-MMF interface is introduced and fixed, while the offset at the output SMF-MMF interface is adjusted to minimize the insertion loss to a level  $<3$  dB. A free spectral range (FSR) of 50 nm, 78 nm, and 218 nm is obtained corresponding to a MMF length of 104 mm, 69 mm, and 23 mm, respectively. The FSR and 3-dB bandwidth decrease as the MMF length increases, acting similarly in the aligned condition without lateral offsets. In contrast, the extinction ratio is increased to 17 dB benefiting from the lateral offsets.

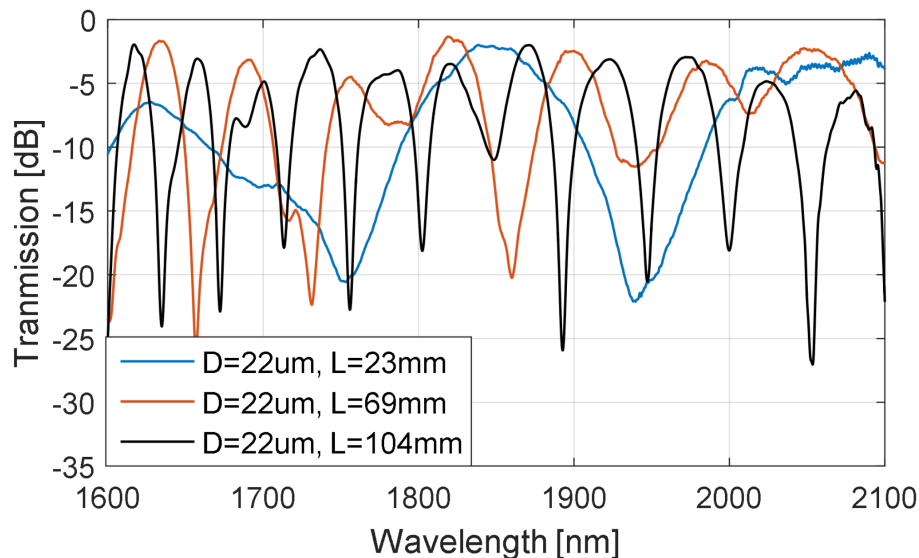


**Fig. 4.5** Transmission spectra of MMI filters with various MMF lengths. The  $\text{As}_2\text{Se}_3$  core/cladding diameters are 22  $\mu\text{m}$ /170  $\mu\text{m}$ . The lengths are 23 mm, 69 mm, and 104 mm, respectively.

After the MMF length is determined, the transmission spectrum is still adjustable in a wide range by tuning the core to core transverse offsets at the input and output SMF-MMF interfaces. Figure 4.6a shows the measured transmission spectrum of a MMI filter that is aligned without offset. The corresponding spatial frequency spectrum is calculated and presented by applying a fast Fourier transformation on the optical transmission spectrum. The MMF embedded in this MMI filter has a length of 67 mm and a core diameter of 40  $\mu\text{m}$ . In this aligned condition, an insertion loss  $<3$  dB, an extinction ratio of 4 dB, and a FSR of 30 nm are obtained. The spatial frequency spectrum has a dominant peak at  $\xi = 0$ , revealing that the fundamental mode in the MMF carries the dominant power while only a

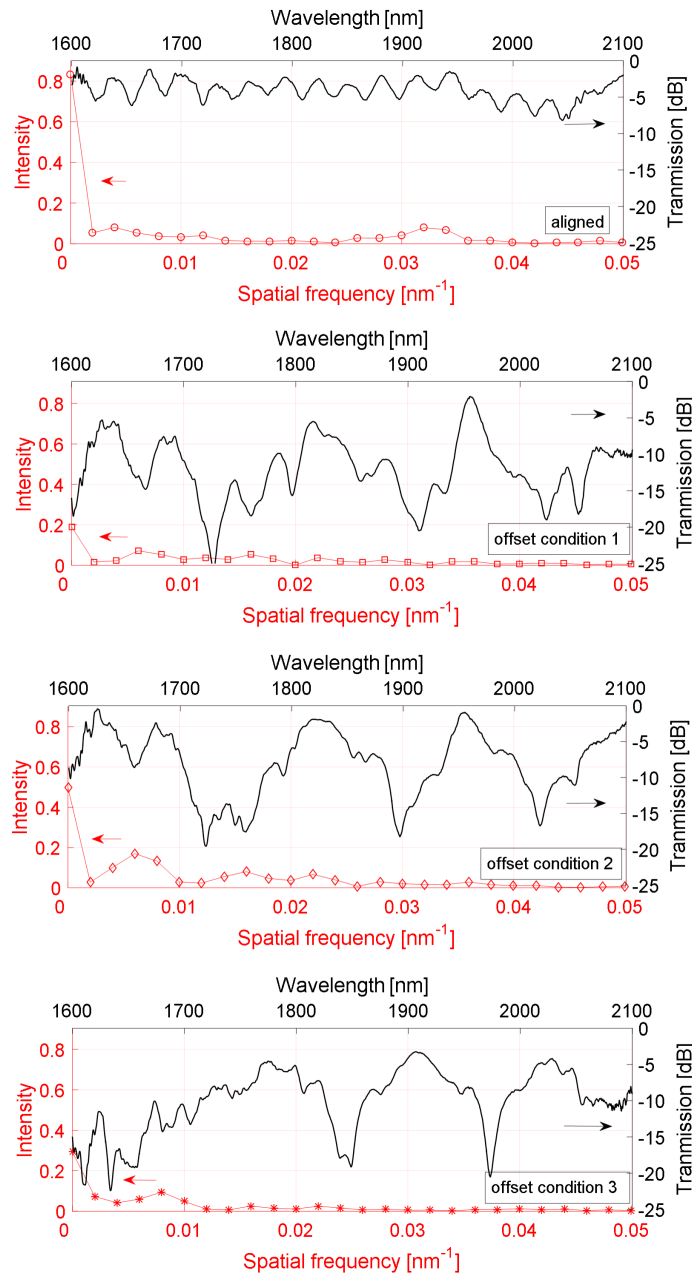


**Fig. 4.6** Transmission spectra and spatial frequency spectra of MMI filters in (a) aligned condition, (b) offset condition 1, (c) offset condition 2, and (d) offset condition 3. The MMF used in these samples has a length of 67 mm and a core diameter of 40  $\mu\text{m}$ .

small portion of the energy is distributed in higher-order modes. The large power differences between  $\text{LP}_{0,1}$  mode and  $\text{LP}_{n,m}$  modes lead to an indistinctive interference pattern as shown

in the optical transmission spectrum. Figure 4.6b-4.6d show the transmission spectra and associated spatial frequency spectra of MMI filters that are assembled by the identical MMF with a length of 67 mm and a core diameter of 40  $\mu\text{m}$ , but aligned with various core to core lateral offsets at both input and output SMF-MMF interfaces. The exact value of offset position is not measured but within a range of the MMF core region. When the insertion loss is kept  $<3$  dB, an extinction ratio  $>17$  dB and a FSR  $>110$  nm are obtained under different offset conditions. The variations of peak transmission wavelength and peak shape are distinguishable compared to Figure 4.6a. The spatial frequency spectra indicate that several modes preserve more equivalent power, leading to a strong interference pattern. It is concluded that offsets of the input and output SMFs provide a new degree of freedom to determine the characteristics of a MMI filter, which result in various transmission spectra in contrast to the aligned case without offset.

Figure 4.7 shows the transmission spectra of a MMI filter when the input SMF is transversely tuned and the output SMF is fixed at an offset position. The MMF used in this sample has a length of 74 mm and a core diameter of 34  $\mu\text{m}$ . As the transverse offset at

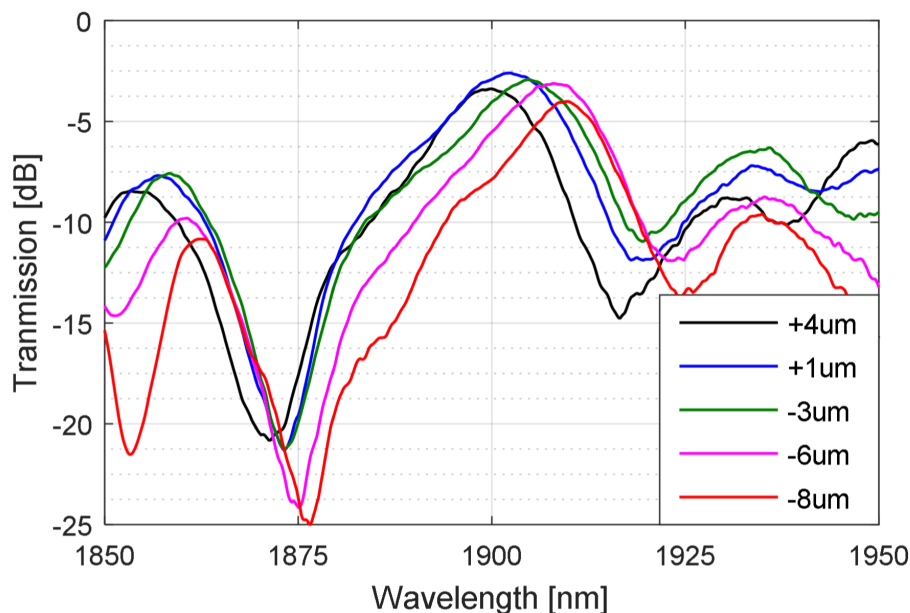


**Fig. 4.7** Transmission spectra of the MMI filter with different transverse offsets at the input SMF-MMF interface. The MMF used in this sample has a length of 74 mm and a core diameter of 34  $\mu\text{m}$ .

the input SMF-MMF interface is tuned from  $+4\ \mu\text{m}$  to  $-8\ \mu\text{m}$ , the peak transmission wavelength is continuously shifted from 1900 nm to 1910 nm, leading to a wavelength tunability of 10 nm. Instead, if the input SMF is fixed, the transverse tuning of output SMF also leads to a similar spectrum shift. Consequently, the length of MMF is no longer precisely enforced because the offset provides a flexible way to determine the peak transmission wavelength of a MMI filter.

A combination of figure 4.6 and figure 4.7 shows that the peak transmission wavelength of a MMI filter is not only adjustable in a broad wavelength range, but also continuously tunable in a small wavelength range, by varying core to core transverse offsets at the SMF-MMF interfaces. The impact of offsets as a new degree of freedom in the design of a MMI filter is demonstrated. All possible relations between offsets and transmission spectra should be investigated using the simulation method regarding a specific MMF.

When offsets of both input and output SMFs are optimized to get a small insertion loss, a large extinction ratio, a desirable peak transmission wavelength, and a suitable free spectral range, they are fixed using UV-cured epoxies to ensure the mechanical stability. Wavelength tuning of a MMI filter is achieved by a translation stage to bend the MMF as shown in Figure 4.4. The tuning property is not only affected by the offset condition but also related to the core diameter of MMF. Regarding MMI filters with various offset conditions and core diameters, two primary wavelength tuning properties are obtained. The first type is a continuous tuning process, where single transmission peak shifts continuously toward shorter wavelength and then decays. The second type is termed as a hop tuning process, where an initial transmission peak shifts toward shorter wavelength, and then hop a wavelength gap. Meanwhile, another peak at longer wavelength arises and shifts continuously to the initial peak wavelength. Thus, the total single wavelength operation range is expanded.

Figure 4.8 and figure 4.9 shows the first type of continuous tuning characteristics by mechanical bending. The MMI filter presented in figure 4.8 has a MMF with a length of 60 mm and a core diameter of  $34\ \mu\text{m}$ . The peak transmission wavelength shifts continuously from 1954 nm to 1902 nm accompanying a decay of 5 dB. Figure 4.8a is plotted on a logarithmic scale in order to observe the extinction ratio. The extinction ratio decreases from 17 dB to 8 dB during the tuning process due to intermodal power exchange. The 3-dB bandwidth of the MMI filter varies between 24 nm and 38 nm during the tuning process. Figure 4.8b shows the detailed relationship between peak wavelength and displacement of the translation stage, where the transmission is color-coded on a linear scale, leading to a

clear wavelength tunability of 52 nm.

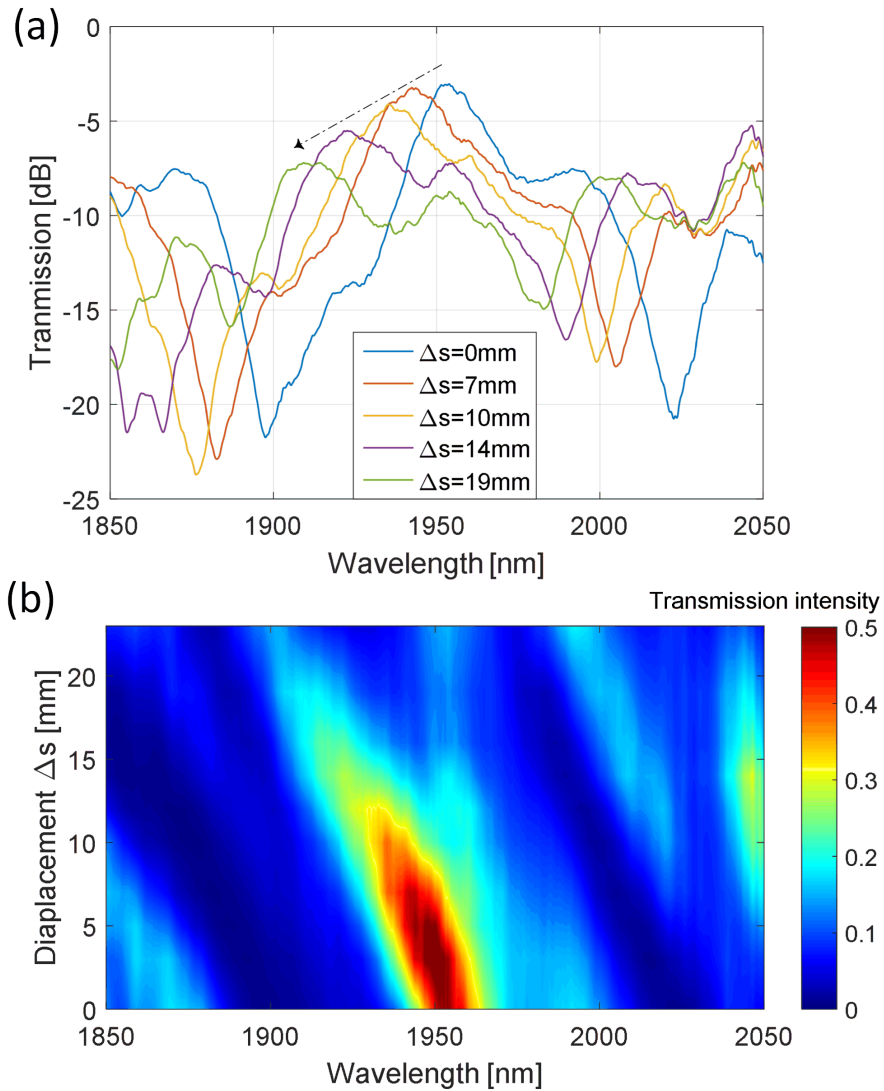


**Fig. 4.8** (a) Transmission spectra of the MMI filter under various bending condition. (b) The intensities of transmission spectra are color-coded on a linear scale. The MMF used in this sample has a length of 60 mm and a core diameter of 34  $\mu\text{m}$ .

The MMI filter presented in figure 4.9 has a MMF with a length of 37 mm and a core diameter of 34  $\mu\text{m}$ . Similarly, Figure 4.9a shows that the peak wavelength continuously shifts from 1768 nm to 1712 nm with a decay of 0.5 dB by bending the MMF. The extinction ratio decreases from 27 dB to 10 dB in response to the bending of MMF. Figure 4.9b clearly

#### 4 Tunable bandpass filter from multimode interference in chalcogenide fiber 53

shows a continuous wavelength tunability of 56 nm. The 3-dB bandwidth of this MMI filter varies from 29 nm to 41 nm during the tuning process. The comparison between two MMI filters reveals that it could reach similar wavelength tunability at different MMF lengths at certain offset condition, while the deformation of peak shape during the tuning process is affected by the offset condition. In the case with less random intermodal conversion induced

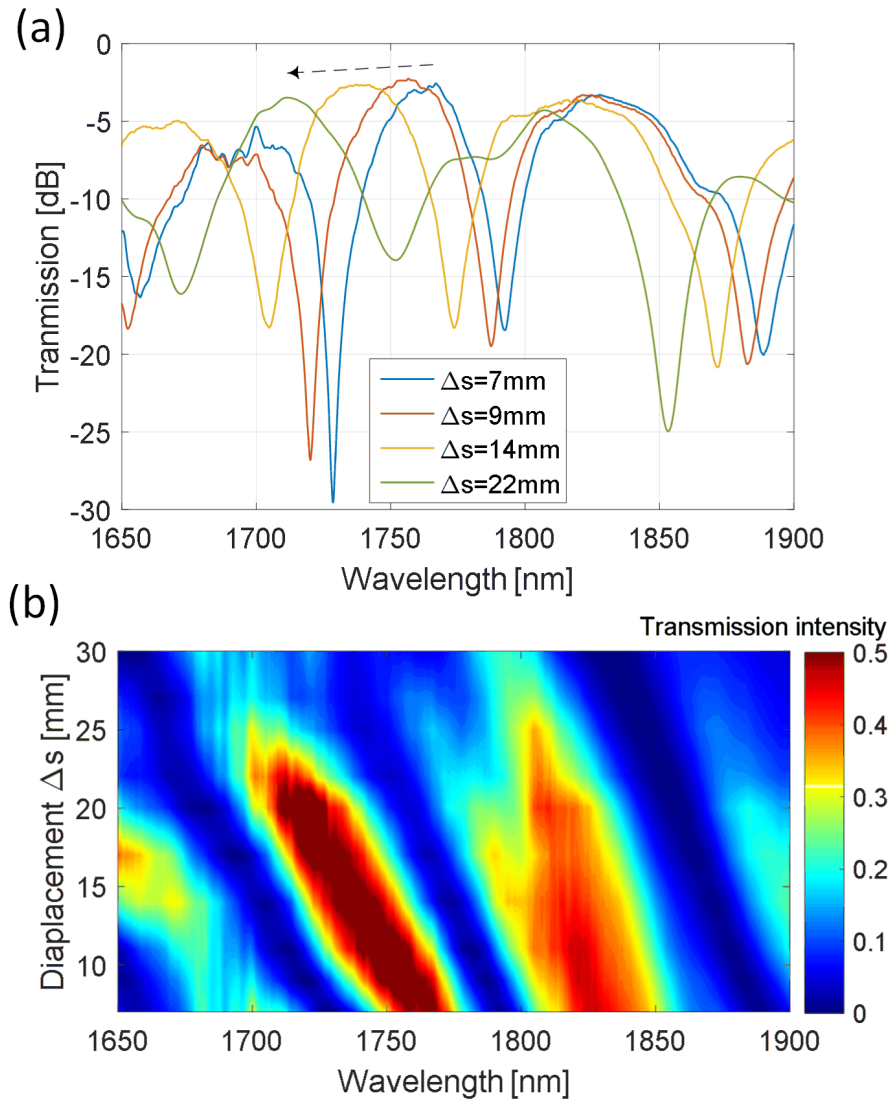


**Fig. 4.9** (a) Transmission spectra of the MMI filter under various bending condition. (b) The intensities of transmission spectra are color-coded on a linear scale. The MMF used in this sample has a length of 37 mm and a core diameter of 34  $\mu\text{m}$ .

by curvature, the peak shape is more immutable, leading to a smooth tuning process.

Figure 4.10 and figure 4.11 show the second type of hop tuning characteristics via mechanical bending. The MMI filter presented in figure 4.10 has a MMF with a length of 67 mm and a core diameter of 40  $\mu\text{m}$ . Figure 4.10a is plotted on a logarithmic scale where the transmission peak is located initially at a wavelength of 1952 nm. In the first period, the peak wavelength shifts continuously from 1952 nm to 1926 nm, and then hop to 1890 nm. At the same time, another peak emerges at a wavelength of 2010 nm. In the second period,

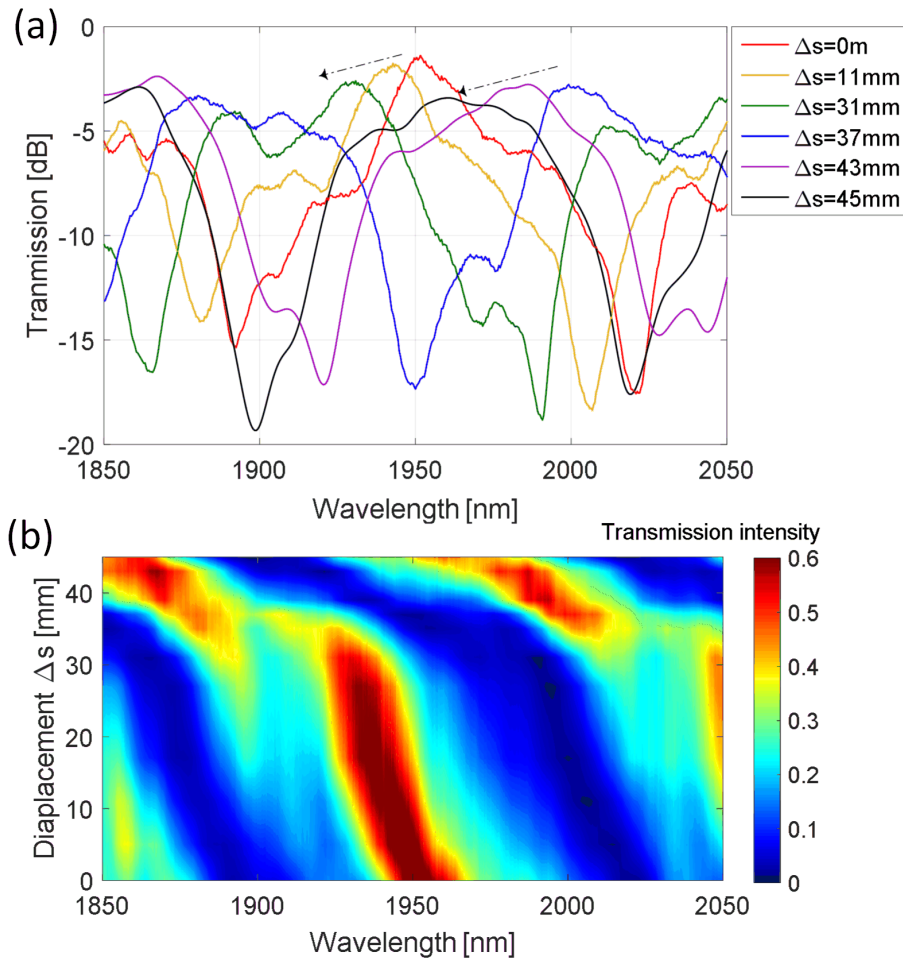


**Fig. 4.10** (a) Transmission spectra of the MMI filter under various bending condition. (b) The intensities of transmission spectra are color-coded on a linear scale. The MMF used in this sample has a length of 67 mm and a core diameter of 40  $\mu\text{m}$ . Offsets could affect the FSR.

the peak wavelength shifts continuously from 2010 nm to 1952 nm. Totally, the two continuous tuning ranges of 26 nm and 58 nm lead to a single wavelength operation covering 1926 nm-2010 nm, defined as a hop wavelength tunability of 84 nm. The insertion loss and extinction ratio only fluctuate in a small range of 2 dB. The 3-dB bandwidth varies from 26 nm to 68 nm during the tuning process. Figure 4.10b shows the detailed relationship between peak wavelength and displacement of the translation stage, where the transmission intensities are color-coded on a linear scale.

The MMI filter presented in figure 4.11 has a MMF with a length of 78 mm and a core

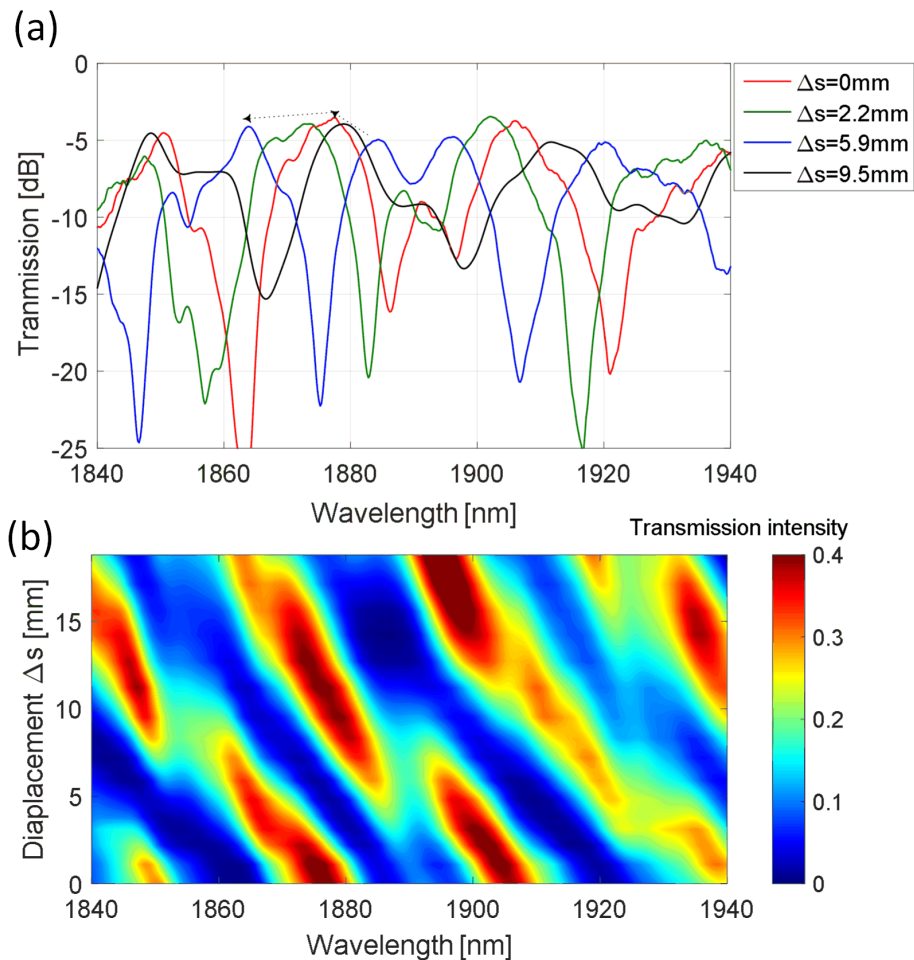


**Fig. 4.11** (a) Transmission spectra of the MMI filter under various bending condition. (b) The intensities of transmission spectra are color-coded on a linear scale. The MMF used in this sample has a length of 78 mm and a core diameter of 30  $\mu\text{m}$ . Offsets could affect the FSR.

diameter of 30  $\mu\text{m}$ . The MMF has a smaller core diameter, less offset, and longer length than the previous one, leading to a narrower FSR. Similarly, in the first period, the peak wavelength shifts continuously from 1876 nm to 1864 nm, and then hop to 1852 nm. In the second period, the peak wavelength at 1884 nm shifts continuously to 1876 nm. A hop tunability of 20 nm is obtained, covering the wavelength range of 1864 nm-1884 nm. The insertion loss and extinction ratio also vary in a small range. The MMI filter has a 3-dB bandwidth between 10 nm and 13 nm during the tuning process. The comparison among all previous MMI filters indicates that offsets play an important role in determining the tuning characteristics.

Figure 4.12a shows the relationship between peak wavelength and displacement of a MMI filter that is assembled by a MMF with a length of 78 mm and a core diameter of 58  $\mu\text{m}$ . A continuous wavelength tunability of 16 nm and a 3-dB bandwidth between 23 nm and 33 nm during the tuning process are obtained. The transmission peak is more sensitive to the bending curvature because more modes come into interaction, resulting in a fast decay of the transmission peak. Therefore, the continuous tunability is limited by the random intermodal conversion, which is prominent in a relatively large core MMF. In contrast, figure 4.12b shows the tuning characteristic of a MMI filter consisting of a MMF with a length of 104 mm and a core diameter of 22  $\mu\text{m}$ . This MMI filter has a 3-dB bandwidth between 24 nm and 26 nm during the tuning process and an extinction  $>27$  dB. The peak transmission wavelength shifts continuously from 1867 nm to 1813 nm with a decay of 2 dB. A tunability of 54 nm is demonstrated, limited by the FSR in this case. It is concluded that a MMF with a relatively small core diameter, referred as a few-mode MMF, usually leads to a MMI filter possessing a broad and continuous wavelength tunability.

Table 4.1 lists the properties of corresponding MMI filters presented in this chapter. The comparison among all MMI filters leads to following conclusions: (1) a long length of MMF leads to narrow bandwidth and small FSR which might limit the wavelength tunability, but has little effect on the tuning type; (2) offsets at both input and output SMF-MMF interfaces determine the excitation and coupling efficiencies of guided modes, benefiting for large extinction ratio, as well as relating to peak transmission wavelength, FSR, insertion loss, bandwidth, and tunability; (3) random intermodal conversion is responsible for the peak decay during bending, where a large core MMF with more excited modes usually has a narrow tunability, but a few-mode MMF ensures a broad and smooth tunability; (4) a hop tunability expands the single wavelength operation range. (5) In reality, angular misalignment and fiber

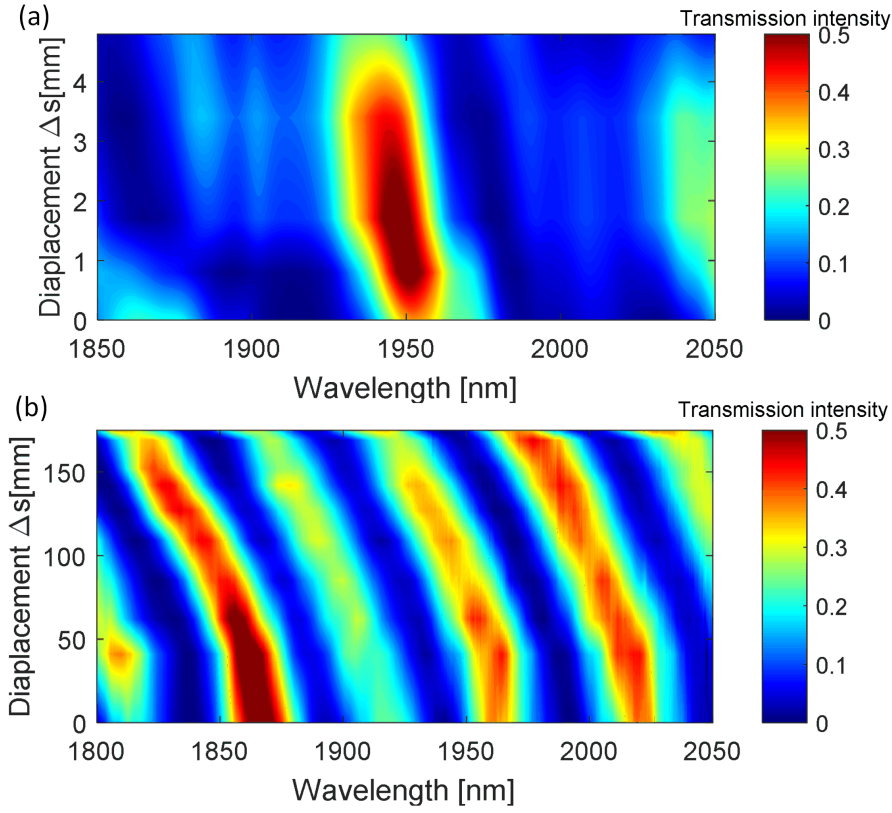


**Fig. 4.12** Relationship between the transmission spectrum and translation displacement using (a) MMF with a length of 78 mm and a core diameter of 58  $\mu\text{m}$  and (b) MMF with a length of 104 mm and a core diameter of 22  $\mu\text{m}$ . Offsets could affect the FSR.

birefringence might also cause difference between simulation and experiment.

**Table 4.1** Parameters of MMI filters

MMF core/cladding materials	Core diameter ( $\mu\text{m}$ )	MMF length (mm)	Bandwidth (nm)	Tunability (nm)
As <sub>2</sub> Se <sub>3</sub> /As <sub>2</sub> Se <sub>3</sub>	22	104	24-26	54
As <sub>2</sub> Se <sub>3</sub> /COP	30	78	10-13	12+8
As <sub>2</sub> Se <sub>3</sub> /COP	34	60	24-38	52
As <sub>2</sub> Se <sub>3</sub> /COP	34	37	29-41	56
As <sub>2</sub> Se <sub>3</sub> /COP	40	67	26-68	26+58
As <sub>2</sub> Se <sub>3</sub> /COP	58	78	23-33	16

## 4.5 Simulation

Since the few-mode chalcogenide MMF has demonstrated a continuous and broad wavelength tunability, simulation is made to explore possible influence of the offsets at both input and

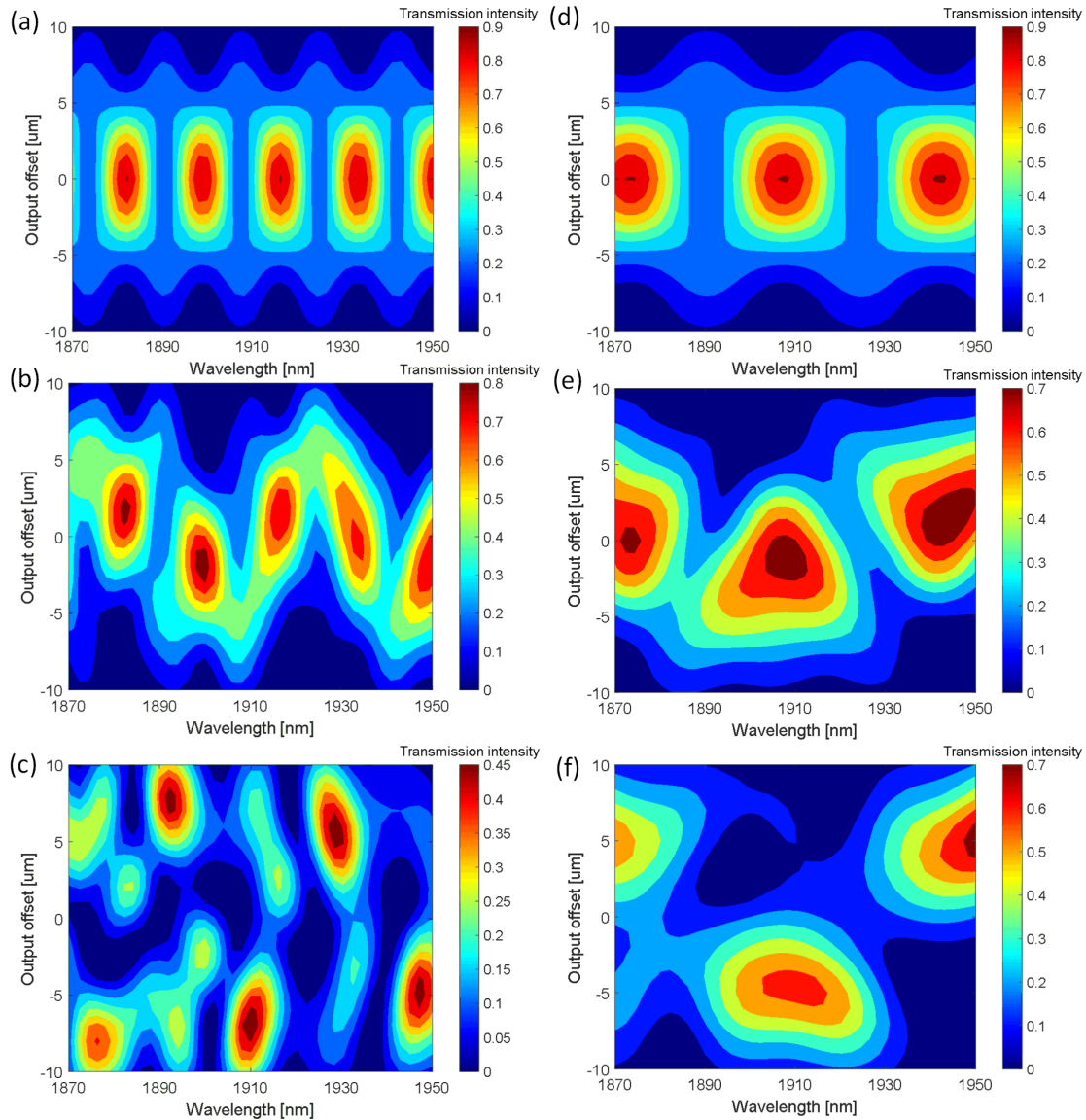


**Fig. 4.13** (a)-(c) A MMF with a length of 100 mm and a core diameter of 20  $\mu\text{m}$ . Input offset is (a) 0  $\mu\text{m}$ , (b) +2  $\mu\text{m}$ , and (c) +10  $\mu\text{m}$ . (d)-(f) A MMF with a length of 50 mm and a core diameter of 20  $\mu\text{m}$ . Input offset is (a) 0  $\mu\text{m}$ , (b) +2  $\mu\text{m}$ , and (c) +6  $\mu\text{m}$ .

output SMF-MMF interfaces. Figure 4.13a-4.13c show the transmission spectra of MMI filter using a MMF with a length of 100 mm and a core diameter of 20  $\mu\text{m}$ . The input offsets are fixed at 0  $\mu\text{m}$ , +2  $\mu\text{m}$ , and +10  $\mu\text{m}$ , respectively, while the output offsets are varied from -10  $\mu\text{m}$  to +10  $\mu\text{m}$ . Figure 4.13d-4.13f show the transmission spectra of MMI filter using a MMF at a shorter length of 50 mm. The input offset are fixed at 0  $\mu\text{m}$ , +2  $\mu\text{m}$ , and +6  $\mu\text{m}$ . The transmission is color-coded at various offset conditions. It is noted that the peak transmission wavelength could be designed at more positions by optimizing the offsets than the case without any offset. Specifically, at certain offset condition, the peak transmission wavelength could be tuned in a small range by only varying one offset.

### 4.6 Summary

In summary, I have demonstrated the first chalcogenide MMI tunable filter consisting of an  $\text{As}_2\text{Se}_3$  SMS fiber structure. The theoretical analysis of MMI effect and the relationship between bending curvature and translation displacement are presented. Transverse core to core offsets at the input and output SMF-MMF interfaces are introduced as a new degree of freedom in designing the transmission spectrum of a MMI filter. The spatial frequency spectrum is calculated to extract the mode contribution from the transmission spectrum. Wavelength tuning is achieved by bending the MMF, while the tuning characteristics are compared and discussed concerning fiber parameters and offset conditions. A MMI filter with a continuous wavelength tunability  $>54$  nm, an insertion loss  $<3$  dB, an extinction ratio  $>17$  dB, and a 3-dB bandwidth around 25 nm are obtained benefiting from a few-mode MMF. It is noteworthy that the central wavelength of this MMI filter could be customized at any position in the mid-infrared spectral range, leading to a simple, stable, and low-cost mid-infrared fiber tunable filter, as a promising building-block for diverse applications in the mid-infrared spectral range.

## Chapter 5

# All-fiber saturable absorber using nonlinear multimode interference in chalcogenide glass

In this chapter, the first chalcogenide fiber saturable absorber is demonstrated based on nonlinear multimode interference in a few-mode chalcogenide fiber. This saturable absorber also acts simultaneously as a wavelength bandpass filter in a resonant cavity. First, a theoretical analysis of nonlinear multimode interference is summarized. Then, the saturable absorber is characterized with a modulation depth of 10% and a peak saturation intensity  $<55 \text{ MW/cm}^2$ . Finally, a thulium fiber laser is passively triggered into a pulsed regime by inserting this saturable absorber in the laser cavity, leading to mode-locking in a tunable wavelength range of 1834 nm to 1895 nm. Pulse trains with conventional single pulse pattern and resembling pulse pattern are presented and discussed. The chalcogenide fiber saturable absorber shows great potential as a building-block for mid-infrared mode-locked fiber lasers.

### 5.1 Introduction

Over the past decades, pulsed laser sources have gained great attraction for technological and scientific applications such as material ablation [19], welding [111], LIDAR detection [112], optical communication [113], molecular spectroscopy [114], wavelength conversion [115], supercontinuum generation [116], and medical surgery [117]. The output wavelengths of pulsed

lasers have now extended to mid-infrared spectral range for the rising demand of mid-infrared applications. Saturable absorbers play a pivotal role in passively triggering pulses in a laser cavity. Examples of mid-infrared compatible saturable absorbers (SAs) include GaSb-based semiconductor mirror [118], low dimensional materials such as carbon nanotube [119], graphene [120], and black phosphorus [121]. Besides, techniques based on Kerr-effect are increasingly used as equivalent SAs including nonlinear polarization rotation [122], nonlinear amplifying loop mirror [123], and nonlinear mode coupling [124]. The Kerr-effect SA has a fast recovery time at femtosecond level. The recovery time of the SA has little influence on the pulse duration when the pulse is balanced by dispersion and nonlinearity in an anomalous dispersion cavity. However, it might affect the pulse duration at other conditions especially in a normal dispersion cavity [125]. Though the slow SA is more suitable for self-starting mode-locking, it could generate asymmetry pulses. The fast SA is more stable against pulse breaking [126].

Recently, incorporating fiber platform, all-fiber SAs based on nonlinear multimode interference have been demonstrated with fast response time, simple structure, and durability, while the operation wavelength covering the whole transparency window of silica glass. In 2013, E. Nazemosadat *et al.* proposed theoretical analysis and simulation results of a saturable absorber consisting of a graded-index multimode fiber (GIMF) [127]. Since then, J. Chen *et al.* demonstrated a mode-locked linear-cavity fiber laser with a GIMF based SA [128], H. Jiang *et al.* demonstrated a mode-locked thulium fiber laser with a tapered-GIMF SA [129], T. Chen *et al.* reported a SA made of a step-index multimode fiber (SIMF) [130], and D. Z. Mohammed *et al.* used a large diameter no core fiber (NCF) as a SA [131]. For these SAs, the saturable absorption wavelength depends on the length of MMF, which should be precisely determined to satisfy the demand.

Various hybrid structures have been proposed to overcome the stringent restriction of MMF length. Z. Wang *et al.* reported a stretched GIMF as a SA, which provides a way to control the length of GIMF [132]. H. Li *et al.* presented a SIMF-GIMF fiber structure as a SA, where the mode excitation condition is adjustable by bending the SIMF [133]. Similarly, T. Zhu *et al.* adopted a NCF-GIMF fiber structure for flexible saturable absorption [134]. F. Yang *et al.* presented a SA assembled by a micro-cavity based GIMF [135]. Z. Dong *et al.* demonstrated a mode-locked fiber laser with a SA constructed by offset splicing between two GIMFs [136]. Even though MMI SAs are based on silica fibers that limit their operation wavelength to 2.4  $\mu\text{m}$ , a vast range of mode-locking regimes have been explored using these

SAs such as the generation of soliton, bound soliton, stretched pulse, square-wave pulse, noise-like pulse, and harmonic mode-locking [134–138].

As an alternative solution for applications in the mid-infrared spectral range, chalcogenide glass offers attractive features as mentioned in chapter 1, leading to a transparency window up to 17  $\mu\text{m}$  ( $\text{As}_2\text{Se}_3$ ), a nonlinearity  $\sim 1000$  times higher than silica glass [30], and a high damage threshold of 3  $\text{GW}/\text{cm}^2$  [55]. In the previous chapter, an all-fiber chalcogenide bandpass filter based on the linear multimode interference effect has been demonstrated. Here, the multimode interference device is further investigated in a nonlinear regime, leading to the demonstration of first chalcogenide fiber SA. It also acts as a tunable bandpass filter simultaneously. A mode-locked fiber laser is passively triggered by inserting this SA into a fiber ring cavity. Both conventional single pulse pattern and resembling pulse pattern are discussed with variable pulse separations. The oscillation wavelength is tunable from 1834 nm to 1895 nm by bending the few-mode chalcogenide SIMF.

## 5.2 Theoretical analysis

As mentioned in chapter 4, light coupled from SMF to the MMF is decomposed into a set of eigenmodes as expressed in Eq. 4.2, where the amplitude of each mode is assumed constant during the propagation. However, in the nonlinear regime, power exchange between modes arises from intermodal nonlinearity, leading to an assumption of a slowly varying amplitude. Light filed as a superposition of all modes is expressed as

$$\tilde{E}(r, \omega) = \sum_m F_m(x, y, \omega) \tilde{A}_m(z, \omega) e^{-i\beta_m(\omega)z} \quad (5.1)$$

where  $F_m$  is the field profile,  $\beta_m$  is the propagation constant, and  $\tilde{A}_m$  is the amplitude of a specific mode labeled as index  $m$ . Following the analysis of Helmholtz equation, Eq. 2.18 is rewritten as

$$\nabla^2 \tilde{E} + \frac{n^2 \omega^2}{c_0^2} \tilde{E} = -\frac{\omega^2}{\epsilon_0 c_0^2} \tilde{P}_{\text{NL}} \quad (5.2)$$

where  $\tilde{P}_{\text{NL}}$  is the third-order nonlinear polarization in terms of in Eq. 2.14. Substituting Eq. 5.1 into Eq. 5.2 and neglecting second derivative of  $\tilde{A}_m(z, \omega)$  lead to [69]

$$\sum_m 2i\beta_m \frac{\partial \tilde{A}_m}{\partial z} F_m(x, y, \omega) \cdot e^{-i\beta_m(\omega)z} = \frac{\omega^2}{\epsilon_0 c_0^2} \tilde{P}_{\text{NL}} \quad (5.3)$$

Multiplying Eq. 5.3 with  $F_m^*$ , integrating over the transverse plane, and applying the orthogonal nature of eigenmodes, the mode amplitude is obtained as [69]

$$\frac{\partial \tilde{A}_m}{\partial z} = \frac{-i\omega^2 e^{i\beta_m(\omega)z}}{2\epsilon_0 c_0^2 \beta_m} \frac{\iint F_m^*(x, y, \omega) \cdot \tilde{P}_{\text{NL}} dx dy}{\iint F_m^*(x, y, \omega) \cdot F_m(x, y, \omega) dx dy} \quad (5.4)$$

After converting Eq. 5.4 back into the time domain, expanding  $\beta_m(\omega)$  in a Taylor series around the carrier frequency  $\omega_0$ , substituting the expression of  $P_{\text{NL}}$ , and neglecting Raman effect, Eq. 5.4 is modified as [69]

$$\frac{\partial A_m(z, t)}{\partial z} = -i \sum_{n=1}^{\infty} \frac{(-i)^n \beta_{mn}}{n!} \frac{\partial^n A_m}{\partial t^n} - i \sum_n \sum_p \sum_q \gamma_{mnpq} A_n^* A_p A_q e^{-i\Delta\beta_{mnpq}z} \quad (5.5)$$

where  $m, n, p,$  and  $q$  are the indices of modes, and

$$\begin{aligned} \Delta\beta_{mnpq} &= \beta_{p0} + \beta_{q0} - \beta_{m0} - \beta_{n0} \\ \gamma_{mnpq} &= \frac{\omega_0 \bar{n}_2 \iint F_m^*(x, y) F_n^*(x, y) F_p(x, y) F_q(x, y) dx dy}{c_0 \iint F_m^*(x, y) F_m(x, y) dx dy} \end{aligned} \quad (5.6)$$

Typically, Eq. 5.5 is known as the generalized multimode nonlinear Schrödinger equation, solved through numerical simulation such as the split-step Fourier method.

Analytically, when input power is relatively low, the MMI device acts as a bandpass filter due to wavelength-dependent self-imaging lengths where only dispersion effect dominates. Under the influence of increasing input power, the propagation constant of each mode varies in response to self-phase modulation and cross-phase modulation effects, shifting the transmission spectrum. Consequently, the MMI device experiences a higher transmittance at some wavelengths, manifesting itself as a SA [127]. At an intermediate high input power, the intermodal four-wave mixing effect rises and dominates, leading to power conversion among different modes in the MMF. Energy transfers from high-order modes to the fundamental

mode, leading to self-focusing effect [139]. Therefore, extinction ratio of the transmission spectrum decreases, resulting in saturable absorption at more wavelengths [127]. Different modes are self-trapped with each other when the intermodal nonlinearity compensates the diffraction, leading to a temporally localized energy packet. When transverse offset is introduced at the interface between input SMF and MMF, the pulse packet undergoes a zigzag propagation path in MMF [140]. At a sufficient high input power, the intermodal nonlinearity overwhelms the dispersion effect, leading to temporally and spatially locking among guided modes so that the propagation path becomes independent of the MMF structure [140]. As a result, the transmission spectrum of MMI device becomes almost flat where the extinction ratio is close to zero [127]. Insertion loss might also decrease at high input power due to an enhanced coupling at the interface between MMF and output SMF. Thus, saturable absorption is obtained at any wavelength.

### 5.3 Fabrication

Figure 5.1 shows the schematic of a MMI SA consisting of a singlemode-multimode-singlemode fiber structure. Both input and output silica SMFs have a core diameter of  $8\ \mu\text{m}$  and a numerical aperture  $\text{NA}=0.14$ . The  $\text{As}_2\text{Se}_3$  step-index MMF has a core diameter of  $18\ \mu\text{m}$  and a  $\text{NA}=0.22$ . Transverse core to core offsets at both input and output SMF-MMF interfaces are adjusted via two 5-axes translation stages and optimized by simultaneously observing the transmission spectrum until reaching a desirable peak transmission wavelength, a low insertion loss, an acceptable extinction ratio, and a suitable free spectral range. Then the fiber to fiber connections are fixed by the UV-cured epoxy following a procedure described in chapter 4, ensuring the mechanical stability.

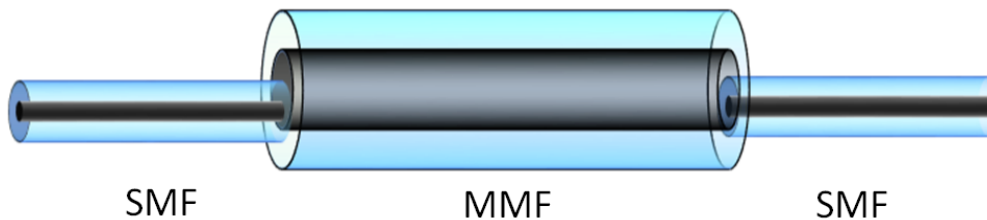


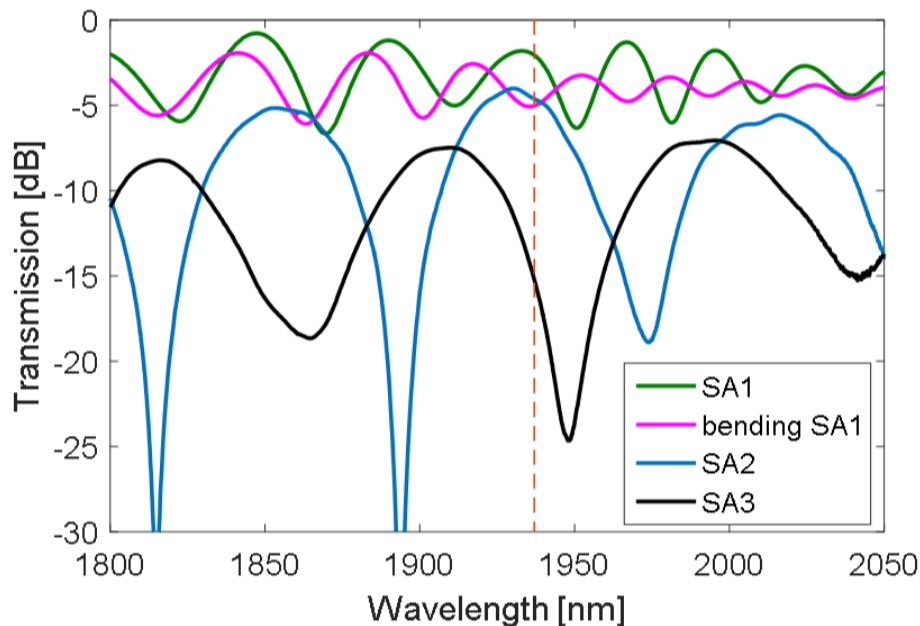
**Fig. 5.1** Schematic of a multimode interference saturable absorber.

A number of MMI SAs have been fabricated with arbitrary MMF lengths and different

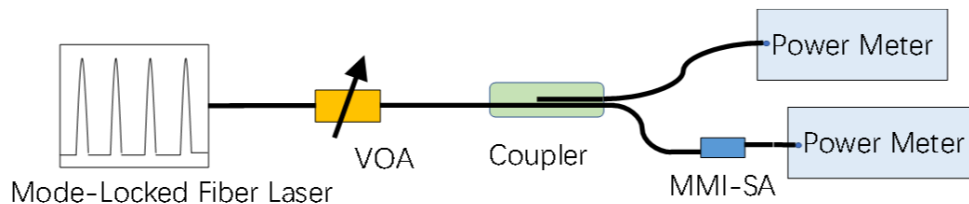
offset conditions, leading to various linear transmission spectra.  $SA_1$ ,  $SA_2$ , and  $SA_3$  have a MMF length of 52.5 mm, 65 mm, and 60 mm, respectively.

#### 5.4 Experimental characterization of saturable absorber

Figure 5.2 shows the measured linear transmission spectra of these MMI SAs.  $SA_1$  exhibits an insertion loss of 2.4 dB, an extinction ratio of 4.5 dB, and a FSR of 39 nm. The transmission spectrum shifts toward short wavelength via bending the MMF.  $SA_2$  shows an insertion loss of 4.4 dB, an extinction ratio  $>15$  dB, and a FSR of 75 nm.  $SA_3$  shows an insertion loss of 7.5 dB, an extinction ratio  $>15$  dB, and a FSR of 91 nm. The linear transmission spectrum is not only adjustable by varying offsets at SMF-MMF interfaces during the fabrication process, but also tunable by bending the MMF after fabrication. Therefore, the length of MMF is no longer crucial for saturable absorption to occur at a specific wavelength. As mentioned in chapter 4, a broad wavelength tunability is obtained thanks to a few-mode chalcogenide fiber, leading to much more flexibility in optimizing the MMI SA property after the fabrication.



**Fig. 5.2** Linear transmission spectra of saturable absorbers. These samples are fabricated with different offset conditions and MMF lengths.



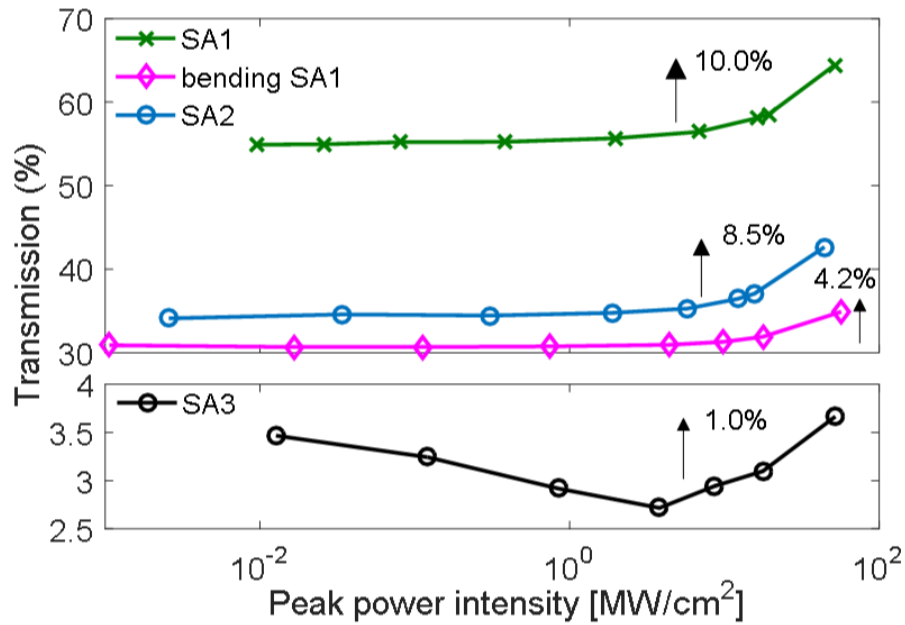
**Fig. 5.3** Schematic of the characterization setup for nonlinear transmission of saturable absorbers as a function of peak power intensity. VOA: variable optical attenuator. MMI-SA: multimode interference saturable absorber.

Figure 5.3 shows the schematic of setup to characterize a MMI SA. A mode-locked fiber laser transmits pulses with a duration of 800 fs, a repetition rate of 30.3 MHz, and a central wavelength of 1937 nm. A variable optical attenuator is used to control the power into a MMI SA, which is detected and calculated via a coupler and a power meter. MMI SA is inserted into the other output arm of the coupler and another power meter detects the transmitted power.

Figure 5.4 shows the transmission of MMI SAs as a function of input peak intensity. Saturable absorptions of SA<sub>1</sub>, SA<sub>2</sub>, and SA<sub>3</sub> are observed and compared at an operational wavelength of 1937 nm. With the input peak intensity varying in the range of 0-51 MW/cm<sup>2</sup>, SA<sub>1</sub> has a measured modulation depth of 10.0% and SA<sub>1</sub> in a bent status has a modulation depth of 4%. SA<sub>2</sub> exhibits a modulation depth of 8.5% and SA<sub>3</sub> shows a modulation depth of 1.0%. It is clear that the modulation depths could extend to higher values, given sufficient high input power. Regarding SA<sub>1</sub> and SA<sub>2</sub>, the input central wavelength is located near a peak wavelength in the linear transmission spectrum, indicating the possibility of a SA and a tunable bandpass filter simultaneously. SA<sub>3</sub> has a larger insertion loss compared to others, making it hard to get large modulation depth in the current input power range. At the beginning, saturable absorption might not occur at all wavelengths, depending on the relationship between modes as well as the offset condition. However, as mentioned in section 5.2 self-focusing and self-trapping effects might help trigger the saturable absorption effect and improve the performance of SA<sub>3</sub>. Typically, the nonlinear saturable absorption curve is fitted following a function [141]

$$T(I) = 1 - q \cdot e^{-I/I_{\text{sat}}} - a_{\text{ns}} \quad (5.7)$$

where  $I_{\text{sat}}$  is the peak saturation intensity,  $q$  is the estimated modulation depth, and  $a_{\text{ns}}$  is the



**Fig. 5.4** Nonlinear transmission of saturable absorbers as a function of peak power intensity.

nonsaturable loss. For instance, fitting parameters  $q = 0.14$ ,  $I_{\text{sat}} = 55 \text{ MW/cm}^2$ ,  $a_{\text{ns}}=0.31$  are obtained for SA<sub>1</sub> and  $q = 0.11$ ,  $I_{\text{sat}} = 38 \text{ MW/cm}^2$ ,  $a_{\text{ns}} = 0.55$  are obtained for SA<sub>2</sub>. The saturation intensity can be further reduced with proper engineering such as increasing the waveguide nonlinearity or extending the walk-off distance among guided modes. Thus, a small number of propagating modes in the MMF is beneficial for the design of a SA.

## 5.5 Experimental characterization of pulsed fiber laser

All previous MMI SAs are capable of triggering mode-locking and generating pulses while inserted into a fiber laser cavity. A mode-locked laser will establish a stable pulse pattern under the dynamic balance among cavity gain, loss, nonlinearity, and dispersion [142]. The output pulse shape is determined by a lot of factors such as modulation depth of SA, arrangement of components in the cavity, cavity dispersion map, pump power, and random polarization fluctuation. In the following test, a net normal dispersion cavity is assembled due to its advantage in generating high energy pulses. Figure 5.5 shows the schematic of a passively mode-locked fiber laser with a ring configuration. A thulium-doped fiber (TDF)

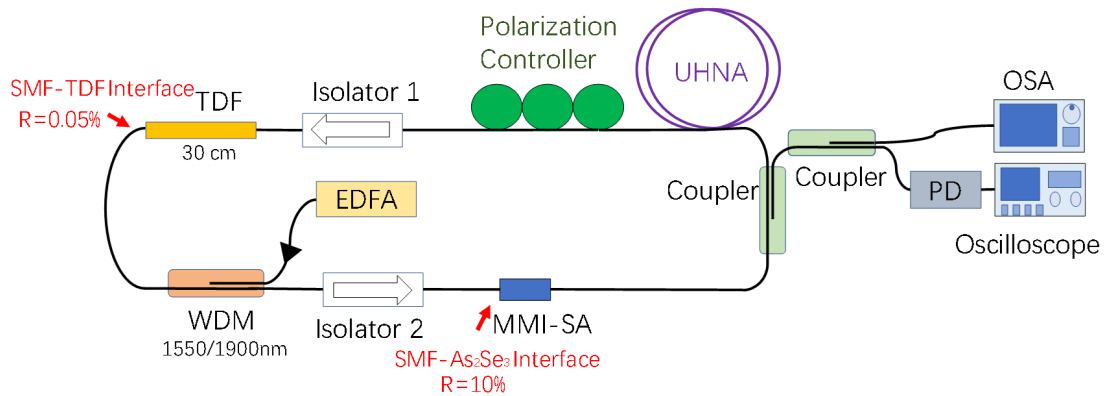


**Fig. 5.5** Schematic of a fiber pulsed laser. EDFA: erbium-doped fiber amplifier. WDM: wavelength division multiplexer. TDF: thulium-doped fiber. UHNA: ultra-high numerical aperture fiber. OSA: optical spectrum analyzer. PD: photodetector. MMI-SA: multimode interference saturable absorber. Arrows point to SMF-TDF interface and SMF-As<sub>2</sub>Se<sub>3</sub> interface, which forming a secondary Fabry-Perot cavity.

with a length of 30 cm is pumped using the amplified spontaneous emission from an erbium-doped fiber amplifier (EDFA) via a 1550/1900 nm wavelength division multiplexer (WDM). Polarization-independent isolators impose an unidirectional light propagation in the ring cavity, where the second isolator between WDM and MMI SA is used to suppress the Fresnel reflection at the SMF-As<sub>2</sub>Se<sub>3</sub> fiber interface. Otherwise, a secondary cavity is constructed by the SMF-TDF interface and SMF-As<sub>2</sub>Se<sub>3</sub> interface which are marked by two red arrows. A polarization controller is used to compensate for the random polarization fluctuation in the cavity, ensuring the stability of this oscillator. Two ultra-high numerical aperture fiber spools (UHNA1 and UHNA7), incorporated with the rest silica SMFs, are used to manage the total cavity dispersion. The UHNA1, UNHA7, and SMF have a dispersion of 40 ps<sup>2</sup>/km, 42 ps<sup>2</sup>/km, and -67 ps<sup>2</sup>/km at a wavelength of 1900 nm, respectively [143, 144]. The fiber length is 4.0 m for the UHNA1 spool and 27.6 m for the UHNA7 spool. The total cavity length is 48.6 m, including a length of 16.7 m for the rest SMFs, leading to a net normal dispersion of 0.23 ps<sup>2</sup>. Taking SA<sub>2</sub> as an example, it is inserted in the ring cavity closely after the TDF for high input power. An 80/20 coupler is used to extract light out of the cavity. The output pulses are characterized by an OSA and a pulse analysis system composed of a photodetector and an oscilloscope. Figure 5.6 shows the impulse response of the pulse analysis system, providing a time response of 0.1 ns in rise time, 2.0 ns in fall time, and 0.1

ns in the deviation of pulse duration, which is observed from the detection of 800 fs optical pulses. An electrical spectrum analyzer is also connected to the photodetector to obtain a radio frequency (RF) spectrum.

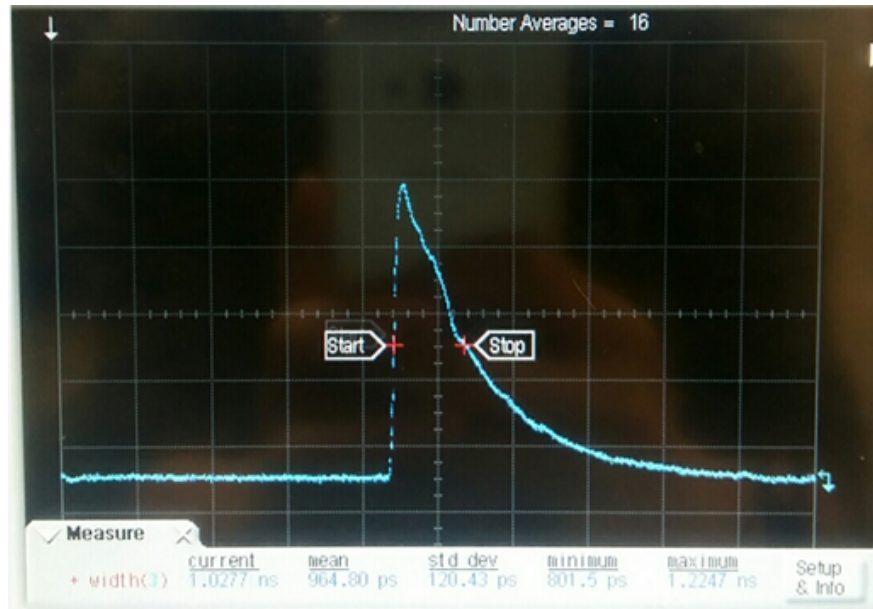


**Fig. 5.6** Impulse response of the photodetector and oscilloscope observed from the detection of 800 fs optical pulses. It has a rise time of 0.1 ns, a fall time of 2.0 ns, a deviation of 0.1 ns.

The fiber laser first enters into a continuous wave regime after increasing the power of EDFA (pump) above  $\sim 0.65$  W. Then, the fiber laser enters into a pulsed regime by simply increasing the pump power above a threshold of 0.70 W. Since the lasing wavelength is determined by the combination of thulium gain spectrum and the transmission spectrum of MMI SA, it is also observed that the pump threshold varies according to the bending state of MMI SA. Property of the MMI SA is optimized by bending MMF to maximize the pulse amplitude. The polarization controller is also adjusted to stabilize the output pulse train and maximize the output power. Figure 5.7a shows the conventional single pulse train at a pump power of 1.0 W. A pulse separation of 235 ns is obtained, matching the total cavity length  $t = nL/c_0$ . Figure 5.7b shows the temporal profile of a single pulse, leading to a pulse duration of 3.1 ns. Such a broad pulse duration is attributed to low input power into the SA, which leading to a small effective modulation depth. Figure 5.7c shows the measured optical spectrum with a peak wavelength at 1876 nm. However, the 3-dB spectral linewidth

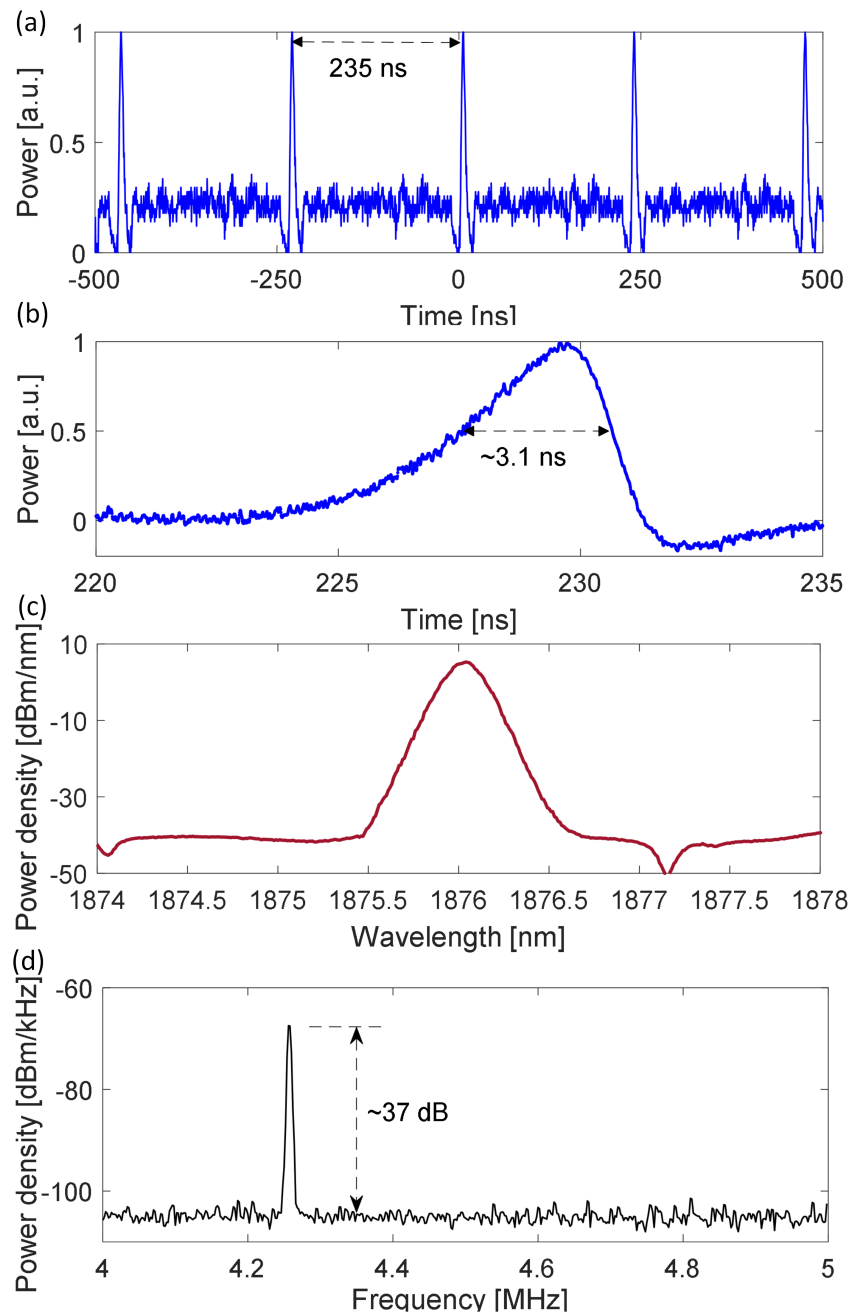


**Fig. 5.7** Experimental results of the fiber pulsed laser when using SA<sub>2</sub>. (a) Pulse train. (b) Detail of a single pulse. (c) Optical spectrum with a resolution of 0.1 nm. (d) Radio frequency spectrum with a resolution of 1 kHz

mostly reflects the instrument response as it is reaching the OSA resolution limit of 0.1 nm. Detailed spectrum of the fiber laser is not resolved whereas it indicates a narrow spectral linewidth. Figure 5.7d shows the RF spectrum of the laser output. A distinct peak at a frequency of 4.26 MHz is obtained with a signal to noise ratio (SNR) of 37 dB, consistent with the pulse separation of 235 ns. The SNR is small compared to other mode-locked lasers whose SNRs are more than 50 dB [128–138], indicating that the fiber cavity is in a weakly mode-locking status, which can be improved by reducing the total cavity insertion loss and increasing the pump power.

The mode-locked fiber laser can also operate with a resembling pulse pattern by removing the second isolator in front of the MMI SA. Compared to the conventional single pulse train pattern, resembling pulses consist of a group of pulses with an identical pulse shape, while the whole pulse packet is propagating at a repetition rate corresponding to the total cavity length [145, 146]. The successive resembling pulse separation is governed by the length of secondary cavity. In this configuration, a secondary Fabry-Perot cavity is constructed by two reflectors, which are the interfaces of SMF-As<sub>2</sub>Se<sub>3</sub> and SMF-TDF with a reflection coefficient of 10% and 0.05%, respectively. Figure 5.8a shows the resembling pulse train pattern, where a dominant pulse separation of 234 ns conforms to the total cavity length of 48.4 m, and a resembling pulse separation of 32 ns is consistent with the fiber length of 3.31 m between two reflectors. Figure 5.8b shows the temporal profile of a single pulse where a pulse duration of 4.4 ns is obtained. Figure 5.8c shows a RF spectrum in a narrow span. A distinct peak at a frequency of 4.27 MHz and a SNR of 40 dB are obtained, in line with the dominant pulse separation of 234 ns. The SNR is increased compared to the conventional single pulse pattern because of the removal of isolator 2 that led to 0.8 dB insertion loss. However, the pulse duration is slightly increased because the current cavity with net normal dispersion is dominated by the balance between gain and cavity loss, where the pulse shortening effect of SA is not prominent. The variation of the pulse shape might not only due to gain depletion effect of thulium-doped fiber where the leading edge of pulse experiences a higher gain, but also come from the increased effective modulation depth of SA, leading to suppression of the low power pulse edge and resulting in a shorter rise time. Figure 5.8d shows a RF spectrum in a wide span, which also agrees with the Fourier transform spectrum of the resembling pulse train pattern. The high peak at a frequency of 31 MHz matches the resembling pulse separation. It is noted that a resembling pulse pattern differs from the Q-switched pulse pattern. The repetition rate is usually at kHz level and varies with pump power for Q-

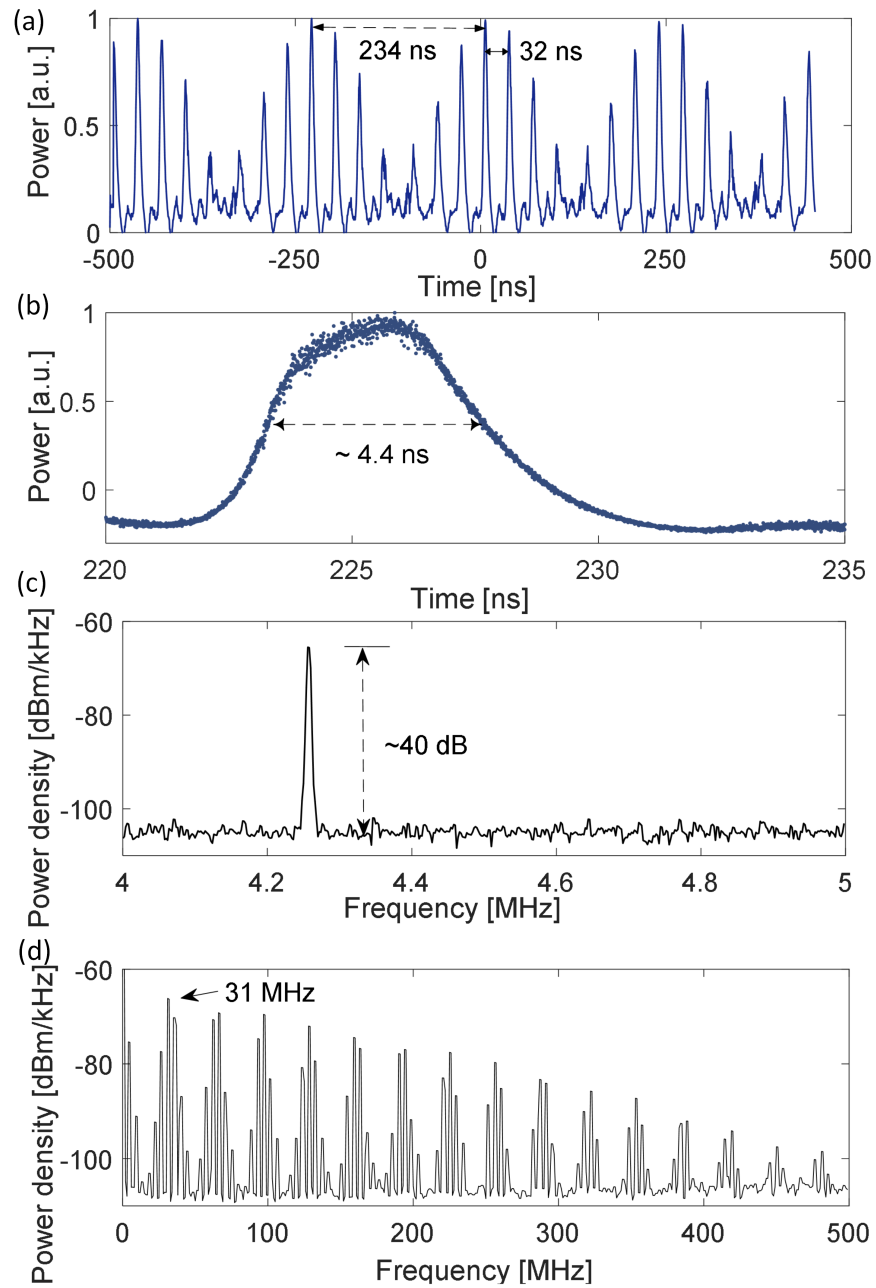


**Fig. 5.8** Experimental results of the fiber pulsed laser when using SA<sub>2</sub> and removing isolator 2. (a) Pulse train. (b) Detail of a single pulse. (c) Radio frequency spectrum in a narrow span with a resolution of 1 kHz and (d) wide span with a resolution of 100 kHz

switched pulse pattern. However, the repetition rate only depends on the total cavity length and keeps stable for resembling pulse pattern.

Figure 5.9 shows the relationship between averaged output power and input pump power of the mode-locked fiber laser with resembling pulses. A pump threshold of 0.65 W is attributed to the total cavity insertion loss of 11.0 dB at the lasing wavelength, including 0.8 dB from isolator, 0.8 dB from WDM, 1.4 dB from the intra-cavity coupler, 5.0 dB from MMI SA, and 3.0 dB from UHNA fibers. A power conversion efficiency is 0.8%, resulting from insufficient utilization of the pump power. The repetition rate of the output pulse train maintains constant and is independent of the pump power, indicating a mode-locking process. When the average output power is 5 mW, the corresponding cavity peak power and peak intensity injected into the MMI SA are 4.75 W and  $1.87 \text{ MW/cm}^2$ , leading to an effective modulation depth of 0.6%. The effective modulation depth is still significantly below the saturation intensity of SA, responsible for a broad pulse duration. The pulse duration would become shorter by reducing the intra-cavity loss and increasing the input power into the SA. Meanwhile, a pump power threshold is also expected to decrease.

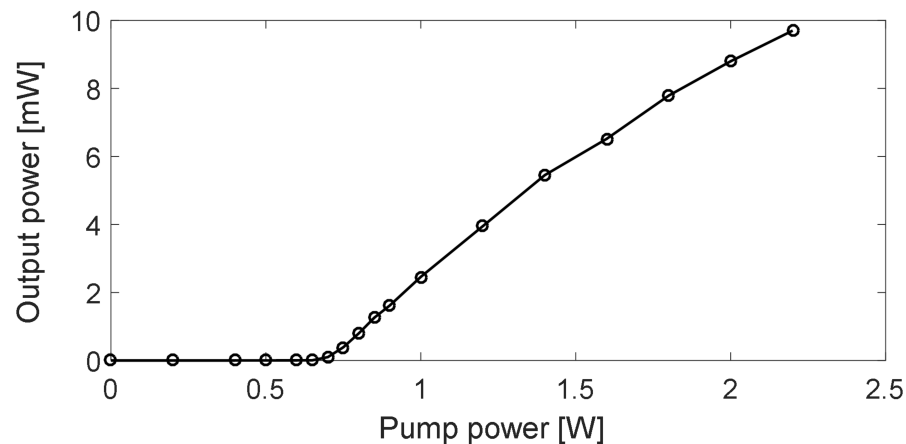


**Fig. 5.9** Relationship between output power and pump power of the fiber pulsed laser.

Figure 5.10a-5.10c show diverse output pulse train patterns with varying fiber lengths in the secondary Fabry-Perot cavity. Comparison among them shows the resembling pulse separation is adjustable by adding different SMF lengths in the Fabry-Perot cavity, leading to a new way to control the pulse pattern. A resembling pulse separation of 34.7 ns, 42.5 ns,

and 82.5 ns are obtained by revising the Fabry-Perot cavity length to 3.59 m, 4.40 m, and 8.53 m, respectively. These consistent results, in turn, confirm the formation of Fabry-Perot cavity arising from Fresnel reflections at the two interfaces. Meanwhile, the dominant pulse separations of 205 ns, 209 ns, and 229 ns are accordant with corresponding total cavity lengths of 42.4 m, 43.2 m, and 47.3 m, respectively. Figure 5.10c shows that resembling pulses from adjacent dominant pulse packets overlap with each other. Therefore, it is possible to construct various pulse patterns via the ratio between total cavity length and secondary cavity length.

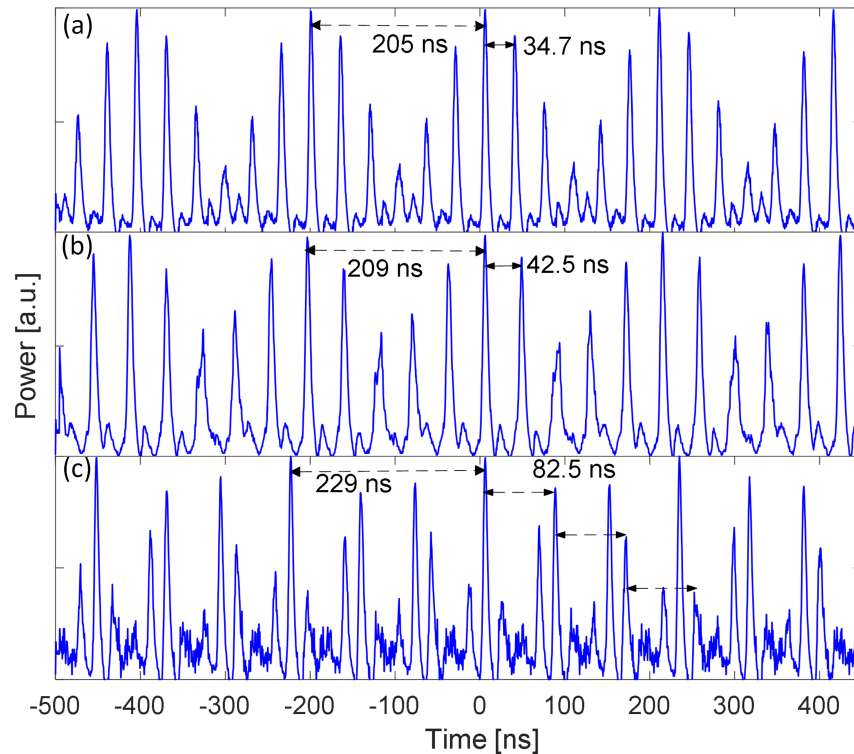


**Fig. 5.10** Output pulse trains of the fiber pulsed laser with (a) a total cavity length of 42.4 m and a Fabry-Perot cavity length of 3.59 m, (b) a total cavity length of 43.2 m and a Fabry-Perot cavity length of 4.40 m, and (c) a total cavity length of 47.3 m and a Fabry-Perot cavity length of 8.53 m.

A wavelength tunable mode-locked laser is demonstrated by bending the MMI structure, which acts as a SA and a bandpass filter simultaneously. Figure 5.11 shows transmission spectra of a tunable mode-locked fiber laser with a resembling pulse pattern. A wavelength

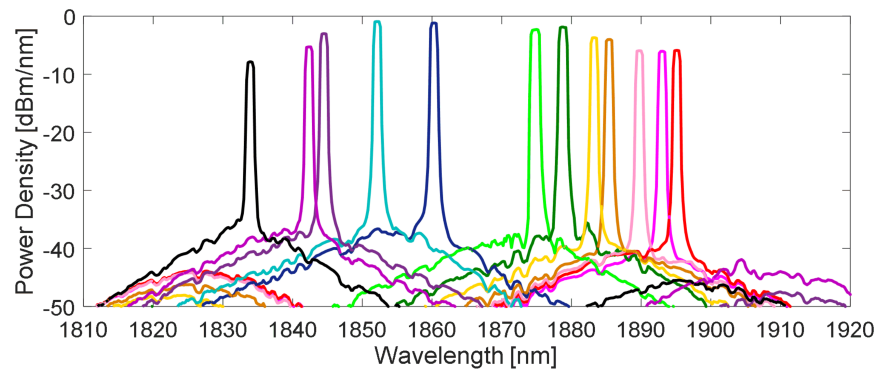


**Fig. 5.11** Spectra of a fiber pulsed laser with a tunability from 1834 nm to 1895 nm.

tunability of 61 nm is obtained, covering 1834 nm-1895 nm. The fiber laser maintains its output pulse train pattern during the wavelength tuning process, where a continuous and broad tuning range is ensured by a few-mode chalcogenide fiber.

Figure 5.12a shows a fiber laser cavity with a total cavity length of 15.2 m and a net cavity dispersion of  $-0.58 \text{ ps}^2$  at the anomalous dispersion region. In this case, a short SA with a length of 14 mm is inserted after the PC and output coupler. Figure 5.12b shows the spectra of Tm-doped fiber spontaneous emission and SA in the linear condition, resulting in dual lasing wavelengths. Figure 5.12c and 5.12d are the output pulse patterns under different polarization states. By optimizing the PC, a good resembling pulse pattern could be obtained, similar to the case at normal dispersion region.

It is noted that the pulse duration is the balanced result of gain, loss, dispersion, nonlinearity, filter, and SA in the laser cavity. Especially in the normal dispersion region, the gain and loss play a more important role. The amplitude and duration of pulse would vary along the cavity, unlike the traditional soliton in the anomalous dispersion region which keeps an unified pulse shape. A simulation of the fiber laser cavity is made following the schematic of figure 5.5. The effects of PC and WDM are ignored. The assumption of SA is idealized using Eq. 5.7. By playing with the gain and loss distribution in the cavity, both broad and narrow pulses are possible to obtain. Though parameters used in simulation are not exactly the same as that in experiment, the tendency of possible pulse shapes are illustrated. Figure 5.13a shows the pulse propagation along the fiber cavity. Figure 5.13b and 5.13c show the pulse in temporal and spectral domain, respectively. In this case, loss of 6 dB is added, and gain saturation energy is set at a level of 3 nJ. A pulse duration of 3.97 ns and an ultra-narrow

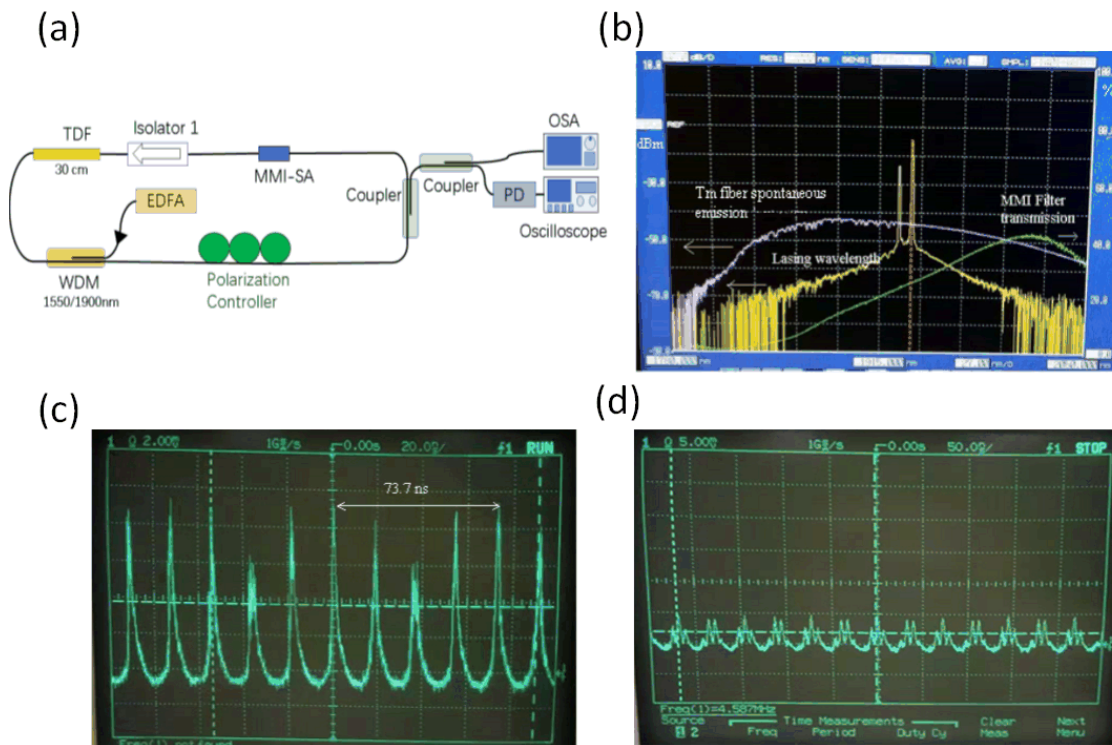


**Fig. 5.12** (a) Setup of a fiber laser with a total cavity length of 15.2 m and a net cavity dispersion of  $-0.58 \text{ ps}^2$ . (b) Spectra of Tm-doped fiber spontaneous emission, SA, and dual lasing wavelengths. (c) and (d) Output resembling pulse patterns under different polarization states.

spectral linewidth of 0.001 nm are obtained. Figure 5.14 shows another case where loss is reduced to 3 dB and gain saturation energy is increased to 10 nJ. A pulse duration of 35.4 ps and a broad spectral linewidth of 10 nm. Thus, a low loss laser cavity with enough gain could improve the performance of the current fiber laser, leading to a better pulse condition.

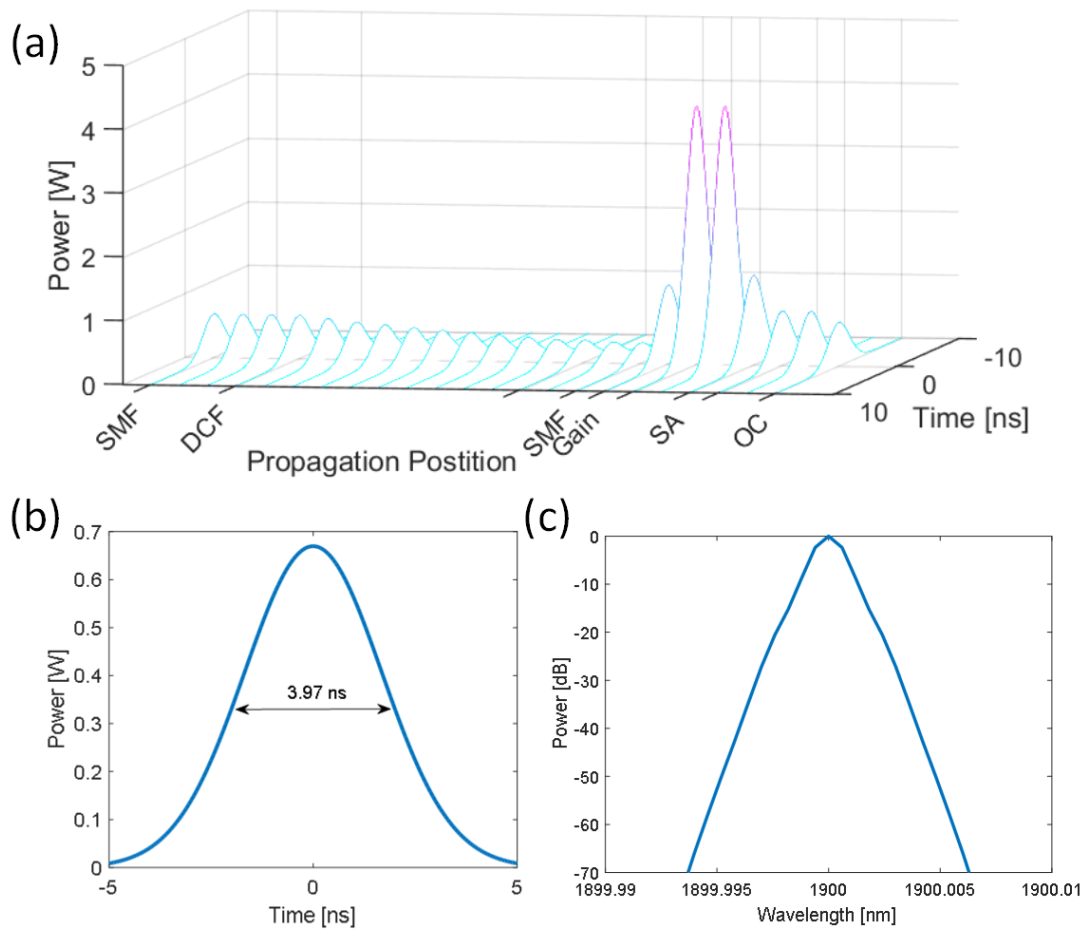


**Fig. 5.13** (a) Pulse propagation along the fiber cavity. (b) Pulse in time domain. (c) Spectrum of the pulse. SMF: single mode fiber. DCF: dispersion compensating fiber. SA: saturable absorber. OC: output coupler. There a 3 dB loss at the chalcogenide fiber and 3 dB loss at the DCF. Gain saturation energy is 3 nJ.

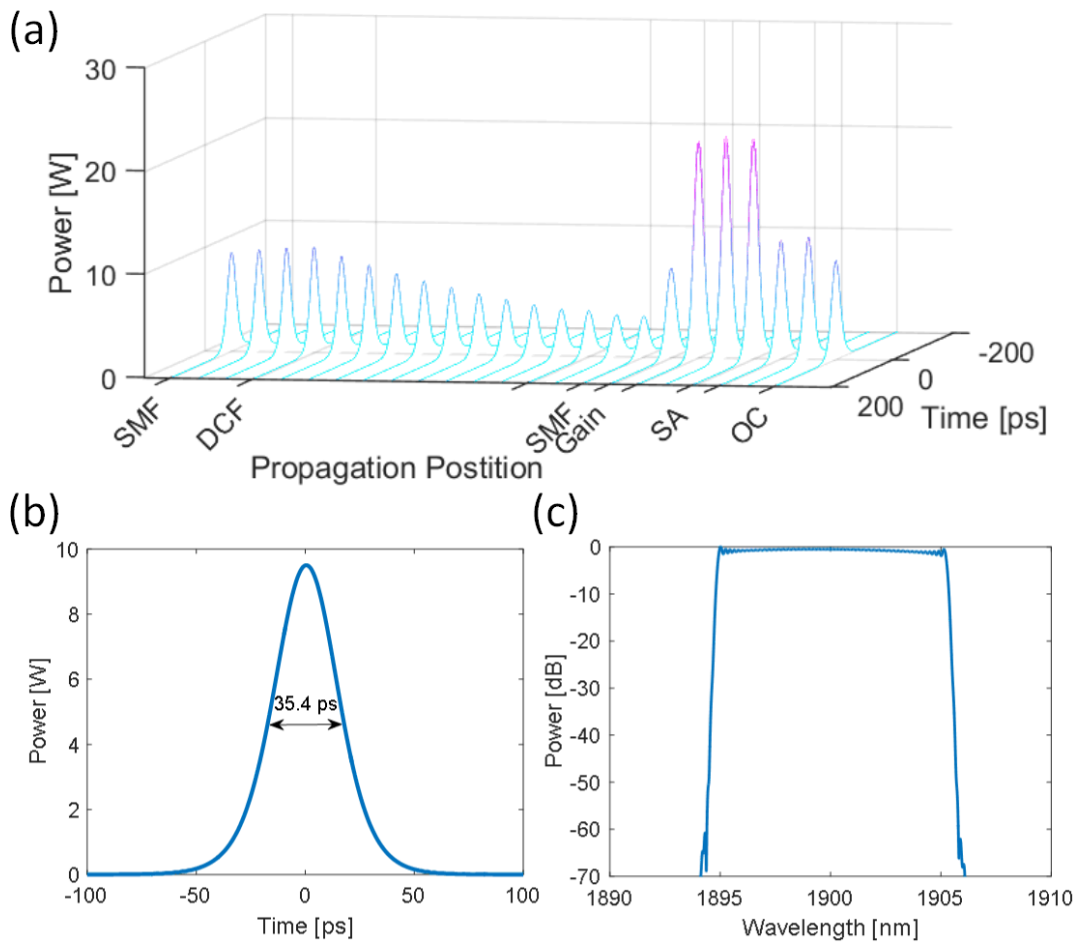


**Fig. 5.14** (a) Pulse propagation along the fiber cavity. (b) Pulse in time domain. (c) Spectrum of the pulse. SMF: single mode fiber. DCF: dispersion compensating fiber. SA: saturable absorber. OC: output coupler. There a 3 dB loss at the DCF. Gain saturation energy is 10 nJ.

## 5.6 Summary

In summary, an all-fiber chalcogenide SA is demonstrated for the first time based on a singlemode-multimode-singlemode fiber structure. Nonlinear multimode interference mechanisms for the saturable absorption effect are summarized. The SA has a modulation depth of 10% and an estimated peak saturation intensity  $<55 \text{ MW/cm}^2$ . Transverse core to core offsets at both input and output SMF-MMF interfaces are introduced to finely adjust linear

transmission properties such as peak wavelength, FSR, extinction ratio, and insertion loss, providing a flexible way in the design. As a result, the length of MMF is no longer crucial. A few-mode chalcogenide MMF is beneficial for a SA as it ensures a broad and continuous tunability after fabrication. Then, a mode-locked fiber laser is passively triggered by inserting this SA into a laser cavity. Both conventional single pulse and resembling pulse patterns are presented and discussed. Diverse output pulse patterns are possible taking advantage of the resembling pulses. Finally, employing the MMI structure as a SA and a tunable band-pass filter simultaneously, the mode-locked fiber laser demonstrates a continuous wavelength tunability of 61 nm, covering 1834 nm to 1895 nm. As a building-block compatible with the mid-infrared spectral range, this chalcogenide fiber SA will create new avenues of research toward mid-infrared fiber pulsed lasers.

# Chapter 6

## Conclusion and outlook

### 6.1 Conclusion

In the scope of this thesis, my achievements and novelties toward tunable bandpass filters in chalcogenide fibers are highlighted, followed by their applications in fiber lasers. The significance of mid-infrared spectral range is identified, boosting the demand for chalcogenide fiber components due to their excellent mid-infrared transparency and high nonlinearity. Along with theoretical analyses of fiber basics, chapter 3 to 5 address the fabrication procedures and experimental characterizations. This thesis fulfills the need of mid-infrared tunable fiber filters as building-block components, paving the way for future integrations and researches.

First, I demonstrate a chalcogenide Fabry-Perot filter with an ultrabroad wavelength tunability  $>300$  nm. Dielectric materials suitable for the mid-infrared spectral range are selected and deposited on the  $\text{As}_2\text{S}_3$  fiber facet via an electron-beam evaporation method, leading to high reflective thin-film coatings consisting of Ge layers and  $\text{CaF}_2$  layers. A theoretical model is established to analyze the additional loss due to surface roughness and diverging Gaussian beam propagation in the Fabry-Perot cavity. As a proof of concept for potential applications, a tunable fiber laser is assembled, resulting in a continuous wave regime with a wavelength tunability from 1835 nm to 1920 nm, limited by the thulium gain bandwidth. This work will further lead to a commercialized mid-infrared tunable fiber filter.

Second, I demonstrate a tunable multimode interference filter based on a few-mode chalcogenide fiber ( $\text{As}_2\text{Se}_3$ ). The filter is assembled by a singlemode-multimode-singlemode fiber structure, where transverse core to core offsets at both input and output interfaces are applied as a new degree of freedom in determining the transmission spectrum. After a

comparison of multimode fibers with various core diameters, guidelines for a broadly tunable filter are summarized, where a continuous wavelength tunability  $>54$  nm and a hop tunability of 84 nm are obtained, surpassing the tunability of same kind of filters. Theoretical analysis is also provided to support the experimental results. This work provides an appealing solution for mid-infrared all-fiber tunable filters with ease of fabrication, low cost, and durability. Further investigation of this multimode interference filter leads to inspirations of several mid-infrared tunable filters and saturable absorbers with a similar structure.

Third, I demonstrate an all-fiber saturable absorber based on nonlinear multimode interference in an  $\text{As}_2\text{Se}_3$  few-mode fiber. Generalized multimode nonlinear Schrödinger equation is introduced to describe the light behavior. Mechanisms responsible for saturable absorption are qualitatively summarized. Compared to similar kinds of saturable absorbers in silica fibers, this work proposes lateral core to core offsets at both input and output SMF-MMF interfaces, overcoming the stringent restriction imposed on the MMF length and providing a new way to customize the property of saturable absorber. A modulation depth of 10% and a peak saturation intensity  $<55$  MW/cm<sup>2</sup> are obtained. This multimode interference saturable absorber acts as a tunable bandpass filter simultaneously by inserting it into a fiber laser cavity. A mode-locked fiber laser is passively triggered into a pulsed regime with a wavelength tunability from 1834 nm to 1895 nm while maintaining the output pulse pattern. In addition to the conventional single pulse pattern, a resembling pulse pattern is obtained, arising from a secondary Fabry-Perot cavity constructed by Fresnel reflectors, while the successive pulse separation is controllable by the length of Fabry-Perot cavity. This work meets the increasing demand toward a mid-infrared pulsed fiber laser and creates a new avenue to generate diverse ultrafast pulse patterns.

Among these fiber components, the fiber Fabry-Perot filter is expensive while the coating fabrication process is also time consuming. It might be difficult to precisely align such two chalcogenide fibers due to high reflection coatings, where a light source at a low reflection wavelength of the coating is recommended as an assist. Since the transmission of Fabry-Perot filter is extremely sensitive to the cavity length, this filter is better packaged to avoid vibration and prevented from air flow. However, the wavelength tunability of Fabry-Perot is inherently broad and the design technique of multilayer high reflection coating is matured. By cleaving the chalcogenide fiber, the surface roughness could be further improved. It is possible to obtain an extremely high finesse and narrow bandwidth using concave fiber facets. The MMI fiber filter is cost effective and easy to fabricate. However, the bandwidth is

broader, and the tuning process is hard to quantify. The interaction among modes, the fiber birefringence, and the angular misalignment would lead to mismatch between the simulation and fabrication. Due to the available equipment in the mid-infrared wavelength range, it is currently difficult to precisely control the peak transmission wavelength without simultaneously observing the transmission spectrum. Similarly, though the chalcogenide fiber SA is compatible to the mid-infrared wavelength range, the lasing wavelength is determined by the gain medium, the SA, and other cavity conditions. The insertion loss of SA should be further decreased by “splicing” technique for chalcogenide fibers. The saturable absorption property at each wavelength should be further explored in regard to the linear transmission spectrum of SA, providing a guideline for designers.

## 6.2 Outlook

Following research avenues piloted by works in this thesis, several potential projects are inspired.

First, performance of a chalcogenide Fabry-Perot filter could be further improved by a concave Fabry-Perot cavity. Loss coming from the diverging Gaussian beam propagation is reduced to a minimum value by appropriate cavity curvatures. In contrast to the case in silica fibers where a concave fiber facet is fabricated by CO<sub>2</sub> laser ablating, the chalcogenide fiber should be ablated through a femtosecond laser. H. Wang *et al.* have demonstrated induced damage on the chalcogenide bulk glass via a femtosecond laser with a wavelength of 800 nm [147]. I have tested this method and proved it is useful for chalcogenide fibers. However, a laser ablation setup should be integrated with a light interferometer to simultaneously measure the facet profile. Power and beam size focus on the fiber facet should also be optimized to get an ideal curvature. Meanwhile, the surface roughness of multilayer thin-film coating could be reduced by an ion-assisted electron-beam evaporation method, leading to a compact microstructure. Then, the concave chalcogenide Fabry-Perot filter can be used commercially in the mid-infrared spectral range.

Second, following the idea of multimode interference, a mid-infrared tunable fiber filter could be fabricated by tapering a singlemode chalcogenide fiber with a nonadiabatic transition region, leading to power coupling to the cladding modes. Then, a bandpass wavelength filter is obtained based on the interference between core and cladding modes. Coupling loss at fiber connections could be avoided in this way.

Third, an all-fiber chalcogenide saturable absorber could be obtained similarly based on the nonlinear multimode interference effect. A nonadiabatically tapered singlemode fiber or an adiabatically tapered multimode fiber could be used to enhance the fiber nonlinearity by reducing the core diameter. Furthermore, a truly mid-infrared laser could be constructed to investigate the diverse pulsed regimes based on the proposed chalcogenide fiber multimode interference saturable absorber.

## References

- [1] H. Venghaus and N. Grote, *Fibre optics communication: key devices*. Springer Science & Business Media, 2nd ed., 2017.
- [2] F. Mitschke, *Fiber optics: physics and technology*. Springer Nature, 2nd ed., 2016.
- [3] S. D. Personick, *Fibre optics: technology and applications*. Springer Science & Business Media, 1st ed., 1985.
- [4] J. Zhao, L. Li, L. Zhao, D. Tang, D. Shen, and L. Su, “Tunable and switchable harmonic h-shaped pulse generation in a 3.03 km ultralong mode-locked thulium-doped fiber laser,” *Photonics Res.*, vol. 7, no. 3, pp. 332–340, 2019.
- [5] V. V. Ter-Mikirtychev, *Foundamentals of fiber lasers and fiber amplifiers*. Springer Nature, 2nd ed., 2019.
- [6] H. Venghaus, *Wavelength filters in fibre optics*. Springer Science & Business Media, 1st ed., 2006.
- [7] J. M. Vaughan, *The Fabry-Perot interferometer: history, theory, practice and applications*. Routledge, 1st ed., 1989.
- [8] J. Geng, Q. Wang, J. Wang, S. Jiang, and K. Hsu, “All-fiber wavelength-swept laser near 2  $\mu\text{m}$ ,” *Opt. Lett.*, vol. 36, no. 19, pp. 3771–3773, 2011.
- [9] R. Kashyap, *Fiber Bragg gratings*. Academic Press, 2nd ed., 2010.
- [10] G. Ramírez-Meléndez, M. Bello-Jiménez, O. Pottiez, and M. V. Andrés, “Improved all-fiber acousto-optic tunable bandpass filter,” *IEEE Photon. Technol. Lett.*, vol. 29, no. 12, pp. 1015–1018, 2017.
- [11] Y. Li, Q. Sun, Z. Xu, Y. Luo, and D. Liu, “A single longitudinal mode fiber ring laser based on cascaded microfiber knots filter,” *IEEE Photon. Technol. Lett.*, vol. 28, no. 20, pp. 2172–2175, 2016.

- [12] D. E. Heard, *Analytical techniques for atmospheric measurement*. Blackwell, 1st ed., 2006.
- [13] B. H. Stuart, *Infrared spectroscopy: fundamentals and applications*. John Wiley & Sons, 1st ed., 2004.
- [14] R. V. Kochanov, I. E. Gordon, L. S. Rothman, P. Wcislo, C. Hill, and J. S. Wilzewski, "HITRAN Application Programming Interface (HAPI): A comprehensive approach to working with spectroscopic data," *J. Quant. Spectrosc. Radiat. Transfer*, vol. 177, pp. 15–30, 2016.
- [15] J. H. Taylor and H. W. Yates, "Atmospheric transmission in the infrared," *J. Opt. Soc. Am.*, vol. 47, no. 3, pp. 223–226, 1957.
- [16] A. K. Majumdar and J. C. Ricklin, *Free-space laser communications: principles and advances*. Springer Science and Business Media, 1st ed., 2008.
- [17] J. M. Theriault and J. O. Jensen, *Spectral sensing research for surface and air monitoring in chemical, biological and radiological defense and security applications*. World Scientific, 1st ed., 2009.
- [18] M. Xie, S. Dai, C. You, P. Zhang, C. Yang, W. Wei, G. Li, and R. Wang, "Correlation among structure, water peak absorption, and femtosecond laser ablation properties of Ge–Sb–Se chalcogenide glasses," *J. Phys. Chem. C*, vol. 122, no. 3, pp. 1681–1687, 2018.
- [19] M. A. Mackanos, D. M. Simanovskii, K. E. Schriver, M. S. Hutson, C. H. Contag, J. A. Kozub, and E. D. Jansen, "Pulse-duration-dependent mid-infrared laser ablation for biological applications," *IEEE J. Sel. Top. Quantum Electron.*, vol. 18, no. 4, pp. 1514–1522, 2012.
- [20] I. T. Sorokina and K. L. Vodopyanov, *Mid-IR laser applications in medicine*. Springer, 1st ed., 2003.
- [21] Y. Wu, M. Meneghetti, J. Troles, and J. L. Adam, "Chalcogenide microstructured optical fibers for mid-infrared supercontinuum generation: interest, fabrication, and applications," *Appl. Sci.*, vol. 8, no. 9, p. 1637, 2018.
- [22] B. Karasu, T. İDİNAK, E. Erkol, and A. O. Yanar, "Chalcogenide glasses," *El-Cezeri Journal of Science and Engineering*, vol. 6, no. 3, pp. 428–457, 2019.
- [23] R. Frerichs, "New optical glasses with good transparency in the infrared," *J. Opt. Soc. Am.*, vol. 43, no. 12, pp. 1153–1157, 1953.

- [24] T. Miyashita and Y. Terunuma, "Optical transmission loss of As-S glass fiber in 1.0-5.5  $\mu\text{m}$  wavelength range," *Jpn. J. Appl. Phys.*, vol. 21, no. 2, pp. 175–176, 1982.
- [25] B. J. E. adn B. L. Davies and K. Richardson, "Chalcogenide photonics," *Nat. Photonics*, vol. 5, pp. 141–148, 2011.
- [26] L. Calvez, "Chalcogenide glasses and glass-ceramics: transparent materials in the infrared for dual applications," *C. R. Physique*, vol. 18, no. 5-6, pp. 314–322, 2017.
- [27] F. Vanier, F. Côté, M. E. Amraoui, Y. Messaddeq, Y.-A. Peter, and M. Rochette, "Low-threshold lasing at 1975 nm in thulium-doped tellurite glass microspheres," *Opt. Lett.*, vol. 40, no. 22, pp. 5227–5230, 2015.
- [28] Y. Shpotyuk, C. Boussard-Pledel, V. Nazabal, R. Chahal, J. Ari, B. Pavlyk, J. Cebulski, J. Doualan, and B. Bureau, "Ga-modified  $\text{As}_2\text{Se}_3$ -Te glasses for active applications in IR photonics," *Opt. Mater.*, vol. 46, pp. 228–232, 2015.
- [29] J. S. Sanghera, L. Brandon Shaw, and I. D. Aggarwal, "Chalcogenide glass-fiber-based mid-ir sources and applications," *IEEE J. Sel. Top. Quantum Electron.*, vol. 15, no. 1, pp. 114–119, 2009.
- [30] J. S. Sanghera, C. M. Florea, L. Shaw, P. Pureza, V. Q. Nguyen, M. Bashkansky, Z. Dutton, and I. D. Aggarwal, "Non-linear properties of chalcogenide glasses and fibers," *J. Non-Cryst. Solids*, vol. 354, no. 2-9, pp. 462–467, 2008.
- [31] N. Abdukerim, I. Alamgir, and M. Rochette, "All-fiber frequency-resolved optical gating pulse characterization from chalcogenide glass," *Opt. Lett.*, vol. 43, no. 14, pp. 3228–3231, 2018.
- [32] N. Abdukerim, I. Alamgir, and M. Rochette, "Pulse characterization by cross-phase modulation in chalcogenide glass," *Opt. Lett.*, vol. 43, no. 19, pp. 4771–4774, 2018.
- [33] N. Abdukerim, L. Li, M. E. Amraoui, Y. Messaddeq, and M. Rochette, "2  $\mu\text{m}$  Raman fiber laser based on a multimaterial chalcogenide microwire," *Appl. Phys. Lett.*, vol. 110, p. 161103, 2017.
- [34] R. Ahmad and M. Rochette, "All-chalcogenide Raman-parametric laser, wavelength converter, and amplifier in a single microwire," *IEEE J. Sel. Top. Quantum Electron.*, vol. 20, no. 5, pp. 299–304, 2014.
- [35] T. North and M. Rochette, "Raman-induced noiselike pulses in a highly nonlinear and dispersive all-fiber ring laser," *Opt. Lett.*, vol. 38, no. 6, pp. 890–892, 2013.
- [36] R. Ahmad and M. Rochette, "Raman lasing in a chalcogenide microwire-based Fabry–Perot cavity," *Opt. Lett.*, vol. 37, no. 21, pp. 4549–4551, 2012.

- [37] R. Ahmad and M. Rochette, "Chalcogenide microwire based Raman laser," *Appl. Phys. Lett.*, vol. 101, no. 101110, 2012.
- [38] F. Vanier, M. Rochette, N. Godbout, and Y.-A. Peter, "Raman lasing in As<sub>2</sub>S<sub>3</sub> high-Q whispering gallery mode resonators," *Opt. Lett.*, vol. 38, no. 23, pp. 4966–4969, 2013.
- [39] F. Vanier, Y.-A. Peter, and M. Rochette, "Cascaded Raman lasing in packaged high quality As<sub>2</sub>S<sub>3</sub> microspheres," *Opt. Express*, vol. 22, no. 23, pp. 28731–28739, 2014.
- [40] N. Abdukerim, L. Li, and M. Rochette, "Chalcogenide-based optical parametric oscillator at 2  $\mu\text{m}$ ," *Opt. Lett.*, vol. 41, no. 18, pp. 4364–4367, 2016.
- [41] R. Ahmad and M. Rochette, "High efficiency and ultra broadband optical parametric four-wave mixing in chalcogenide-PMMA hybrid microwires," *Opt. Express*, vol. 20, no. 9, pp. 9572–9580, 2012.
- [42] R. Ahmad and M. Rochette, "Chalcogenide optical parametric oscillator," *Opt. Express*, vol. 20, no. 9, pp. 10095–10099, 2012.
- [43] R. Ahmad and M. Rochette, "High efficiency and ultra broadband optical parametric four-wave mixing in chalcogenide-PMMA hybrid microwires," *Opt. Express*, vol. 20, no. 9, pp. 9572–9580, 2012.
- [44] A. Al-Kadry, C. Baker, M. E. Amraoui, Y. Messaddeq, and M. Rochette, "Broadband supercontinuum generation in As<sub>2</sub>Se<sub>3</sub> chalcogenide wires by avoiding the two-photon absorption," *Opt. Lett.*, vol. 38, no. 7, pp. 1185–1187, 2013.
- [45] S. Venck, F. St-Hilaire, L. Brilland, A. N. Ghosh, R. Chahal, C. Caillaud, M. Meneghetti, J. Troles, F. Joulain, S. Cozic, S. Poulain, G. Huss, M. Rochette, J. M. Dudley, and T. Sylvestre, "2-10  $\mu\text{m}$  Mid-infrared fiber-based supercontinuum laser source: experiment and simulation," *Laser Photonics Rev.*, vol. 14, no. 6, p. 2000011, 2020.
- [46] D. D. Hudson, S. Antipov, L. Li, I. Alamgir, T. Hu, M. E. Amraoui, Y. Messaddeq, M. Rochette, S. D. Jackson, and A. Fuerbach, "Toward all-fiber supercontinuum spanning the mid-infrared," *Optica*, vol. 4, no. 10, pp. 1163–1166, 2017.
- [47] A. Al-Kadry, M. E. Amraoui, Y. Messaddeq, and M. Rochette, "Two octaves mid-infrared supercontinuum generation in As<sub>2</sub>Se<sub>3</sub> microwires," *Opt. Express*, vol. 22, no. 25, pp. 31131–31137, 2014.
- [48] A. Al-Kadry and M. Rochette, "Maximized soliton self-frequency shift in non-uniform microwires by the control of third-order dispersion perturbation," *J. Light. Technol.*, vol. 31, no. 9, pp. 1462–1467, 2013.

- [49] I. Alamgir, F. St-Hilaire, and M. Rochette, “All-fiber nonlinear optical wavelength conversion system from the C-band to the mid-infrared,” *Opt. Lett.*, vol. 45, no. 4, pp. 857–860, 2020.
- [50] M. Rochette, “Design and fabrication of nonlinear optical waveguides for far-detuned wavelength conversion to the mid-infrared,” *Adv. Opt. Technol.*, vol. 7, no. 5, pp. 321–326, 2018.
- [51] L. Li, N. Abdukerim, and M. Rochette, “Mid-infrared wavelength conversion from  $\text{As}_2\text{Se}_3$  microwires,” *Opt. Lett.*, vol. 42, no. 3, pp. 639–642, 2017.
- [52] A. Dot, E. Meyer-Scott, R. Ahmad, M. Rochette, and T. Jennewein, “Converting one photon into two via four-wave mixing in optical fibers,” *Phys. Rev. A*, vol. 90, p. 043808, 2014.
- [53] T. Godin, Y. Combes, R. Ahmad, M. Rochette, T. Sylvestre, and J. M. Dudley, “Far-detuned mid-infrared frequency conversion via normal dispersion modulation instability in chalcogenide microwires,” *Opt. Lett.*, vol. 39, no. 7, pp. 1885–1888, 2014.
- [54] A. Al-Kadry and M. Rochette, “Mid-infrared sources based on the soliton self-frequency shift,” *J. Opt. Soc. Am. B*, vol. 29, no. 6, pp. 1347–1355, 2012.
- [55] I. D. Aggarwal and J. S. Sanghera, “Development and applications of chalcogenide glass optical fibers at NRL,” *J. Optoelectron. Adv. Mater.*, vol. 4, no. 3, pp. 665–678, 2002.
- [56] J. D. Musgraves, J. Hu, and L. Calvez, *Springer handbook of glass*. Springer Nature, 1st ed., 2019.
- [57] M. Rezaei and M. Rochette, “All-chalcogenide single-mode optical fiber couplers,” *Opt. Lett.*, vol. 44, no. 21, pp. 5266–5269, 2019.
- [58] F. Tavakoli, A. Rekik, and M. Rochette, “Broadband and wavelength-dependent chalcogenide optical fiber couplers,” *IEEE Photon. Technol. Lett.*, vol. 29, no. 9, pp. 735–738, 2017.
- [59] L. Li, N. Abdukerim, and M. Rochette, “Chalcogenide optical microwires cladded with fluorine-based CYTOP,” *Opt. Express*, vol. 24, no. 17, pp. 18931–18937, 2016.
- [60] C. Baker and M. Rochette, “Birefringence engineering and high nonlinearity in eccentric-core  $\text{As}_2\text{Se}_3$ -PMMA microtapers,” *J. Light. Technol.*, vol. 31, no. 1, pp. 171–176, 2013.
- [61] C. Baker and M. Rochette, “High nonlinearity and single-mode transmission in tapered multimode  $\text{As}_2\text{Se}_3$ -PMMA fibers,” *IEEE Photonics J.*, vol. 4, no. 3, pp. 960–969, 2012.

- [62] C. Baker and M. Rochette, “Highly nonlinear hybrid AsSe-PMMA microtapers,” *Opt. Express*, vol. 18, no. 12, pp. 12391–12398, 2010.
- [63] R. Ahmad, M. Rochette, and C. Baker, “Fabrication of Bragg gratings in subwavelength diameter As<sub>2</sub>Se<sub>3</sub> chalcogenide wires,” *Opt. Lett.*, vol. 36, no. 15, pp. 2886–2888, 2011.
- [64] I. C. M. Litter, L. B. Fu, E. C. Mägi, D. Pudo, and B. J. Eggleton, “Widely tunable, acousto-optic resonances in chalcogenide As<sub>2</sub>Se<sub>3</sub> fiber,” *Opt. Express*, vol. 14, no. 18, pp. 8088–8095, 2006.
- [65] R. Ahmad and M. Rochette, “Photosensitivity at 1550 nm and Bragg grating inscription in As<sub>2</sub>Se<sub>3</sub> chalcogenide microwires,” *Appl. Phys. Lett.*, vol. 99, p. 061109, 2011.
- [66] M. R. Majewski, R. I. Woodward, and S. D. Jackson, “Dysprosium-doped ZBLAN fiber laser tunable from 2.8  $\mu\text{m}$  to 3.4  $\mu\text{m}$ , pumped at 1.7  $\mu\text{m}$ ,” *Opt. Lett.*, vol. 43, no. 5, pp. 971–974, 2018.
- [67] H. Mao, D. K. Tripathi, Y. Ren, K. K. M. B. D. Silva, M. Martyniuk, J. Antoszewski, J. Bumgarner, J. M. Dell, and L. Faraone, “Large-area MEMS tunable Fabry–Perot filters for multi/hyperspectral infrared imaging,” *IEEE J. Sel. Top. Quantum Electron.*, vol. 23, no. 2, pp. 45–52, 2017.
- [68] Amorphous Materials Inc. <http://www.amorphousmaterials.com/products/>. Accessed May 7, 2020.
- [69] G. P. Agrawal, *Nonlinear fiber optics*. Academic Press, 5th ed., 2013.
- [70] M. Born and E. Wolf, *Principles of optics: electromagnetic theory of propagation, interference and diffraction of light*. Pergamon Press, 4th ed., 1970.
- [71] K. Okamoto, *Fundamentals of optical waveguides*. Academic Press, 2nd ed., 2006.
- [72] H. A. Macleod, *Thin-film optical filters*. CRC Press, 4th ed., 2010.
- [73] N. Kaiser and H. K. Pulker, *Optical interference coatings*. Springer Nature, 1st ed., 2003.
- [74] C. K. Carniglia and D. Jensen, “Single-layer model for surface roughness,” *Appl. Opt.*, vol. 41, no. 16, pp. 3167–3171, 2002.
- [75] A. F. Turner and P. W. Baumeister, “Multilayer mirrors with high reflectance over an extended spectral region,” *Appl. Opt.*, vol. 5, no. 1, pp. 69–76, 1966.

- [76] S. Pevec and D. Donlagic, "Miniature all-fiber Fabry–Perot sensor for simultaneous measurement of pressure and temperature," *Appl. Opt.*, vol. 51, no. 19, pp. 4536–4541, 2012.
- [77] A. M. Shrivastav, D. S. Gunawardena, Z. Liu, and H. Y. Tam, "Microstructured optical fiber based Fabry–Pérot interferometer as a humidity sensor utilizing chitosan polymeric matrix for breath monitoring," *Sci. Rep.*, vol. 10, no. 6002, 2020.
- [78] Y. Liu, D. N. Wang, and W. P. Chen, "Crescent shaped Fabry-Perot fiber cavity for ultra-sensitive strain measurement," *Sci. Rep.*, vol. 6, no. 38390, 2016.
- [79] Y. J. Rao, Z. L. Ran, and Y. Gong, *Fiber-optics Fabry-Perot sensors: an introduction*. CRC Press, 1st ed., 2017.
- [80] D. Hunger, T. Steinmetz, Y. Colombe, C. Deutsch, T. W. Hänsch, and J. Reichel, "A fiber Fabry–Perot cavity with high finesse," *New J. Phys.*, vol. 12, no. 065038, 2010.
- [81] C. Lee, W. Hong, H. Hsieh, and Z. Weng, "Air gap fiber Fabry–Pérot interferometer for highly sensitive micro-airflow sensing," *IEEE Photon. Technol. Lett.*, vol. 23, no. 13, pp. 905–907, 2011.
- [82] Y. Jiang and C. Tang, "High-finesse micro-lens fiber-optic extrinsic Fabry–Perot interferometric sensors," *Smart Mater. Struct.*, vol. 17, no. 055013, 2008.
- [83] G. K. Gulati, H. Takahashi, N. Podoliak, P. Horak, and M. Keller, "Fiber cavities with integrated mode matching optics," *Sci. Rep.*, vol. 7, no. 5556, 2017.
- [84] R. St-Gelais, A. Poulin, and Y. Peter, "Advances in modeling, design, and fabrication of deep-etched multilayer resonators," *J. Light. Technol.*, vol. 30, no. 12, pp. 1900–1908, 2012.
- [85] P. Klocek, *Handbook of infrared optical materials*. CRC Press, 1st ed., 1991.
- [86] K. Seshan, *Handbook of thin film deposition: process and technologies*. Noyes Publications, 2nd ed., 2002.
- [87] I. Petrov, P. B. Barna, L. Hultman, and J. E. Greene, "Microstructural evolution during film growth," *J. Vac. Sci. Technol.*, vol. 21, no. S117, 2003.
- [88] G. N. Strauss, *Mechanical stress in optical coatings*. Springer, 1st ed., 2003.
- [89] R. Koch, "Stress in evaporated and sputtered thin films – a comparison," *Surf. Coat. Technol.*, vol. 204, no. 12-13, pp. 1973–1982, 2010.

- [90] M. Muallem, A. Palatnik, G. D. Nessim, and Y. R. Tischler, “Room temperature fabrication of dielectric Bragg reflectors composed of a  $\text{CaF}_2/\text{ZnS}$  multilayered coating,” *ACS Appl. Mater. Interfaces*, vol. 7, no. 1, pp. 474–481, 2014.
- [91] O. S. Heavens and S. D. Smith, “Dielectric thin films,” *J. Opt. Soc. Am.*, vol. 47, no. 6, pp. 469–472, 1957.
- [92] N. Li, L. H. Cui, J. X. Liu, Z. X. Jia, Z. Kang, Z. W. Dai, F. Zhu, K. Huang, F. Wang, G. S. Qin, and W. P. Qin, “Tunable dual-wavelength  $\text{Er}^{3+}$ -doped fibre laser based on a single multimode interference filter,” *Laser Phys.*, vol. 28, no. 125108, 2018.
- [93] Q. Wu, Y. Semenova, P. Wang, A. M. Hatta, and G. Farrell, “Experimental demonstration of a simple displacement sensor based on a bent single-mode–multimode–single-mode fiber structure,” *Meas. Sci. Technol.*, vol. 22, no. 025203, 2011.
- [94] Q. Wu, A. M. Hatta, P. Wang, Y. Semenova, and G. Farrell, “Use of a bent single SMS fiber structure for simultaneous measurement of displacement and temperature sensing,” *IEEE Photon. Technol. Lett.*, vol. 23, no. 2, pp. 130–132, 2011.
- [95] Y. Zhao, X. Li, and L. Cai, “A highly sensitive Mach–Zehnder interferometric refractive index sensor based on core-offset single mode fiber,” *Sens. Actuator A Phys.*, vol. 233, no. 1, pp. 119–124, 2015.
- [96] A. Khattak, G. Tatel, and L. Wei, “Tunable and switchable erbium-doped fiber laser using a multimode-fiber based filter,” *Appl. Sci.*, vol. 8, no. 7, p. 1135, 2018.
- [97] T. Walbaum and C. Fallnich, “Wavelength tuning of multimode interference bandpass filters by mechanical bending: experiment and theory in comparison,” *Appl. Phys. B*, vol. 108, pp. 117–124, 2012.
- [98] J. E. Antonio-Lopez, A. Castillo-Guzman, D. A. May-Arrijoja, R. Selvas-Aguilar, and P. LiKamWa, “Tunable multimode-interference bandpass fiber filter,” *Opt. Lett.*, vol. 35, no. 3, pp. 324–326, 2010.
- [99] X. Ma, D. Chen, Q. Shi, G. Feng, and J. Yang, “Widely tunable thulium-doped fiber laser based on multimode interference with a large no-core fiber,” *J. Light. Technol.*, vol. 32, no. 19, pp. 3234–3238, 2014.
- [100] M. A. Fuentes-Fuentes, D. A. May-Arrijoja, J. R. Guzman-Sepulveda, M. Torres-Cisneros, and J. J. Sánchez-Mondragón, “Highly sensitive liquid core temperature sensor based on multimode interference effects,” *Sensors*, vol. 15, no. 10, pp. 26929–26939, 2015.

- 
- [101] P. Wang, G. Brambilla, M. Ding, X. Zhang, Y. Semenova, Q. Wu, and G. Farrell, “An SMS fiber structure based on chalcogenide multimode fiber,” *Proc. SPIE, Nonlinear Optics and Applications*, vol. VI, no. 84340N, pp. 3234–3238, 2012.
- [102] L. She, P. Wang, W. Sun, X. Wang, W. Yang, G. Brambilla, and G. Farrell, “A chalcogenide multimode interferometric temperature sensor operating at a wavelength of 2  $\mu\text{m}$ ,” *IEEE Sens. J.*, vol. 17, no. 6, pp. 1721–1726, 2017.
- [103] L. B. Soldano and E. C. M. Pennings, “Optical multi-mode interference devices based on self-imaging: principles and applications,” *J. Light. Technol.*, vol. 13, no. 4, pp. 615–627, 1995.
- [104] X. Zhu, A. Schülzgen, H. Li, L. Li, L. Han, J. V. Moloney, and N. Peyghambarian, “Detailed investigation of self-imaging in largecore multimode optical fibers for application in fiber lasers and amplifiers,” *Opt. Express*, vol. 16, no. 21, pp. 16632–16645, 2008.
- [105] Q. Wang, G. Farrell, and W. Yan, “Investigation on single-mode–multimode–single-mode fiber structure,” *J. Light. Technol.*, vol. 26, no. 5, pp. 512–519, 2008.
- [106] W. S. Mohammed, A. Mehta, and E. G. Johnson, “Wavelength tunable fiber lens based on multimode interference,” *J. Light. Technol.*, vol. 22, no. 2, pp. 469–477, 2004.
- [107] Y. Zhou, S. Lou, Z. Tang, T. Zhao, and W. Zhang, “Tunable and switchable C-band and L-band multi-wavelength erbium-doped fiber laser employing a large-core fiber filter,” *Opt. Laser Technol.*, vol. 111, pp. 262–270, 2019.
- [108] R. T. Schermer and J. H. Cole, “Improved bend loss formula verified for optical fiber by simulation and experiment,” *IEEE J. Quantum Electron.*, vol. 43, no. 10, pp. 899–909, 2007.
- [109] C. Schulze, A. Lorenz, D. Flamm, A. Hartung, S. Schröter, H. Bartelt, and M. Duparré, “Mode resolved bend loss in few-mode optical fibers,” *Opt. Express*, vol. 21, no. 3, pp. 3170–3181, 2013.
- [110] L. Li, A. Al-Kadry, N. Abdukerim, and M. Rochette, “Design, fabrication and characterization of PC, COP and PMMA-cladded  $\text{As}_2\text{Se}_3$  microwires,” *Opt. Mater. Express*, vol. 6, no. 3, pp. 912–921, 2016.
- [111] G. Zhang, R. Stoian, W. Zhao, and G. Cheng, “Femtosecond laser bessel beam welding of transparent to non-transparent materials with large focal-position tolerant zone,” *Opt. Express*, vol. 26, no. 2, pp. 917–926, 2018.
- [112] Y. Jiang, S. Karpf, and B. Jalali, “Time-stretch LiDAR as a spectrally scanned time-of-flight ranging camera,” *Nat. Photonics*, vol. 14, pp. 14–18, 2020.

- [113] E. Weiss, D. Bykhovsky, and S. Arnon, “Symbol error rate model for communication using femtosecond pulses for space applications,” *IEEE Photon. Technol. Lett.*, vol. 28, no. 12, pp. 1286–1289, 2016.
- [114] N. Picqué and T. W. Hänsch, “Frequency comb spectroscopy,” *Nat. Photonics*, vol. 13, pp. 146–157, 2019.
- [115] I. Alamgir, N. Abdukerim, and M. Rochette, “*In situ* fabrication of far-detuned optical fiber wavelength converters,” *Opt. Lett.*, vol. 44, no. 18, pp. 4467–4470, 2019.
- [116] A. Al-Kadry, L. Li, M. E. Amraoui, T. North, Y. Messaddeq, and M. Rochette, “Broadband supercontinuum generation in all-normal dispersion chalcogenide microwires,” *Opt. Lett.*, vol. 40, no. 20, pp. 4687–4690, 2015.
- [117] Y. Liu, A. J. S. Ji, T. Tan, M. Fuest, and J. S. Mehta, “Femtosecond laser-assisted preparation of conjunctival autograft for pterygium surgery,” *Sci. Rep.*, vol. 10, no. 2674, 2020.
- [118] V. Aleksandrov, A. Gluth, V. Petrov, I. Buchvarov, G. Steinmeyer, J. Paaajaste, S. Suomalainen, A. Härkönen, M. Guina, X. Mateos, F. Díaz, and U. Griebner, “Mode-locked Tm,Ho:KLu(WO<sub>4</sub>)<sub>2</sub> laser at 2060 nm using InGaSb-based SESAMs,” *Opt. Express*, vol. 23, no. 4, pp. 4614–4619, 2015.
- [119] C. Wei, Y. Lyu, H. Shi, Z. Kang, H. Zhang, G. Qin, and Y. Liu, “Mid-infrared Q-switched and mode-locked fiber lasers at 2.87 μm based on carbon nanotube,” *IEEE J. Sel. Top. Quantum Electron.*, vol. 25, no. 4, pp. 1–6, 2019.
- [120] G. Zhu, X. Zhu, F. Wang, S. Xu, Y. Li, X. Guo, K. Balakrishnan, R. A. Norwood, and N. Peyghambarian, “Graphene mode-locked fiber laser at 2.8 μm,” *IEEE Photon. Technol. Lett.*, vol. 28, no. 1, pp. 7–10, 2016.
- [121] K. Wang, B. M. Szydłowska, G. Wang, X. Zhang, J. J. Wang, J. J. Magan, L. Zhang, J. N. Coleman, J. Wang, and W. J. Blau, “Ultrafast nonlinear excitation dynamics of black phosphorus nanosheets from visible to mid-infrared,” *ACS Nano*, vol. 10, no. 7, pp. 6923–6932, 2016.
- [122] A. Al-Kadry, M. E. Amraoui, Y. Messaddeq, and M. Rochette, “Mode-locked fiber laser based on chalcogenide microwires,” *Opt. Lett.*, vol. 40, no. 18, pp. 4309–4312, 2015.
- [123] J. Li, Z. Zhang, Z. Sun, H. Luo, Y. Liu, Z. Yan, C. Mou, L. Zhang, and S. K. Turitsyn, “All-fiber passively mode-locked Tm-doped NOLM-based oscillator operating at 2 μm in both soliton and noisy-pulse regimes,” *Opt. Express*, vol. 22, no. 7, pp. 7875–7882, 2014.

- [124] J. Proctor and J. N. Kutz, “Nonlinear mode-coupling for passive mode-locking: application of waveguide arrays, dual-core fibers, and/or fiber arrays,” *Opt. Express*, vol. 13, no. 22, pp. 8933–8950, 2005.
- [125] J. Lee, S. Kwon, and J. H. Lee, “Numerical investigation of the impact of the saturable absorber recovery time on the mode-locking performance of fiber lasers,” *J. Light. Technol.*, vol. 38, no. 15, pp. 4124–4132, 2020.
- [126] F. X. Kurtner, J. A. der Au, and U. Keller, “Mode-locking with slow and fast saturable absorbers-what’s the difference?,” *IEEE J. Sel. Top. Quantum Electron.*, vol. 4, no. 2, pp. 159–168, 1998.
- [127] E. Nazemosadat and A. Mafi, “Nonlinear multimodal interference and saturable absorption using a short graded-index multimode optical fiber,” *J. Opt. Soc. Am. B*, vol. 30, no. 5, pp. 1357–1367, 2013.
- [128] J. Chen, Z. Wang, L. Li, D. N. Wang, T. Zhu, F. Gao, S. Cao, and Z. Fang, “GIMF-based SA for generation of high pulse energy ultrafast solitons in a mode-locked linear-cavity fiber laser,” *J. Light. Technol.*, vol. 38, no. 6, pp. 1480–1485, 2020.
- [129] H. Jiang, H. Li, F. Hu, X. Ren, C. Li, and S. Xu, “Mode-locked Tm fiber laser with a tapered GIMF SA based on nonlinear multimode interference effect,” *IEEE Photon. Technol. Lett.*, vol. 33, no. 9, pp. 503–506, 2020.
- [130] T. Chen, Q. Zhang, Y. Zhang, X. Li, H. Zhang, and W. Xia, “All-fiber passively mode-locked laser using nonlinear multimode interference of step-index multimode fiber,” *Photonics Res.*, vol. 6, no. 11, pp. 1033–1039, 2018.
- [131] D. Z. Mohammed and A. AL-Janabi, “Large diameter coreless fiber as a saturable absorber for erbium doped fiber laser cavity based on multimode interference,” *Opt. Fiber Technol.*, vol. 50, pp. 212–215, 2019.
- [132] Z. Wang, D. N. Wang, F. Yang, L. Li, C. Zhao, B. Xu, S. Jin, S. Cao, and Z. Fang, “Stretched graded-index multimode optical fiber as a saturable absorber for erbium-doped fiber laser mode locking,” *Opt. Lett.*, vol. 43, no. 9, pp. 2078–2081, 2018.
- [133] H. Li, Z. Wang, C. Li, J. Zhang, and S. Xu, “Mode-locked Tm fiber laser using SMF-SIMF-GIMF-SMF fiber structure as a saturable absorber,” *Opt. Express*, vol. 25, no. 22, pp. 26546–26553, 2017.
- [134] T. Zhu, Z. Wang, D. N. Wang, F. Yang, and L. Li, “Observation of controllable tightly and loosely bound solitons with an all-fiber saturable absorber,” *Photonics Res.*, vol. 7, no. 1, pp. 61–68, 2019.

- [135] F. Yang, D. N. Wang, Z. Wang, L. Li, C. Zhao, B. Xu, S. Jin, S. Cao, and Z. Fang, “Saturable absorber based on a single mode fiber – graded index fiber – single mode fiber structure with inner micro-cavity,” *Opt. Express*, vol. 26, no. 2, pp. 927–934, 2018.
- [136] Z. Dong, J. Lin, H. Li, S. Li, R. Tao, C. Gu, P. Yao, and L. Xu, “Generation of mode-locked square-shaped and chair-like pulse based on reverse saturable absorption effect of nonlinear multimode interference,” *Opt. Express*, vol. 27, no. 20, pp. 27610–27617, 2019.
- [137] F. Zhao, Y. Wang, H. Wang, Z. Yan, X. Hu, W. Zhang, T. Zhang, and K. Zhou, “Ultrafast soliton and stretched-pulse switchable mode-locked fiber laser with hybrid structure of multimode fiber based saturable absorber,” *Sci. Rep.*, vol. 8, no. 16369, 2018.
- [138] Z. Lv, Z. Yang, D. Song, F. Li, X. Yang, Y. Yang, Y. Wang, Q. Li, and W. Zhao, “Nonlinear multimodal interference for ytterbium-doped all-fiber mode-locking noise-like pulse generation,” *Appl. Phys. Express*, vol. 12, no. 2, p. 022004, 2019.
- [139] S. Buch and G. P. Agrawal, “Soliton stability and trapping in multimode fibers,” *Opt. Lett.*, vol. 40, no. 2, pp. 225–228, 2015.
- [140] G. J. Liu, B. M. Liang, Q. Li, and G. L. Jin, “Beam propagation in nonlinear multimode interference waveguide,” *J. Opt. A: Pure Appl. Opt.*, vol. 7, pp. 457–462, 2005.
- [141] F. X. Kartner, I. D. Jung, and U. Keller, “Soliton mode-locking with saturable absorbers,” *IEEE J. Sel. Top. Quantum Electron.*, vol. 2, no. 3, pp. 540–556, 1996.
- [142] R. I. Woodward, “Dispersion engineering of mode-locked fibre lasers,” *J. Opt.*, vol. 20, p. 033002, 2018.
- [143] Z. Yan, B. Sun, X. Li, J. Luo, P. P. Shum, X. Yu, Y. Zhang, and Q. J. Wang, “Widely tunable Tm-doped mode-locked all-fiber laser,” *Sci. Rep.*, vol. 6, no. 27245, 2016.
- [144] P. Ciągćka, A. Rampur, A. Heidt, T. Feurer, and M. Klimczak, “Dispersion measurement of ultra-high numerical aperture fibers covering thulium, holmium, and erbium emission wavelengths,” *J. Opt. Soc. Am. B*, vol. 35, no. 6, pp. 1301–1307, 2018.
- [145] C. He, H. Yu, J. Zhang, S. Zou, P. Zhao, and X. Lin, “Flexible picosecond burst generation in a mode-locked Nd:YVO<sub>4</sub> laser with a compound cavity,” *Appl. Phys. B*, vol. 8, pp. 125–147, 2019.
- [146] W. Chen, W. Lin, T. Qiao, and Z. Yang, “Additive mode-locked resembling pulses in a Tm-doped fiber laser with a hybrid cavity configuration,” *Opt. Express*, vol. 23, pp. 28012–28021, 2015.

- 
- [147] H. Wang, D. Qi, X. Yu, Y. Zhang, Z. Zhang, T. Xu, X. Zhang, S. Dai, X. Shen, B. Song, P. Zhang, and Y. Xu, “In-situ and ex-situ characterization of femtosecond laser-induced ablation on As<sub>2</sub>S<sub>3</sub> chalcogenide glasses and advanced grating structures fabrication,” *Materials*, vol. 12, no. 1, p. 72, 2019.